1-1-2010

Three dimensional finite-element modeling of blood flow in elastic vessels: effects of arterial geometry and elasticity on aneurysm growth and rupture

Mohammed Yahya
Ryerson University

THREE DIMENSIONAL FINITE-ELEMENT MODELING OF BLOOD FLOW IN ELASTIC VESSELS: EFFECTS OF ARTERIAL GEOMETRY AND ELASTICITY ON ANEURYSM GROWTH AND RUPTURE

By
Mohammed Yahya
B.Sc. Mosul University, 1988
M.Sc. Mosul University, 1994
Mosul, Iraq

A thesis
presented to Ryerson University
in partial fulfillment of the
requirements for the degree of
Master of Science

in the Program of
Biomedical Physics
Toronto, Ontario, Canada, 2010

Author's Declaration

I hereby declare that I am the sole author of this thesis.

I authorize Ryerson University to lend this thesis to other institutions or individuals for the purpose of scholarly research.

_____

Mohammed Yahya

I further authorize Ryerson University to reproduce this thesis by photocopying or by other means, in total or in part, at the request of other institutions or individuals for the purpose of scholarly research.

_____

Mohammed Yahya

Abstract

Mohammed Yahya. "Three Dimensional Finite-Element Modeling of Blood Flow in Elastic Vessel: Effects of Arterial Geometry and Elasticity on Aneurysm Growth and Rupture", M. Sc. Biomedical Physics, Ryerson University, Toronto, 2010.

An intracranial aneurysm (ICA) is the localized dilation of cerebral arterial segment due to a degenerative arterial disease causing local wall weakness. Sudden ICA rupture of cerebral aneurysms is the leading cause of subarachnoid haemorrhage (SAH) which is a serious disease associated with high mortality and morbidity. In this research work, we have developed and validated a finite-element fluid-structure interaction (FSI) 2-way coupling model using COMSOL Multiphysics® software package. We applied the model to three idealized intracranial elastic arteries under the Newtonian blood flow assumption. The blood flow was characterized as a steady flow velocity at the inflow and various values of blood pressure at the outflow, while the arterial wall was modeled as a hyperelastic neo-Hookean material. The result shows the significantly weakened wall shear stress (WSS) at the aneurysm fundus and intensified WSS at the distal side of aneurysm neck. The wall deformation and WSS may play an important role in the growth and rupture of ICAs. Moreover, based on these results we postulate that lateral saccular aneurysms located on highly curved arteries are subjected to higher hemodynamic stresses and are more prone to rupture.

Acknowledgements

I would like to extend my sincere gratitude towards my thesis supervisor, Dr. Jahan Tavakkoli, for giving me the opportunity to work under his tutelage. His guidance throughout this thesis project was unyielding and vital to its completion. I am truly indebted to him for all his efforts, support and confidence during this research.

I am also deeply grateful to my thesis co-supervisor, Dr. Howard Ginsberg, whose insights helped frame this research and whose enthusiasm propelled it forward.

Additionally, I am thankful to my supervisory committee, Dr. Carl Kumaradas, and Dr. Raffi Karshafian for their guidance during this research.

To my good graduate student friends, thank you for your help and assistance in this research.

Special thanks to my lab mates, Dr. Min Rui, for her knowledge in High Frequency Ultrasound Scanner and Arthur Worthington who was always available for technical issues.

To my dear mom, dad, brother and sister back home, thanks for your blessings and support. Finally I would like to express my gratitude to my dear wife, Sura. Thank you for your steadfast love and support. You have kept me going through the most difficult times.

Table of Contents

Chapter 1 INTRODUCTION AND BACKGROUND 1
1.1 Introduction to the Human Circulatory System 1
1.2 Blood Vessel Structure 2
1.3 Cardiovascular Diseases 3
1.4 Cerebral Aneurysm 4
1.5 Motivation and Aims 7
1.5.1 Mechanical Behaviour of Arteries 9
1.5.2 Hemodynamics 14
1.6 Fluid Principles 16
1.7 Newtonian Viscous Fluid 20
1.7.1 Wall Shear Stress 20
1.8 Physics of Ultrasound 22
1.8.1 Doppler Effect 23
1.8.2 Ultrasound in Medicine 24
1.8.3 Doppler Ultrasound 25
1.8.3.1 Continuous Wave Systems 26
1.8.3.2 Pulsed Wave Systems 26
1.9 Computational Fluid Dynamics 28
1.10 Basic Principles of CFD 30
1.11 Previous Studies on Fluid-Structural Interaction (FSI) 33
1.12 Arbitrary Lagrangian–Eulerian Methods 35
Chapter 2 COMPUTIATIONAL FSI MODELING OF BLOOD FLOW 38
2.1 Model Geometries 38
2.2 Governing Equations 41
2.2.1 Flow Modeling 41

2.2.2 Elastic Vessel Wall Modeling 42
2.3 Boundary Conditions 45
2.4 Computational Details 46
2.5 Formulation of the Problem 47
Chapter 3 MODEL VALIDATIONS 48
3.1 Validation of the Numerical Model - Method One: Comparison with Experimental Data 49
3.1.1 Experimental Model 49
3.1.1.1 Rigid-Wall Phantom 49
3.1.1.2 Steady Flow System 50
3.1.1.3 High Frequency Ultrasound Scanner 53
3.1.1.4 Experimental Preparations 53
3.1.1.5 Experimental Velocity Measurements 55
3.1.2 Computational Model 56
3.1.2.1 Geometry Generation 56
3.1.2.2 Governing Equations 57
3.1.2.3 Boundary Conditions 57
3.1.3 Model Validation Results 58
3.2 Validation of the Numerical Model – Method Two: Comparison with Published Data 60
3.2.1 Experimental work 60
3.2.1 Computational Model 61
3.2.2 Model Validation Results 61
Chapter 4 RESULTS AND DISCUSSION 63
4.1 Influence of Wall Mechanical Properties on Aneurysms Initiation and Growth 63
4.1.1 Wall Deformations 63
4.1.2 Wall Shear Stress and Flow Field 70
4.2 Effects of Blood Vessel Geometry on Cerebral Aneurysm Initiation and Growth 74
4.2.1 Flow Dynamic and Velocity Field 74
4.2.2 Wall Shear Stress 77

4.3 Discussion 79
Chapter 5 CONCLUSIONS AND FUTURE WORK 84
5.1 Conclusions 84
5.2 Future Work 86

List of Symbols

σ_{ij}	First-order stress [Pa]
ε_{ij}	Cauchy's infinitesimal strain tensor
E	Young's modulus [$Pa\ or\ N/mm^2$]
λ	First Lamé constant
G	Second Lamé constant and is known as shear modulus [Pa]
ν	Poisson's ratio
δ_{ij}	Kronecker delta
h	Arterial wall thickness [mm]
p	Blood flow pressure [$mmHg\ or\ Pa$]
D_s	Distensibility volume [J/m^3]
R_c	Rupture critical radius [mm]
$\dot{\gamma}$	Shear rate [Sec^{-1}]
μ	Fluid viscosity [$N.s/m^2$]
ρ	Density [kg/m^3]
D	Arterial diameter [mm]
L	Arterial length [mm]
R	Arterial radius [mm]
R_e	Reynolds number
g	Gravitational external force [N]
u_i	Local velocity [mm/s]
x_i	Length coordinates [mm]
w	Strain energy density function

k Bulk modulus [Pa]

τ_w Wall shear stress [Pa]

e_{ij} Strain rate tensor

$\bar{I}$ Identity unit tensors

J Ratio of the deformed elastic volume over the undeformed volume

f_d Doppler frequency [Hz]

f_t Ultrasound transmitted frequency [Hz]

f_r Ultrasound received frequency [Hz]

S_l Large aneurysm neck surface area [mm^2]

S_s Small aneurysm neck surface area [mm^2]

F_i Components of body force [N]

List of Figures

Figure 1-1: Cross-sectional view of an artery showing the three distinct layers. 3
Figure 1-2: An inferior transverse view of the brain, illustrating the location of cerebral arteries aneurysms. 4
Figure 1-3: Illustrating brain aneurysms (Source: 2001 eCureMe.com). 5
Figure 1-4: Illustrating the principle of radii of curvature. 12
Figure 1-5: The mechanical response of an artery to inflation. The graph shows nonlinear wall tension (T) versus internal radius (R) relationship (solid curve). The four dashed lines are Laplace plots for four levels of pressure (P1 to P4), each having a unique intersection point with the artery curve (a to d, respectively). As long as the Laplace lines are not steep enough to become parallel to the artery curve, there will be a stable inflation..... 13
Figure 1-6: Velocity profiles for laminar (a), turbulent (b) and uniform (c) flow. 15
Figure 1-7: Rouleaux and Non-Rouleaux Blood formation. Source: homepage.ntlworld.com/.../Rouleaux%20Blood.JPG)..... 18
Figure 1-8: Diagram showing the velocity component, u, in the direction of the flow and the space coordinates x and y for a 'no slip' condition applied on the vessel wall. 21
Figure 1-9: A sketch of a saccular aneurysm cross section. 35
Figure 1-10: Doppler Ultrasound Angle. 24
Figure 1-11: Schematic illustration of the Doppler sample volume. 27
Figure 2-1: Geometry and Section Divisions of Saccular Aneurysm. 39
Figure 2-2: Geometry and Section Divisions of Saccular Aneurysm in a curved artery. 39
Figure 2-3: Geometry and Section Divisions of simplified Saccular Side walled Aneurysm, with large neck size (A) and small neck size (B). 40

Figure 3-1: Rexolite® multichannel blood vessel phantom. 49
Figure 3-2: A schematic diagram of the experimental flow system. 50
Figure 3-3: Flow System Setup. The flow system was used to measure the pulse wave velocity in multichannel blood vessel phantom. 51
Figure 3-4: A photograph shows the head and over flow containers that were used to convert the pulsatile flow to steady flow, as well as the manual valve tap that was used to control the fluid flow. 52
Figure 3-5: A photograph illustrate the transducer angle with the phantom for the pulse wave velocity measurements. 53
Figure 3-6: Experimental velocity measurements manual steps..... 54
Figure 3-7: Video Display of Vevo770® scanner for the Continues Velocity on the Blood Vessel Phantom. 55
Figure 3-8: 3D Mesh of multichannel blood vessel phantom. 56
Figure 3-9: Centerline velocity in the rigid Rexolite® phantom. 58
Figure 3-10: Shows the comparisons between the flow velocity from our experimental work that plotted in blue color and computed flow velocity results using FSI on the same geometry plotted in red color..... 59
Figure 3-11: Scheme of the experimental geometry, A: on ascending thoracic aorta. B: on mid-abdominal aorta. 60
Figure 3-12: Comparison result of experimental and simulated values of pressure as a function of vessel diameter. 62
Figure 4-1: Wall Deformation in μm for aneurysm geometrical evolution due to the Young`s Modulus of elasticity dynamic alteration large aneurysm neck surface area in 3D view. 65
Figure 4-2: Wall Deformation in μm for aneurysm geometrical evolution due to the Young`s Modulus of elasticity dynamic alteration large aneurysm neck surface area in 3D view. 65

Figure 4-3: Wall Deformation in µm for aneurysm geometrical evolution due to the Young`s Modulus of elasticity dynamic alteration large aneurysm neck surface area in 3D view. 66
Figure 4-4: Wall Deformation in µm for aneurysm geometrical evolution due to the Young`s Modulus of elasticity dynamic alteration small aneurysm neck surface area in 3D view. 66
Figure 4-5: Wall Deformation in µm for aneurysm geometrical evolution due to the Young`s Modulus of elasticity dynamic alteration small aneurysm neck surface area in 3D view. 67
Figure 4-6: Wall Deformation in µm for aneurysm geometrical evolution due to the Young`s Modulus of elasticity dynamic alteration small aneurysm neck surface area in 3D view. 67
Figure 4-7: Maximum wall displacements for models 2 as a function of outflow pressure... 68
Figure 4-8: Maximum wall displacements for models 3 as a function of outflow pressure... 68
Figure 4-9: Predicted aneurysmal wall rupture for the curved model 2 was calculated based on the Laplace law. 69
Figure 4-10: Von Mises wall shear stress in Pa for aneurysm geometrical at four different blood pressures 40, 80, 120, and 160 *mmHg at E=0.125 MPa* on large aneurysm neck surface area. 71
Figure 4-11: Von Mises wall shear stress in Pa for aneurysm geometrical at four different blood pressures 40, 80, 120, and 160 *mmHg at E=0.125 MPa* on large aneurysm neck surface area. 71
Figure 4-12: Von Mises wall shear stress in Pa for aneurysm geometrical at four different blood pressures 40, 80, 120, and 160 *mmHg at E=0.125 MPa* on large aneurysm neck surface area. 72
Figure 4-13: Von Mises wall shear stress in Pa for aneurysm geometrical at four different blood pressures 40, 80, 120, and 160 *mmHg at E=0.125 MPa* on small aneurysm neck surface area. 72

Figure 4-14: Von Mises wall shear stress in Pa for aneurysm geometrical at four different blood pressures 40, 80, 120, and 160 *mmHg at E=0.125 MPa* on small aneurysm neck surface area. 73
Figure 4-15: Von Mises wall shear stress in Pa for aneurysm geometrical at four different blood pressures 40, 80, 120, and 160 *mmHg at E=0.125 MPa* on large aneurysm neck surface area. 73
Figure 4-16: Velocity field and stream lines at the aneurysm plane in the straight artery model 1with two neck surface area. 75
Figure 4-17: Velocity field and stream lines at the aneurysm plane in curvature artery model 2 for the large neck surface area. 75
Figure 4-18: Velocity field and stream lines at the aneurysm plane in curvature artery model 2 for the small neck surface area. 75
Figure 4-19: Velocity field and stream lines at the aneurysm plane in arterial bifurcation model 3 for the large neck surface area. 76
Figure 4-20: Velocity field and stream lines at the aneurysm plane in arterial bifurcation model 3 for the small neck surface area. 76
Figure 4-21: Comparative plot of the maximum wall deformation at the aneurysm for the three models as a function of outflow pressure. 78
Figure 4-22: Comparative plot of the wall shear stress at the distal side of aneurysmal wall for the three models as a function of outflow pressure..... 78

Chapter 1 INTRODUCTION AND BACKGROUND

Computational fluid dynamics (CFD) modelling of cerebral hemodynamics requires some background into the anatomy, physiology and pathology of the cerebral vasculature before any modelling decisions are to be made. This chapter provides the required background to understand the scope of this research.

The chapter begins with special emphasis on the cardiovascular diseases and intracranial aneurysms (ICAs) which represent one of the forms of cardiovascular diseases that lead to the aim and motivation of this research. The next section describes the human systemic circulation followed by the structure and function of arteries, the mechanical properties of the arteries and the principle of fluid dynamics.

1.1 Introduction to the Human Circulatory System

The human circulatory system is spread all over the body and consists of the heart, which is the central unit and pumps the blood, the blood vessels and the blood. Its main functions are the transport of blood throughout the body carrying essential substances such as nutrients, oxygen and hormones to the cells. It also works for the removal of products and wastes of the cellular metabolism. For an average human being, the heart pumps five liters of blood through a complex network of blood vessels which is distributed to all the organs and parts of human body providing nutrients and oxygen that these organs use and carry out the waste products and potentially harmful chemicals, such as uric acid, away from these organs. The heart works as the pump and is responsible for providing the driving pulsed push to move all this blood while the lungs work for the exchange of blood components as providing oxygen to be carried to the vital and related organs and taking away the carbon dioxide that is gradually built up in the blood as it flows throughout the body.

The main vessels that release fresh blood from heart out are the arteries. The arteries in the systemic circulation transfers rich oxygenated blood, while the veins are the vessels that take away the unwanted chemical with waste gasses in particular where this transfer occurs. The arteries are comparatively larger vessels and they branch into smaller vessels called arterioles which branch further into smallest vessels called capillaries. These small vessels are the ones that reach every smallest possible part of the human body and hence play the most important role for the maximum transfer of materials carried within the blood to other parts of the body. Due to very small size, capillaries have extremely thin walls to allow for flow of fluids and nutrients, and after their job is done, they eventually come together to form vessels called venules where venules join together to form veins. Veins have a thin wall and relatively smaller in diameter as compared to arteries since the pressure exerted by their walls is very low as by those of arteries. Also the veins do not transfer many materials, but they do have valves along the vessel to prevent any incident of backward flow of blood (John Edward, 1946).

1.2 Blood Vessel Structure

The blood vessels form a continuous network throughout the human body. They can be generally classified into arteries, arterioles, capillaries, venules and veins. Since the capillaries and the venules are extremely thin, they do not possess layers as do the arteries and veins. The basic cross sectional structure of an artery consists of three layers surrounded by muscle and supporting tissue which are most apparent in the muscular arteries, since they have to force the pumped blood to all parts, and least apparent in the veins since pressure is dropped by the time blood stream reaches veins from the lumen to the outer wall of the blood vessels. The layers are the tunica intima, the tunica media and the tunica adventitia as illustrated in Figure 1-1 (John Edward, 1946).

The first layer, tunica intima consist of a layer of Vascular Endothelium (VE) which comprises the inner surface of blood vessels and its main role is to act as a filter between the blood and the rest of the biological tissues. Another role of endothelium is to act as a WSS sensor and is a major determinant of vascular remodeling (Hashimoto, Meng, & Young,

2006). The tunica intima and the next layer, tunica media are separated by an internal elastic membrane. The tunica media consists of smooth muscle cells arranged in a circular manner around the blood vessel. The tunica media also includes varying amounts of elastic and collagen fibers, depending on the size of the vessel. The tunica media is separated from the tunica adventitia by an external elastic membrane which can be identified at the outer border of the tunica media in some arteries (John Edward, 1946).

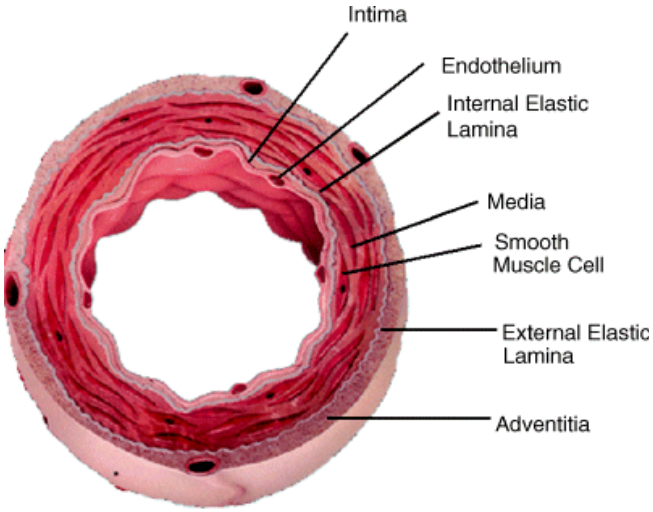

Figure 1-1: Cross-sectional view of an artery showing the three distinct layers.

http://www.medicalhistology.us/twiki/bin/view/Main/Cardiovascular

1.3 Cardiovascular Diseases

According to the most recent statistics, cardiovascular diseases are the third leading cause of death in the western world (Kroon & Holzapfel, 2008). One form of cardiovascular disease is cerebral aneurysm. The rupture of cerebral aneurysms is the leading cause of subarachnoid haemorrhage (SAH) which is a serious disease associated with high mortality and morbidity (Hashimoto et al., 2006; Krex, Schackert, & Schackert, 2001) . Approximately 50% of patients with aneurismal SAH die or suffer severe disability as a result of the initial haemorrhage; another 23 to 35% die as a result of subsequent haemorrhage if the aneurysm is not treated. (Hoi et al., 2004; Humphrey & Canham, 2000). ICA is a moderately common condition that is often asymptomatic until the time of rupture. The fundamental

understanding of the cerebral aneurysms, improvement in new clinical solutions in the form of treatment methods, medical advices, and advanced surgical techniques lead to the reduction of morbidity and mortality associated with the disease.

1.4 Cerebral Aneurysm

A brain aneurysm, also called a cerebral or ICA, is a cerebrovascular disorder caused by the weakness in the wall of a cerebral artery. An aneurysm can simply be described as a weak spot or an infected part on the wall of an artery which becomes more compliant than a healthy vessel. It has less resistance to counteract hemodynamic forces. The weak area causes a localized dilation or ballooning of the blood vessel. The blood vessel bulges outward to form a balloon-like protuberance. Aneurysms are more likely to be formed at high pressure regions in the circulatory system, usually occurring in or near the circle of Willis (Oshima, Torii, Kobayashi, Taniguchi, & Takagi, 2001; Q. Wang, and Cao, 2009), the primary network of vessels that supply blood to the brain and at bifurcations, as illustrated in Figure 1-2.

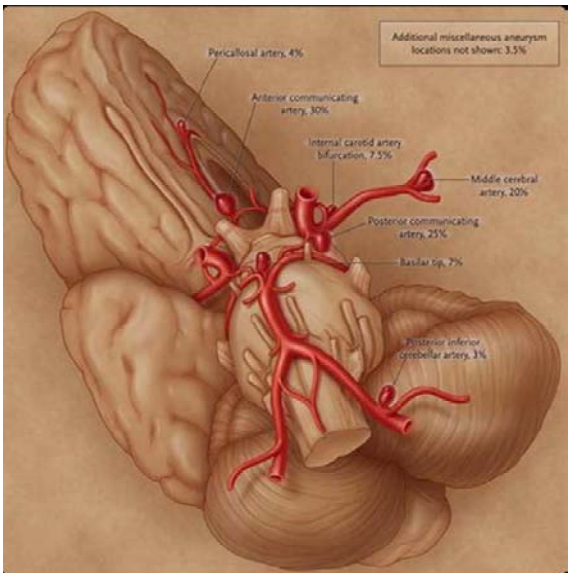

Figure 1-2: An inferior transverse view of the brain, illustrating the location of cerebral arteries aneurysms. http://emedicine.medscape.com/article/252142-overview

Aneurysm is localized, irreversible dilatation of an artery, at least one and a half times its normal diameter, and caused due to the destruction of the vessel wall by infection. The shape of the aneurysm varies from patient to patient, but generally it is roughly a spherical or oblong protrusion from the artery wall.

In general, these aneurysms occur in one of four forms: Saccular, Fusiform, Dissecting, and Mycotic types as shown in Figure 1-3. Saccular and Fusiform represent the two main types of ICA, however the saccular type accounts for 90% of ICAs; thus, it will be the focus of this research.

Fusiform aneurysm is spindle-shaped in which the entire circumference of the vessel is distended, usually occurring in the abdominal and rarely in the brain (Peattie, Riehle, & Bluth, 2004). However, the saccular aneurysm forms a sac-like bulge on one side of an artery. A mycotic aneurysm is an aneurysm that becomes infected as a result of bacterial or fungal accumulation in the bloodstream. It can also be a pre-existing aneurysm that becomes infected. The fourth type is dissecting aneurysm that results from a tear between the tissues layers of the aorta, caused by blood flow pumped from the heart. This tear usually occurs in the aorta close to the heart. Dissecting aneurysms are formed from the separation of tunica layers which fill with blood.

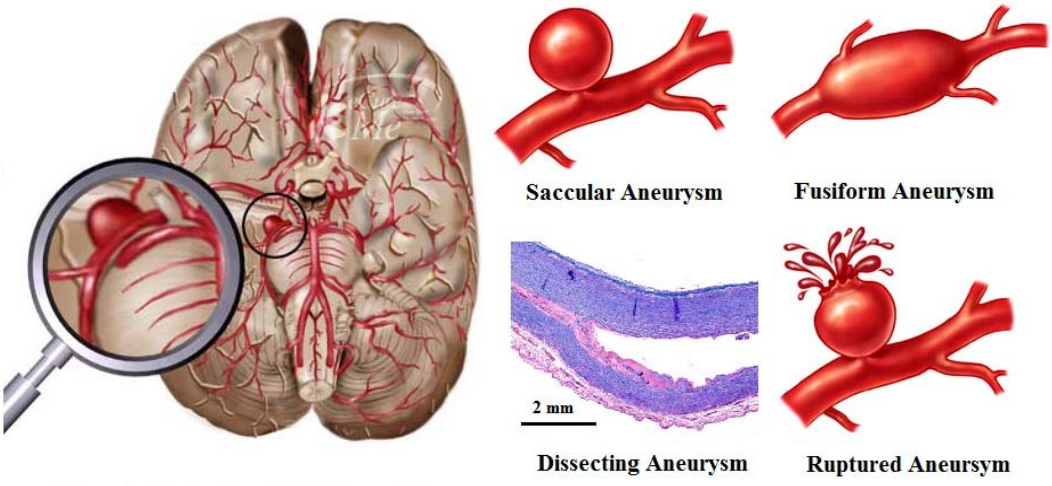

Figure 1-3: Illustrating brain aneurysms (Source: 2001 eCureMe.com).

The natural history of saccular aneurysms comprises of three phases: pathogenesis, enlargement, and rupture (Nikolov, Stoytchev, Torres, & Nieto, 2003). The local hemodynamic environments influence the pathogenesis of cerebral aneurysms significantly. Clinical observations indicate that most cerebral aneurysms originate from area subjected to increased hemodynamic forces, that is, at the apex of the arterial bifurcations or on the curve of tortuous vessels, instead of along straight vessel segments (Humphrey & Canham, 2000). The enlargement of cerebral aneurysm continues till the vessels rupture if left untreated. Fortunately, with the advances in medical imaging, greater numbers of unruptured aneurysms get detected before it ruptures.

Presently, the causes of aneurysms are not fully clear yet, however atherosclerosis, atheroma, syphilis, congenital defects, heart attacks, smoking, obesity, hypertension, trauma, inflammation and/or hereditary conditions are considered by researchers as some of the main causes (Hademenos, Massoud, Valentino, Duckwiler, & Vinuela, 1994a; Hademenos, Massoud, Valentino, Duckwiler, & Vinuela, 1994b). Besides these, hemodynamics and biomechemical factors like vessel WSS are other causes of aneurysms that will be discussed in detail later in this thresis (Hashimoto et al., 2006; Niroomand Oscuii, Tafazzoli Shadpour, & Ghalichi, 2007; Torii, Oshima, Kobayashi, Takagi, & Tezduyar, 2010).

Aneurysms can be treated by two primary methods: intracranial surgery, in which blood flow is cut off from the aneurysm dilatation by placing a small metal clip at the neck; and endovascular embolization, which includes the development of metallic coils that promote the formation of clots within the lesion that again isolates it from the blood flow (Nichols, Meyer, Piepgras, & Smith, 1994; P. J. Camarata, R. E. Latchaw, 1993).

1.5 Motivation and Aims

Recently, significant amount of research is being carried on cerebral aneurysms in intracranial arteries- arteries that have an enlargement at some point on the arterial wall. However, the exact causes of aneurysm are still not clear.

Usually, the enlargement of cerebral aneurysm continues until they rupture if they are not treated. The rupture of ICAs is followed by subarachnoid haemorrhage (SAH), a serious disease associated with high mortality and morbidity. Due to their unpredictable nature, the study of aneurysms is restricted *in vivo* to clinical observations of patients and tissue specimens retrieved at autopsy (Hademenos, Massoud, Valentino, Duckwiler, & Vinuela, 1994a). Nevertheless, special attention is being diverted towards understanding the physics involved with the aneurysm itself and the causes and possible methods of its treatment. Numerous experiments have been conducted in order to study the geometry and fluid effects on the condition. These studies have provided valuable data which contributes tremendously towards understanding the problem. There are certain limitations with these experimental techniques which need to be investigated by applying other methods. The modeling of flow behavior within aneurysm arteries was investigated by applying other methods. The modeling of flow behavior within aneurysm arteries of varying geometry and conditions has become much easier due to recent computational techniques which can be calibrated and adjusted according to realistic clinical situations.

When it comes to economy, accuracy and reliability, the computational technique is probably the preferable choice since it is fast in addition to above mentioned qualities. As technological advancements have been achieved, computational power has increased manifold. As a result the simulations can be carried out with more complexity, and can incorporate a greater number of variables. This leads to better approximation of realistic results.

The study of the relationship between the shape of aneurysm and blood flow has been extended due to numerical simulations using geometry and other physical characteristics obtained from medical samples and non-invasive methods. This study has served as the

basics for extending research since in covers many factors that are related to flow of blood and the growth. The study of rupture of arteries is also supported by this extended research. It also provides a detailed analysis of steady and transient flow of blood.

Inclusion of Fluid-Structural Interaction (FSI), which allows a coupling between fluid and solid models, is another major development. This method has an advantage that it allows for a study of the vessel wall behavior and corresponding flow response to wall deformation, which previously was not considered. With the help of this, studding the aneurysms growth and determining critical radius where an aneurysm may rupture.

Approaches in studies like pathogenesis and hemodynamic of cerebral aneurysms have been carried out intensively, but they do not help much in understanding the problem. A number of simulations have been incorporated to study incompressible Newtonian and non-Newtonian blood flow or FSI individually in different shape and size aneurysms (Bazilevs et al., 2010; Castro, Putman, & Cebral, 2006; Chen & Sheu, 2003). Still, there is a lot of research pending to study the formation of aneurysms growth and carrying out risk analysis for probability of a rupture.

The motivation behind this work includes understanding the mechanisms of the initiation, development and rupture of human ICAs. More focus has been given to saccular aneurysm, since saccular aneurysms are more commend in cerebral arteries. In this study we grafting aneurysm represented with different mechanical properties in a healthy arterial wall to understand the way of aneurysms growth. In addition this study covers the effect of arterial curvature into the growth of aneurysms.

An iterative two-way coupling method will be employed to link the fluid and solid models and provide an understanding of the influences between these models as well as the basic physical characteristics such as WSS, deformations and flow properties, which play important roles in initiation and formation of aneurysms. To achieve this, the COMSOL Multiphysics® software package will be used (COMSOL Inc., Burlington, MA, USA), which carries out the modeling of the fluid and structural portions respectively, as well as provides a bridging environment to couple them.

1.5.1 Mechanical Behaviour of Arteries

Mathematical modeling of the initiation, development and rupture of cerebral aneurysms requires a material description of the human cerebral arterial walls and saccular walls when a constitutive equation of blood and study of its flow in cerebral circulation are required if hemodynamic factors are considered. Generally, testing and modeling the mechanical properties of biological soft tissues usually becomes challenging, since many of them are nonlinear, viscoelastic and anisotropic (Y.C. Fung, 1993). As for the arteries posses as a nonlinear elastic properties and have a stress-strain relationship that can be mathematically described as an approximately exponential function (Wilmer W. Nichols and Michael F. O'Rourke, 1990; Y.C. Fung, 1993).

Most of the biological tissues generally exhibit an isotropic property, which is they have geometrically uniform dimensions (Wilmer W. Nichols and Michael F. O'Rourke, 1990; Y.C. Fung, 1993), consider an isotropic tissues within a mathematical framework, then even the most general form requires a large number of terms to describe the mechanical properties since the geometry changes non-uniformly. However for ease of calculations, if we make the assumption that tissue is isotropic (Fung 1967; Galey 1969), then only two independent constants are required in the mathematical model (Saada 1993). These two constants are called the Lamé constants, as described below.

Biological materials in the human body like vessels have a nature of being deformed in stress situations. If an artery is subjected to a pressure as mechanical loading or a compressive force, then deformation occurs and stresses are developed within that arterial wall. The amount of deformation and strain depend on the history and rate of the applied loading, temperature, etc., and the deformed shape usually does not return to its original configuration when the load is removed (Y.C. Fung, 1993). When the deformation is very small and adiabatic (i.e., no heat is gained or lost), then the most likely condition is that the stress and strain are independent of the loading rate and history, and that the material is likely to return to its original configuration after the compressive force is removed.

If deformation is the only factor, the stress in an elastic body can be expressed as a function of the strain as follows:

$$\sigma_{ij} = f_{ij}(\varepsilon_{ij}), \qquad 1-1$$

where σ_{ij} and ε_{ij} denote the first-order stress and strain tensors, respectively. Assuming that the deformation is linear elastic, and then equation 1-1 becomes:

$$\sigma_{ij} = A_{ij} + C_{ij}\varepsilon_{ij}, \qquad 1-2$$

where $A_{ij} = f_{ij}(0)$ and $C_{ij} = \partial f_{ij}(0)/\partial\varepsilon_{ij}$ are constants and usually called *young's modulus*. A_{ij} represents the state of stress at $\varepsilon_{ij} = 0$, namely, the initial stress. Within the context of linear elastic deformation, the initial stress can be neglected and consequently, equation 1-2 can be simplified to:

$$\sigma_{ij} = E\varepsilon_{ij}, \qquad 1-3$$

where, E is young's elasticity modulus, equation 1-3 is called the generalized Hooke's law where is describes the proportionality of the stress and strain, which states that each of the components of the state of stress at a point is a linear function of the components of the state of strain at that point. The strain tensor introduced in equation 1-3 is defined mathematically as:

$$\varepsilon_{ij} = \frac{1}{2}\left(\frac{\partial u_i}{\partial x_j} + \frac{\partial u_j}{\partial x_i}\right) \qquad 1-4$$

The strain tensor ε_{ij} was introduced by Cauchy and Green and is called *Cauchy's infinitesimal strain tensor,* where u_i is the displacement component in the i^{th}direction and u_j is the displacement captured in the j^{th} direction of the displaced material point (Y.C. Fung, 1990).

For the Hookean elastic solid, a solid that obeys Hooke's law according to which the stress tensor is linearly proportional to the strain tensor:

$$\sigma_{ij} = C_{ijkl}\varepsilon_{kl}, \qquad 1-5$$

where σ_{ij} is the stress tensor, ε_{kl} is the strain tensor, and C_{ijkl} is a tensor of elastic constants, or module, which are independent of stress and strain. If material is isotropic with regular geometry, a great reduction in the number of elastic constants is obtained, and the constitutive equation of an isotropic material has exactly two independent elastic constant, for which the Hooke's law mathematically states:

$$\sigma_{ij} = \lambda\varepsilon_{\alpha\alpha}\ \delta_{ij} + 2G\varepsilon_{ij} \qquad 1-6$$

Where, λ and G are called the *first and second Lamé constants*, respectively. The second Lamé constant G is identified as the *shear modulus*.

As a general practice, the elastic properties of materials are described by their Young's Modulus and the Poisson's ratio since the Lamé constants are achieved after rigorous mathematical calculations and their physical meanings are complex for interpretation. The relationship between both the Young's modulus and Poisson's ratio and the Lamé constants can be derived by considering an elastic isotropic material and a simple contraction deformation experiment.

$$G = \frac{\lambda(1-2\nu)}{2\nu} = \frac{E}{2(1+\nu)}\,, \qquad 1-7$$

where ν is the Poisson's ratio.

Most metals and rubbers have linear elasticity, for small strain values. This simplest deformation behavior of a purely elastic body can be described by Hooke's law of elasticity. If the applied stress is plotted against the resulting strain, it yields a straight line whose slope is the elastic or Young modulus, and describes quantitative measure of an object to retain its original state or shape (Scott, Ferguson, & Roach, 1972). In other words, if a linearly elastic material is deformed, a plot of the applied stress against the resulting strain gives a straight line whose slope is the Young's modulus of elasticity. This is a measure of the elastic stiffness of the material. A material with a high Young's modulus is stiffer, and less easily deformed, than one with a low Young's modulus. For example steel has a higher young's modulus than rubber. In human circulatory system, arteries and most biological tissues have nonlinear elastic properties. When arteries are expanded, the elastic modulus is not constant because it increases as the strain changes due to nonlinearity. Arteries get nonlinear elastic behavior due to the presence of their stiff and rubbery constituents that is collagen and elastin respectively (Robert Shadwick, 1999; Y.C. Fung, 1993). In physics, elastic rigidity increases with the degree of stress, and it is more suitable to describe these properties using an elastic modulus that is expressed as a function of the strain or distending pressure. Non-linear

behavior is the key to elastic stability in any highly stretchable pressure vessel, protecting against aneurysms and consequent blowout (Burton, 1954; Gordon, 1975).

It has come into observation that while in addition to the nonlinear behavior, cerebral arterial walls also exhibit inelastic behavior under effectively high loads. The most relevant mechanical testing in which arteries have an inelastic behavior of arteries was revealed by Scott et al. (Scott et al., 1972).

The inflation behavior of a cylindrical blood vessel can be governed by the Law of Laplace that describes the behavior of a membrane that encapsulates the vessel. This law describes the state of equilibrium of a curved membrane subjected to a pressure. The membrane stress ($\sigma_{membrane}$) can be described as follows:

$$\sigma_{membrane} = \frac{P/h}{\left(\frac{1}{R_1} + \frac{1}{R_2}\right)} \qquad 1-8$$

where P represents the internal pressure, h is the membrane thickness, and R_1 and R_2 are the principle radii of curvature, where R_1 is the arterial radii curvature and R_2 is the arterial inner radii. The above equation does not consider external pressure and assumes that the membrane stress is independent of the direction (see Figure 1-4). For the case of a straight tube, $R_1 = R \; and \; R_2 \Rightarrow \infty$, and the Law of Laplace yields the mean circumferential stress,

$$\sigma_{circ} = \frac{PR}{h} \qquad 1-9$$

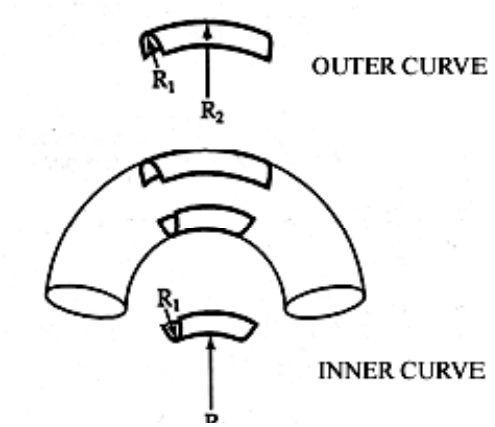

Figure 1-4: Illustrating the principle of radii of curvature.

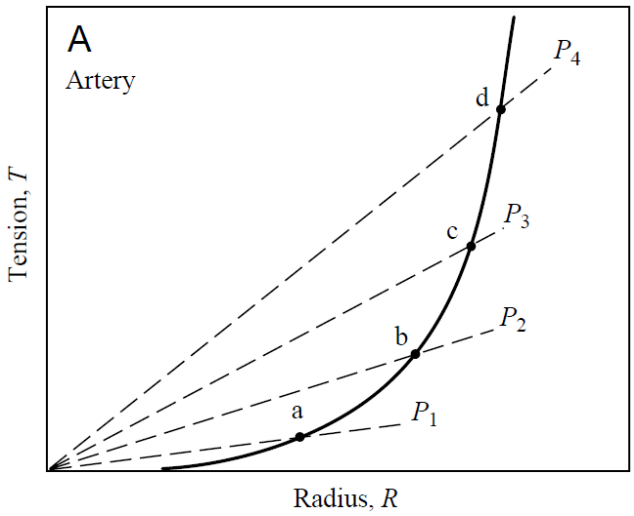

Figure 1-5: The mechanical response of an artery to inflation. The graph shows nonlinear wall tension (T) versus internal radius (R) relationship (solid curve).

The nonlinear properties of an artery may be well studied by plotting of T versus R as shown in Figure 1-5. The four dashed lines are Laplace plots for four levels of pressure (P1 to P4), each having a unique intersection point with the artery curve (a to d,) respectively. As long as the Laplace lines are not steep enough to become parallel to the artery curve, there will be a stable inflation. Nevertheless in this graph are placed a family of straight lines through the origin, each representing the Laplace relationship at a different pressure. It is noteworthy here that the Laplace plot of T versus R for pressure P_i is a straight line with slope (P_i).

The above analysis illustrates that each Laplace line has only one point of intersection with the artery curve, and this is the point which represents the equilibrium radius for the artery at that pressure.

Keeping in mind the above graph, to maintain stable inflation requires that increasing pressures must all have equilibrium intersection points on the artery curve. In contrast to this, a similar operation on the tension–radius relationship curve for a cylindrical rubber tube where a small incremental change in pressure results in a large increment in radius, forming

the aneurysm. This phenomenon is typically observed when a balloon is inflated, as air enters it, pressure is increased and rubber walls expand with huge increments in radius of balloon.

There is also a case where instability occurs and that is at the pressure at which the Laplace line is tangential to the inflation curve for the cylinder. This graphical analysis illustrates that the tension–radius curve for the elastic cylinder must have a continuously increasing slope that is nonlinear elasticity to be stable in the situation of increasing pressure. This required condition was also illustrated more quantitatively by (Burton, 1954), who defined relative volume distensibility as $\mathrm{D_s} = \frac{\mathrm{dV}}{\mathrm{VdP}}$, the Distensibility, defined as the relative change in volume per unit of pressure, where V is volume, and was shown to be inversely proportional to the expression $(Eh/R) - P$, where E is the elastic modulus and h is the wall thickness. So, as P increases, R will increase and h will decrease. If E is constant (linear elasticity), then D_s will increase and become infinitely large and get unstable values as P approaches (Eh/R), causing rupture. To balance this, E must increase as a function of P, such that (Eh/R), is always greater than P. based on Laplace law the critical risk of rapture radii for spherical shape such as saccular aneurysms can be written as (George J. Hademenos, Tarik F. Massoud, 1998):

$$R_c = \frac{2Eh}{P} \qquad 1-10$$

1.5.2 Hemodynamics

Blood is formed essentially of erythrocytes commonly known as “Red Blood Cells” (RBCs), leukocytes known as “White Blood Cells” (WBCs), and platelets that are suspended in the plasma. From physical point of view, since blood is a fluid which consists of different constituents, it is viscous due to the friction of a two different layers pass over each other.

Viscosity is a physical property of every fluid. In less viscous fluids such as water, viscosity is independent on the rate at which the adjacent fluid layers slide over one another in another word the relative velocities in laminar flow of parallel adjacent layers of a fluid body under shear force called (shear rate $\dot{\gamma}$) and such fluids are usually referred to as Newtonian fluids. In contrast to simple fluids as water, blood is a suspension of particles,

therefore the viscous properties of blood are complex and therefore blood is a non-Newtonian fluid. It has been shown that if the arterial diameter is greater than 1mm, the effect of RBC in the flow is minimizes as the size of the RBC is too small compared to the arterial diameter and therefore it is pertinent to neglect lead to a constant viscosity of blood in this case (Huo, Choy, Svendsen, Sinha, & Kassab, 2009; Wilmer W. Nichols and Michael F. O'Rourke, 1990), and consider the asymptotic value of blood viscosity, that is the value to which the apparent viscosity tends at high shear rate of adjacent sliding layers. Its value at normal physiological conditions for an average human being is in the range of $\mu = 3 \times 10^{-3} - 4 \times 10^{-3} N.s/m^2$ with a density of $\rho = 1060\ Kg/m^3$.

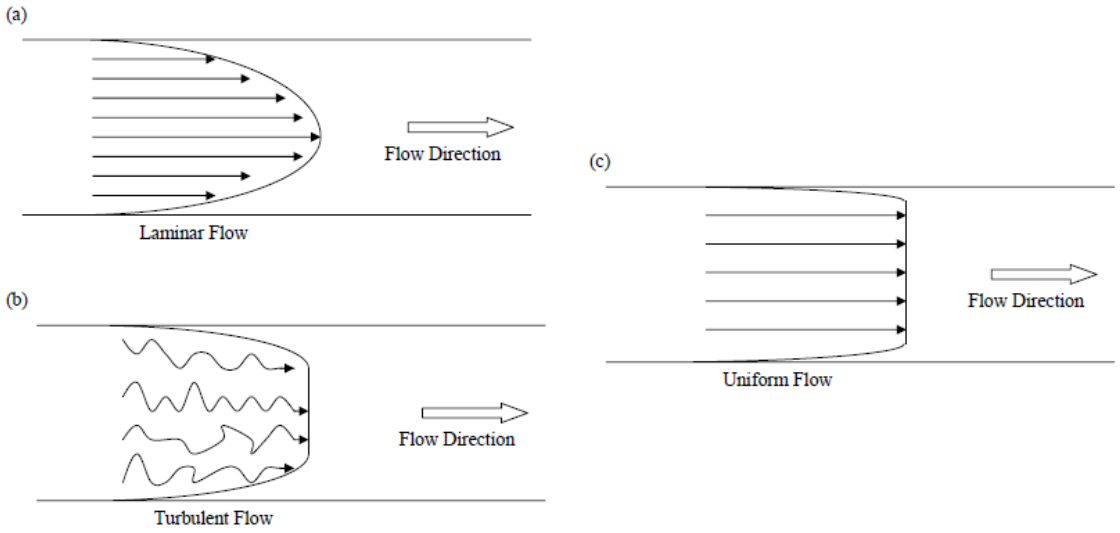

Figure 1-6: Velocity profiles for laminar (a), turbulent (b) and uniform (c) flow.

A fluid flowing in a vessel exhibits motion which is classified into two types: laminar or turbulent. In laminar flow the fluid particles move along smooth paths in layers with every layer sliding smoothly over its neighbor. It is also called streamline flow. As the velocity of flow increases, the different layers start interfering in each others' motion due to different inertia and friction at some point and eventually the laminar flow becomes unstable, vortices start to form, and ultimately the fluid flow becomes turbulent. Hence turbulent flow is one in which different layers collide with one another and cause non-uniformity. When the flow is turbulent the velocity vectors of the fluid particles at every point change rapidly with time,

both in magnitude and direction. Both the laminar and turbulent flows have different developed sketches, as illustrated in Figure 1-6.

For every fluid, to reach turbulent flow, there is a threshold value dependent on the average fluid velocity, density, viscosity and the diameter of the vessel (for internal flows). This characteristic value, which depends on all these quantities, is called the Reynolds number (R_e), as shown below in equation 1-11.

$$R_e = \frac{\rho u D}{\mu} \qquad 1-11$$

Where, u is the average fluid velocity, D is the vessel diameter, ρ is the fluid density, μ is the fluid (dynamic) viscosity. It has been found through experiments that the fluid (blood) tends to become turbulent at a Reynolds number of approximately 2000 for internal flows (Wilmer W. Nichols and Michael F. O'Rourke, 1997,1990,1998).

1.6 Fluid Principles

Dynamics is a branch of physics that involves studying motion under the influence of forces. It is fundamental that force drives fluid motion. Newton's second law of motion, $F = m \times a$ (force = mass × acceleration) also applies to fluid flow. Changes in pressure and body force (such as gravity) produce fluidic motion. Shear forces, on the other hand, oppose fluid motion by creating friction between different layers. Shear forces occur when a fluid body is subjected to deformation. In streamline flows, shear is caused from the viscosity of the fluid. When turbulence is present, its current like motion causes the shear forces. Shear forces diffuse through the flow, which result in variation in velocity. Along these lines, shear forces counterbalance pressure gradients and body forces.

Fluid motion is said to have zero acceleration when the sum of the shear, pressure gradient and body forces are zero. In this way the fluid motion remains constant. Since acceleration is zero, net force is zero. However, whenever one of these factors breaks the balance, then the fluid achieves acceleration and force must be accounted for this acceleration. The resultant acceleration which is created is of two possible types: temporal

and convective. Temporal acceleration is the one that occurs due to flow that changes with respect to time. Convective accelerations are due to change in fluid motion as a fluid moves from one location to another. In other words, it is the acceleration that changes with respect to displacement. For instance, the accelerations a fluid experiences through an arterial constriction are convective since it is different at different location while the accelerations a fluid experiences during the heart pumping cycle are temporal.

Since in dynamics, momentum is always conserved, the forces driving and opposing fluid motion may be equated to the accelerations. Assuming that fluid is incompressible and that the fluid exhibits Newtonian fluid properties, the conservation of momentum leads to a commonly used form of equation called the Navier-Stokes equation as (Oshima et al., 2001; Torii, Oshima, Kobayashi, Takagi, & Tezduyar, 2006).

$$\rho\left(\frac{\partial u_i}{\partial t} + u_j\frac{\partial u_j}{\partial x_j}\right) = -\frac{\partial P}{\partial x_i} + \rho g + \mu\frac{\partial^2 u_i}{\partial x_j \partial x_j} \qquad 1-12$$

Here, u_i = (*u, v, w*) is the local velocity, x_i = (*x, y, z*) is the length coordinate, *t* is the time scale, *P* is the fluid pressure, μ is the dynamic viscosity, $f_i = \rho g$ is the body force, and *g* is the gravitational constant. The terms on the left hand side collectively represent momentum change from temporal and convective acceleration. On the right hand side, the terms represent pressure gradient, gravitational forces and shear forces.

One of the fundamental principles that are followed in dynamics is the law of conservation of mass. Mass is neither created nor destroyed by any non-nuclear processes. This is fundamental to physics, fluid dynamics, and cardiovascular circulation. Considering an incompressible fluid, the conservation of mass is represented by,

$$\frac{\partial u_i}{\partial x_i} = 0 \qquad 1-13$$

The study of fluid flow combines the laws of conservation of momentum and mass both. Sometimes the equations of fluid flow containing limited parameters of mass and momentum may be solved analytically to describe the flow field. However when analytical solutions are not possible or when mass and momentum relationships follow non-uniform behaviour, these equations may be approximated using iterative numerical methods.

In fluid motion, sheer stress and its rate of change affect the flow depending on their values. The relationship between the shear stress, τ, and shear rate, $\dot{\gamma}$, determines the fluids ability to flow when sheer stress keeps on changing (Wilmer W. Nichols and Michael F. O'Rourke, 1997,1990,1998). For Newtonian fluids the correlation between shear stress and shear rate is linear. This relationship is sometimes expressed using a single constant, the dynamic viscosity, μ (Agarwal, Katiyar, & Pradhan, 2008). The best example of a Newtonian fluid is water which exhibits laminar fluid flow with linear behaviour in terms of shear stress and shear rate. But many other simple homogenous fluids also exhibit these properties.

Blood has different behaviour from water in terms of fluid flow. At low shear, blood becomes thick and becomes more viscous. Red blood cells align and aggregate to form rouleaux Figure 1-7 (Schmid-Schönbein, Wells, & Goldstone, 1969).

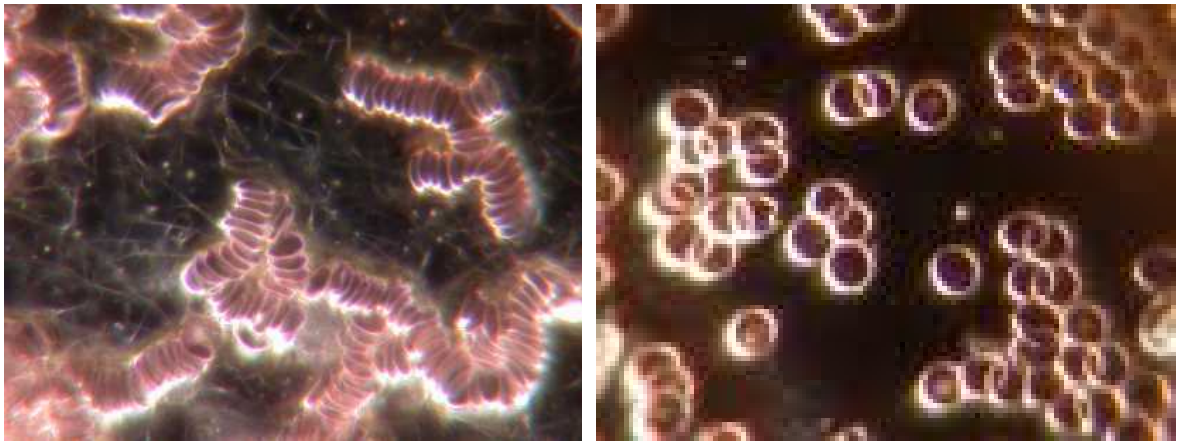

Figure 1-7: Rouleaux and Non-Rouleaux Blood formation. Source: http://www.homepage.ntlworld.com/.../Rouleaux%20Blood.JPG

When rouleaux are formed, it acts as an opposing force to fluid flow. The formation of rouleaux slows down the ability of the blood to flow. More specifically, blood has the properties of a Casson fluid that is shear-thinning fluid, which shows both a yield stress and a non-linear relationship between stress and strain in the fluid flow system (Fournier, 1999). Casson fluids show three types of behaviour depending on the values of shear:

1) Low Values of Shear

When the shear is low, the yield stress of blood ($0.004\ N/m^2$), the yield stress is the applied stress we must exceed than shear in order to allow for the blood to flow. In case the change in pressure is not enough to overcome the viscous yield stress, the fluid does not flow. Since fluid is not flowing in such conditions, the viscosity is said to be infinite to make a structured fluid flow

2) Shear Surpasses Yield Stress

When the yield stress is overcome and the blood becomes fluidic, it results in a nonlinear behaviour between stress and strain. This condition occurs at low to moderate strain rates ($\dot{\gamma} < 100\ \mathrm{s}^{-1}$). Such strain rates are present in smaller blood vessels. Due to lower value of shear, the viscosity remains variable at different points.

3) High Values of Shear

The shear stress and shear rate correlation becomes more linear at higher value of shear ($\dot{\gamma} > 100\ \mathrm{s}^{-1}$), which results in constant effective viscosity. These conditions are observed only in the largest arteries, the blood behaves in a Newtonian manner (Wilmer W. Nichols and Michael F. O'Rourke, 1990). That is why, the Newtonian behaviour is assumed throughout this study and the kinematic viscosity, μ , is considered constant at $0.0035\ N.s/m^2$. The dynamic viscosity, $v = 0.003465\ \mathrm{N/m^2}$, which is the product of the density, ρ, and kinematic viscosity ($\mu = \rho v$). The density of blood under pressures experienced in our study assumed to be constant at $\rho = 1060\ kg/\mathrm{m}^3$. To make the study mathematically simpler, blood is modeled as an incompressible fluid.

1.7 Newtonian Viscous Fluid

Newtonian viscous fluid is a fluid for which the shear stress is linearly proportional to the strain rate. For a Newtonian fluid the stress-strain relationship is specified by the equation;

$$\sigma_{ij} = -p\delta_{ij} + \mu_{ijkl} e_{kl} \qquad 1-14$$

where σ_{ij} is the stress tensor, e_{kl} is the strain rate tensor, μ_{ijkl} is the tensor of viscosity coefficients of the fluid, P is the static pressure, and δ_{ij} is the kronecker delta, which has the value 1 if $i = j$, and zero if $i \neq j$. The term $-P\delta_{ij}$ represents the state possible in a fluid at rest (when $e_{kl} = 0$). For equations purposes, assume an isotropic tensor, which the tensor has the same array of components when the frame of reference is rotated or reflected. In this case, the isotropic constitutive equation yields:

If a fluid is incompressible, then $e_{kk} = 0$, and the constitutive equation for an incompressible viscous fluid becomes:

$$\sigma_{ij} = -P\delta_{ij} + \lambda e_{kk}\delta_{ij} + 2\mu e_{ij} \qquad 1-15$$

1.7.1 Wall Shear Stress

The Wall shear stress τ_w, is a vector, containing both a directional and a magnitude component, where is defined as the gradient of the velocity of the fluid at and normal to the wall times its dynamic viscosity.

Newton's concept of viscosity may be elucidated in the simplest case of a shear flow with a uniform velocity gradient as sketched in Figure 1-8. Fluid in contact with the vessel wall will travel at the same velocity as the wall under the 'no slip' condition forced on the boundary. This is a logical assumption as the shear forces applied by the wall on the fluid will ultimately cause the flow on the boundary to have the same velocity as the wall further downstream, which in this study is equal to zero. In the meantime, in order to maintain mass balance, the flow further away from the vessel wall is inclined to increase in velocity until it reaches a developed profile, after which no further changes in velocity profile occur in the

flow direction. These results in a non-zero velocity gradient du/dy , where u and y are the velocity component in the direction of the flow and the space coordinate normal to the flow direction respectively as shown in Figure 1-8.

$$\tau_w = \mu \frac{du}{dy} \qquad 1-16$$

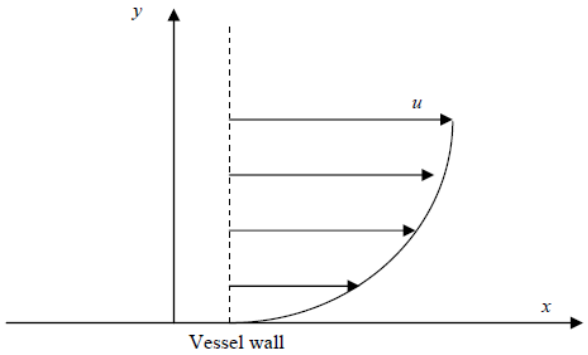

Figure 1-8: Diagram showing the velocity component, u, in the direction of the flow and the space coordinates x and y for a 'no slip' condition applied on the vessel wall.

where τ is the shear stress, μ is the coefficient of viscosity, the unit of μ in SI system is $N.s/m^2$ is called a poise ($1\,poise = 0.1\,N.s/m^2$, in honour of Poiseuille, the French physicist who did seminal works in this field.

Direct WSS measurement is not feasible, therefore to evaluate wall shear, three measurements are required. 1) The dynamic viscosity must be known. 2) The velocity near the wall must be determined in fine details to accurately evaluate the gradient. 3) The normal direction of the wall must be found. Viscosity evaluation is challenged by the Casson properties of blood and its coagulation outside the body, but the Newtonian assumption simplifies this portion of the calculation.

It has been demonstrated that WSS plays important roles in initiation and growth on ICAs (Oshima et al., 2001). Since this quantity is difficult to attain using experimental techniques, it mostly relies on knowledge of the fluid viscosity and velocity profile near the vessel wall. Computational fluid dynamics (CFD) techniques make this quantity easier to

estimate and numerous studies have been devoted to WSS estimation in aneurysms considering a rigid wall using this technique (Hoi et al., 2004; Peattie et al., 2004; Q. Wang et al., 2009). Moreover, In case of an elastic wall by implementing the FSI method, only a few attempts have been done to estimate the WSS in a blood vessel. The FSI modeling showed significant difference in WSS between rigid and elastic wall, with an increase of about 25% in an elastic wall as compared to a rigid wall (Niroomand Oscuii et al., 2007).

The blood flow velocity calculations in our experiment were done using pulse wave Doppler ultrasound method. Therefore following is a brief explanation of this concept including background and basic physics.

1.8 Physics of Ultrasound

Sound is a form of mechanical energy which travels through matter, as waves in the form of compressions and rarefactions. Sound waves are generated when an object vibrates in a medium. When a sound wave is generated, it causes pressure in the molecules of the medium, so the molecules of the medium compress. As the source of generation of sound moves backward, pressure drops in the medium, and the molecules decompress. After the wave travels through a particular point, the molecules of the medium retain their original position with an overall displacement equalling zero.

The speed of sound is different in different media. It is fastest in solids, and minimum in gasses. It depends on how close the molecules of the medium are to each other. For human beings the audible sound frequency ranges from approximately 10 Hz to 20 KHz, sound with frequency more that 20 KHz inaudible to the human ear and this is known as ultrasound.

Nowadays, ultrasound has a number of applications in medicine and biology, and in industry (Francis A. Duck, Andrew C. Baker, Hazel C. Starritt, c1998; George J. Hademenos, Tarik F. Massoud, 1998; Jorgen Arendt Jensen, 1996). In this work, we dealt with Doppler ultrasound as an accurate method for blood flow measurement.

1.8.1 Doppler Effect

The Doppler Effect is a physical phenomenon named after Austrian physicist *Christian Johann Doppler (1803-1853)*, who first described it in 1842. According to the definition of Doppler Effect, the apparent frequency of a sound wave changes as the distance between the source and observer changes. The change in the frequency is known as the Doppler frequency shift, or simply Doppler shift:

$$f_d = f_t - f_r \qquad 1-17$$

where f_d is the shifted apparent frequency, f_t is the actual transmitted frequency, and f_r is the received frequency. If the source and the observer move toward each other, the wavelength decreases and the frequency increase. Conversely, when the sound source and observer are moved apart, the wavelength increases and the frequency decreases, since the wavelength and frequency are inversely related to each other at a constant velocity.

Doppler Effect is utilized widely in medical imaging to measure the velocity of blood flow in blood vessels. This work is credited to *Satumora* who first conceived this idea (S. Satomura, 1957). In addition to blood flow, Doppler Effect has been extensively used since then to monitor moving structure within the body, for example foetal movement (Peter W. Callen, c2000).

Using the theory of the Doppler effect, Satumora constructed an instrument capable of detecting moving objects. This instrument generates ultrasound and transmits it toward a blood flow. The flow of blood causes the ultrasound to scatter. Based on the observation of shifted frequency between incident and reflected waves, Satumora was able to detect the velocity of flowing blood. Mathematically the Doppler formula can be written as:

$$f_d = \frac{2f_t}{c} v\, cos\theta \qquad 1-18$$

By re-arranging the equation, we can get expression for velocity as:

$$v = \frac{f_d\, c}{2f_t\, cos\theta} \qquad 1-19$$

Here f_t represents the frequency of the incident beam (transducer), v the velocity of the blood in a given direction, c the propagation speed of sound in the tissue, and θ the angle between

the axis of the vessel and the ultrasound beam shown below in Figure 1-8. The above equation 3-3 forms the basis for clinical application of Doppler principle.

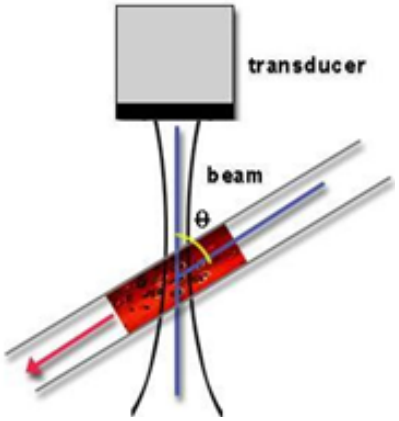

Figure 1-9: Doppler Ultrasound Angle.

1.8.2 Ultrasound in Medicine

Ultrasound was used in medicine first in 1950s, when it was found that ultrasound waves could be used for the detection of parts like tissue layers, tumours and heart structures (Christof Sohn, Hans-Joachim Voigt, Klaus Vetter, 2004). As the technology advanced, non-invasive ultrasound imaging technique has been widely used in medical area. The affordable price of ultrasound equipment and its ability to gather real-time data without invading the body makes this technique very preferable in clinics and hospitals around the world.

As the ultrasound waves pass from one medium to another (e.g., from soft tissue to bone) some of them pass through the boundary separating the two media, and the remaining waves are reflected back. The amount of reflection of these waves depends on the mismatch of blocking of medium for sound waves, or in other words the acoustic impedance, and the angle of incidence of these waves. The acoustic impedance is different for different parts of the body. For the fluids like blood and soft media like soft tissues, the acoustic impedance depends on the density and compressibility of the medium.

Over the past few decades, many different types of ultrasound scanners have been developed to study the inside of the human body. Almost, all these scanners work on basic

principle of pulse-echo imaging in which the instrument sends an ultrasonic pulse into the body and measures the reflections from various interfaces in the wave path. The differences in the echo signals help in collecting data about behaviour of different body parts like blood flow and other parts and organs in our body. The first such scanner was the A-mode scanner in which the ultrasonic beam is directed into the body along the single path. The echo wave received has time delay which is proportional to the distance covered. The echoed wave is plotted versus the strength of original signal. The amplitude of the received wave is determined by various factors such as the interfaces and attenuation of the medium along its path.

There is a more complex and advanced ultrasound system that is capable of displaying two-dimensional images. It is called the B-mode scanner. Such a scanner produces images by holding the transducer with the body. The transducer transmits ultrasound waves into the body and receives the reflected waves. The waves travelling inside the body confront various obstacles and some part of the waves is reflected back. The amount of the reflected wave is proportional to the difference in the acoustic density and compressibility of the tissues. For generation of the image, the brightness of each pixel is determined by the amplitude of the echo signal corresponding to the position in the image (David H. Evans and W.N. McDicken, 2000). In this way particular regions in the image get corresponding brightness depending on echoes and hence produce a final gray scale image.

1.8.3 Doppler Ultrasound

Doppler ultrasound is a medical technique used to perform a non-invasive measurement of blood flow velocity. The instrument used in this technique transmits an ultrasonic beam into the body at a certain frequency. As this wave travels inside the body, it is reflected /scattered in the body and if the object that is causing this reflection and deflection is moving in relation to the ultrasonic transducer, the frequency of the received wave is different from that of the transmitted one as explained in the Doppler Effect theory. The frequency difference is proportional to the relative difference between the object inside

the body and the ultrasonic transducer. There are two modes of operation for Doppler ultrasound: the Continuous Wave (CW) and Pulse Wave (PW) Doppler ultrasound.

1.8.3.1 Continuous Wave Systems

The CW Doppler instrument consists of two separate transducers: a Transmitter (T) that is continuously emitting ultrasound waves and the Receiver (R) continuously picking up the ultrasound waves reflected or scattered from the body tissue. The receiver transducer collects the radiation reflected back from tissue interfaces along the beam path, such as blood vessel walls, as well as the radiation backscattered by the red blood cells (RBCs) within the blood flow. These two transducers are mounted side by side in the same probe with a slight inward inclination so that their beams overlap. The portion of overlap is usually called the sample volume as shown in Figure 1-10.

1.8.3.2 Pulsed Wave Systems

The CW Doppler system lags behind when it comes to resolution. It is possible to check the depth in tissue of the vessel, when two transducer crystals are close to each other. There is a possibility that two vessels, at different depths, accidentally will be at the same image and therefore it will give a wrong frequency distribution. To resolve this issue, the Pulsed Wave (PW) system suggested by Baker (1970) (Jorgen Arendt Jensen, 1996) overcomes the range resolution limitation by controlling the distance from which echoed beam is received. In PW systems there is a single transducer to transmit and receive the ultrasonic wave. In PW mode, a short pulse of ultrasound signal is transmitted at a repetition frequency of f_r. The reflected signal is received with the same transducer but with a time delay of T_d caused in the travel. The delay time T_d is determined by the range of interest or sample volume which gives comparison of transmitted and received beam see Figure 1-10.

The Doppler Sample Volume (DSV) is the three-dimensional region in the path of the transmitted ultrasound beam from which the frequency shift signals are obtained. For the PW Doppler system, the specified zone from which the echoes are received makes up the sample volume. The distance between the transducer and the sample volume is determined by the

time delay between the transmission and reception. The duration of the transmission interval and of the reception interval determines its axial length. The width of the sample volume is linked with the width of the ultrasonic beam at the depth being investigated. Although PW systems have added advantages over CW systems, but that comes with added cost. The Doppler shift that can be detected has limitations. For each Pulse Repetition Frequency (PRF) there is a maximum frequency shift that can be clearly detected $f_{d_{max}=PRF/2}$ (the Nyquist limit, which, represent the maximum frequency threshold). If examination of a deeper sample volume is done that requires higher PRF, it will reveal that the distance travelled by the beam to the sample volume and back is reduced. Since the PRF decreases, the maximum detectable velocity also decreases. The maximum detectable velocity decreases as the transmitted frequency increases for a given depth of sample volume and for a constant angle of incidence. As the heart pumps blood with a periodic pulse throughout the body, the Doppler signal spectrum varies with time following the cardiac cycle, and therefore it is usually plotted as a sonogram, also called a spectrogram, where the horizontal axis represents time, the vertical axis represents frequency and the intensity of the gray scale plot is related to the power of the spectrum (Fish, c1990).

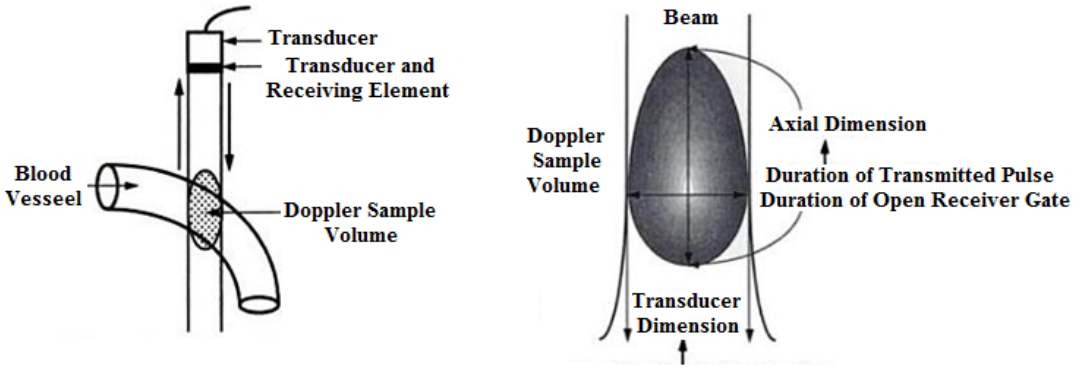

Figure 1-10: Schematic illustration of the Doppler sample volume.

1.9 Computational Fluid Dynamics

Computational Fluid Dynamics (CFD) is an increasingly popular approach to study fluid flows within both common and unique applications. This method uses a numerical approach to solve the mathematical equations involved in the fluid flow. Most of the times, these equations are in the partial differential equations form. Such problems can deal with simple flow characteristics or at times complex factors like turbulence and heat flow.

The CDF equations can be solved by conventional equations which themselves have been well recognized for many years and represent the groundwork of fluid mechanics. Though, with the advancement in numerical methods, the ability to solve the CFD equations numerically has become a widely-used approach due to advancements in computational power.

The applications of CFDs started as early as in 1940's (Milne-Thomson, 1958), but the applications at that time were restricted by the computational power. According to the principles of CFD, having finer and more elements allow for a more accurate prediction of results but that is achieved at the cost of increased computation time. Increasing the complication of the calculations by integrating accurate turbulence equations as well as other factors that may be of research interest can also significantly affect the processing time and ability of the code. That is why CFD has recently been established as an alternative to experimental testing and pure theoretical calculations for research (the latter being applicable for simpler problems only).

As powerful modern processors are arriving, computational power is such that now it is possible to implement complicated simulations on an affordable personal computer within a reasonable period of time. Methods such as parallel processing have decreased the computational effort even further.

CFD has a number of advantages over experimental fluid dynamics (EFD) investigations. The first advantage that CFD has over EFD is in terms of feasibility of design and development. As a typical example consider a simple aerodynamics experiment. A considerable amount of time is required to design the experimental rig and setup to obtain the required data correctly. Collecting values of flow data at more than one location requires the

construction of either a movable data-sampler or multiple data-samplers arranged to cover the region of interest. It is not easy to design conditions where a good sampling of results is obtainable without putting the results beyond accuracy by having the measuring instruments interfere with the fluid flow (Milne-Thomson, 1958). In EFD, a considerable amount of time may also be required to set up experimental conditions to match the conditions of interest, such as changing temperature of the fluids or achieving steady flow. It is also difficult to make adjustments to design parameters for experimental conditions so as to study the variation of measured values with respect to these alterations. On the other hand, in most cases these alterations are quite easy to make in CFD simulations and at most of the times do not require a restarting the solution process. Research on novel algorithms that allow the computer to predict the changes in trends given sufficient initial inputs is still ongoing. However, it should be noted that there are certain restrictions to the CFD methods. Non-uniformity and sudden changes in parameters can affect the solution stability, resulting in slow or non-converging results or a drastic overhaul in the simulation process. One of the major advantages that CFD simulations over experimental methods and theoretical calculations is the span and details available from a simple simulation. In experimental approach, results can provide large-scale values such as changes in pressure over a relatively large test section, the velocity graph or the average velocity at a point of interest and the paths of injected particles. Still, achieving accurate results for the entire model can be costly, time consuming and in some cases impossible to do. As an example, WSS calculation is quite feasible and accurate using the CFD, while it is a fairly challenging task to measure it using experimental methods (Hoi et al., 2004; Q. Wang et al., 2009).

A third advantage that gives the CFD a lead is that extensive simulations at the present time are quite cost-effective compared to the experimental alternative. The programming codes which are used to solve the fluid dynamics equations are commonly available and even basic computers are capable of providing accurate results for complex simulations. Comparatively, the cost required to run the experiments is significantly higher even for simple experiments. That is why the CFD is cost effective and accurate and hence has become a widely-used approach in fluid dynamics calculations.

In spite of all advantages of the CFD discussed above, it should be noted that the experimental methods still play a vital role in research. In a CFD technique there will be a small degree of inaccuracy due to round-off errors, which should preferably be kept to an extremely small value. In numerical computational methods, convergence is a key concern as it may be impossible to achieve a satisfactory degree of convergence without a large demand in computational resources CFD results also require some form of experimental validation to ensure that the proper settings were used and that the code functions as it has been programmed. But on wider scale, the advantages mentioned above have made CFD methods playing a growing role in the research and development process, and thus providing an economically practical option to extend the results beyond the limitations of experimental methods (P. Niyogi, S.K. Chakrabartty, M.K. Laha, 2005).

1.10 Basic Principles of CFD

CFD breaks geometry into small cells and hence aims to solve the governing equations for each cell. These equations describe the physical aspects of fluid flow and for simple flows they are:

(1) Conservation of mass,

(2) Conservation of momentum, and

(3) Conservation of energy if heat is transferred from one point in space to another.

For this study, the basic governing equations of flow are the Navier-Stokes equations (Y.C. Fung, 1990) that determine the conservation of mass and momentum. The process of CFD can be divided into three different phases. The first is the pre-processing stage, in which the domain of calculation is determined and it is decomposed into discrete cells to form a mesh or network of cells. There are several methods involved in creating a best possible mesh that requires knowledge and experience. A finer mesh would provide better results but will need more computational power. To achieve a balance between the calculation accuracy and time, several mesh setting have been tested. This stage also involves determination of the properties of the fluid to be studied. After the fluid medium and the equations that need to be solved have been determined, appropriate boundary conditions are applied to the model. This

is done by constraining the nodes or cells along the domain boundary with known or controllable parameter values. The solution for the rest of the flow domain will be determined from these boundary values. It is wise to note that this stage is likely to require the largest amount of effort. It has been estimated that over 50% of the time spent on a CFD simulation will be devoted to defining the domain geometry and grid generation (P. Niyogi, S.K. Chakrabartty, M.K. Laha, 2005). In this study three idealized geometries that have been created using COMSOL CAD tools. While current codes has helped in making this stage easier, it still requires reasonable knowledge in CAD drawing and mesh setting to be able to create proper meshes to reproduce actual conditions and provide accurate results while keeping computational time to a reasonable level.

In the second stage of CFD, the mesh generated in the previous stage is solved. The solution starts by assigning the cells with an initial value which provides initial estimates for the solution methods. There are several numerical solution techniques like finite difference, finite element and finite volume methods for this purpose. In this work we will use methods based on the finite element solvers in which functions on elements are used to describe the local variations of variable of interest $\emptyset$ across the nodes, which are then used to estimate the value of $\emptyset$ of the element (see below for the definition of $\emptyset$).

All of these methods essentially use a solver algorithm described by (Lee waite, c2006; P. Niyogi, S.K. Chakrabartty, M.K. Laha, 2005),

$$A_c \emptyset_c + \sum_{nb} A_{nb}\, \emptyset_{nb} = Q_c \qquad 1-20$$

The subscripts c and nb refer to the cell centre or grid point and the centres of the neighbouring cells or grid points respectively, A stands for the geometrical parameters (volume, area or distance), fluid properties (density, viscosity, etc.) and also variable values to account for the non-linearity of the equations. Q represents all terms that are known or treated as such within one iteration cycle. $\emptyset$ is the dependent variable, which may stand for the velocity components or pressure that is to be determined from the calculation. An iterative approach is used to solve these equations from the original given values to the point whereby the condition of equation 1-20 is met. The third stage is post-processing stage which

is the final stage in the CFD method in which the data generated from the preceding step is extracted and analysed. Commercially available programs are user-friendly and seek to improve on the visual presentation and manipulation of the data, whereas the traditional codes only export raw data. Commercial programs employ a graphical user interface that among others can show the geometry and grid, vector plots, contour plots, surface plots, particle tracking and other options to suit the user's needs. However, this process requires basic knowledge to interpret the results. The needs of the present level of research and computational power are being met by improving modelling capabilities and user interface.

The main concern of the current study engages the FSI capability of the software, which is presently not supported by a lot of the popular packages available in the market today. It is, therefore, the most important feature for determining which numerical code to use. Since the fluid flows in the current study are laminar, there is little or no need for considerations related to the code's accuracy when solving turbulence. Most of the CFD programs already include the viscosity-strain equations within the code itself. Software's flexibility to encompass user-defined changes and the ability to model transient conditions are some of the considerations to be taken into account.

At present, several software packages like ADINA, ANSYS Multiphysics, FLUENT, ABAQUS and recently COMSOL Multiphysics provide this capability (Structural Mechanics Model: User's Guide, 2008). All these software employ the finite-element method to solve the flow equations. This is the preferred method for solving FSI simulations of structural problems as it is a well established and the best method available. In this study we will develop a novel coupling environment of COMSOL Multiphysics with FSI capability to use in the computational blood flow simulation in an elastic blood vessel. The most important feature of this software is that it is capable of solving both the fluid and solid models within one single program. The coupling method is two-way, in which the fluid domain is fully coupled with the solid structure, which subsequently allows for highly non-linear problems to be modelled. A stronger interaction than an iterative scheme between the fluid and the solid model is resulted due to a fully coupled model. Although this type may acquire more computational efforts to resolve, yet the results have the propensity to be accurate. With the

amalgam of the flow and solid equations into a single system to be solved by using the finite element method, this software currently allows to simulate more complex flow conditions and highly non-linear behaviour.

1.11 Previous Studies on Fluid-Structural Interaction (FSI)

Fluid-structure interaction (FSI) has been an important field of study for many years. It is a technique used in numerical problems to provide an understanding of the impact of the flow on structures, both within and surrounding the flow. Due to the drastic increase in computing power over the last decade, numerical methods are becoming increasingly more effective. This has resulted in the increased utilization and research in the field of numerical methods to predict FSI motions and other responses. Originally, this method was used to simulate cases of aeroelasticity for aerodynamic research (Milne-Thomson, 1958), but recently it has been actively integrated in various biomechanical researches, including those involving blood flows through aneurysms arteries (Bazilevs et al., 2010; Takizawa, Christopher, Tezduyar, & Sathe, 2010; Torii et al., 2010). The integration of FSI into the blood flow models is considered to be a big step in research field carried on arteries wall diseases as it allows the researcher to locate where arterial lesions are most likely to occur and how they happen; offering a method to understand the problem and to prevent potentially fatal results.

It has been an established observation that the presence of an aneurysm within the artery can result in a high region of blood pressure, particularly where the occlusion is at bifurcations or curvatures arteries (Eriksson, Kroon, & Holzapfel, 2009; Hashimoto et al., 2006; Krex et al., 2001; Sekhar & Heros, 1981). Various physiological experiments conducted recently have shown that the hemodynamic forces play an important role of initiation, formation and growth of an ICA and other vascular diseases, such as atherosclerosis (Malek, Alper, and Izumo, 1999).

Numerous studies focusing on the CFD, recommended geometry movement and provided immense information that is not available in clinical practice (Lee waite, c2006). The introduction of Arbitrary Lagrangian–Eulerian formulation (ALE) methods (Duarte,

Gormaz, & Natesan, 2004) (described in the next section) has helped ease the studies of moving boundary. Lately, hemodynamic simulations with patient-specific vascular models have become popular and a large number of studies have been conducted. In one of the earlier studies as reported in (Taylor, Hughes, & Zarins, 1998), hemodynamic simulations were carried out with the main focus on the abdominal aorta in which the geometry was extracted from the magnetic resonance imaging (MRI) data. In (Taylor et al., 1998) as well as in various studies from the same period, the vascular walls were assumed to be rigid. Only the most recent studies have taken into account the deformation of the vascular walls in Hemodynamic simulations. For instance in (Alberto Figueroa, Baek, Taylor, & Humphrey, 2009; Bazilevs et al., 2010; Pericevic, Lally, Toner, & Kelly, 2009), blood flow computations were carried out with moving boundaries where either a theoretical or an empirical model based on *in vivo* measurements is used to prescribe the motion. Computations of the FSI between blood flows and blood vessels were reported in (Di Martino et al., 2001; Moosavi, Fatouraee, & Katoozian, 2009; Watanabe, Hisada, Sugiura, Okada, & Fukunari, 2002). These studies mainly focused on the heart and abdominal aorta where the deformations are comparatively large. On the other hand, FSI analysis of cerebral arteries is not so common because the cerebral arteries deform less and are smaller than other arteries and consequently have little influence. However, no matter how small, these small deformations affect and interact with the dynamics of blood flow in the brain and this makes the arterial-wall deformations in cerebral arteries important.

With special focus on modeling the structure influence of moving boundaries of aneurysmatic arteries with implementation of FSI and ALE formulation (Flori, Giudicelli, & Di Martino, 2009; Guivier-Curien, Deplano, & Bertrand, 2009; Krittian, Janoske, Oertel, & Böhlke, 2010), studies have been performed with a 3D code-coupling approach to simulate cardiovascular blood flow and stenosed arteries (Koh, Kang, Cho, & Yoo, 2009). Research using FSI analysis on many types of aneurysms arteries was conducted and provided analysis on wall deformation, stress distribution and flow characteristics with patient-specific geometry constructed from clinical magnetic resonance images (MRI), computer tomography (CT), and 3D ultrasound images (Oshima et al., 2001; Torii, Oshima, Kobayashi, Takagi, &

Tezduyar, 2007a), or by using idealized realistic geometry with different sizes and shapes of arterial aneurysms (Bazilevs, Gohean, Hughes, Moser, & Zhang, 2009; De Hart, Peters, Schreurs, & Baaijens, 2003) . These researches have managed to show that a high WSS exists around the neck region of the aneurysms and at the aneurysm fundus (the farthest part from the opening of a sac or hollow artery). Moreover, these studies reveal that the aneurysms have a significantly thinner wall thickness compared with the parent artery, which increases the probability of rupture see Figure 1-11.

The aneurysms in the mentioned studies already existed in the geometries before the simulation begins, whether or not the geometries were constructed from the patients' medical images or represented simplified clinical geometries.

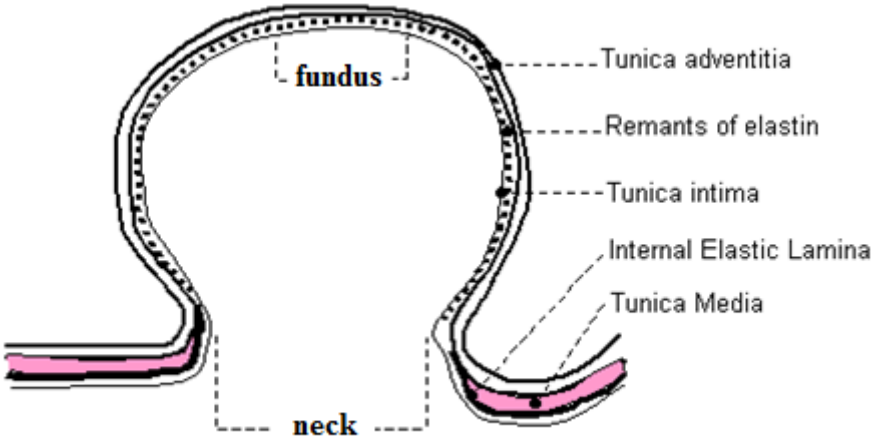

Figure 1-11: A sketch of a saccular aneurysm cross section.

(George J. Hademenos, Tarik F. Massoud 1998)

1.12 Arbitrary Lagrangian–Eulerian Methods

For numerical simulation of multi-dimensional problems in fluid dynamics and nonlinear solid mechanics, an establishment of strong interaction between fluid-solid, solid-fluid or fluid-structure interface is frequently required. When developing a computer code for simulating problems in this class, the choice of an appropriate kinematical description of the continuum is an essentially important consideration. In fact, such a choice determines the

relationship between the deforming continuum and the finite grid or network of computing zones, and thus conditions the ability of the numerical method to deal with large distortions and provides an accurate resolution of material interfaces and mobile boundaries (A Huerta, M Casteleiro and H. Alder, 1993).

Arbitrary Lagrangian Eulerian (ALE) is an approach employed to solve problems in engineering in which the use of the classical Lagrangian and Eulerian reference frames is combined. Mostly it is used in the analysis of FSI systems. Generally, it is favourable (if not necessary) to use an ALE approach to analyze the structure (and fluid) motions if material strain rate is significant. ALE becomes very useful when analyzing structural motions in cases where the structure is severely deformed, like an impact problem or for the analysis of a very flexible structure.

The Lagrangian reference frame is most commonly used in solid mechanics (Duarte et al., 2004). It sets up a reference frame by fixing a grid to the material of interest and as the material deforms the grid deforms with it. It also assists in identifying the exact dislocation of each particle which becomes very helpful in tracking motions in solid mechanics. This method automatically adjusts the conservation of mass since the individual sections of the grid always contain the same (amount of) mass. In structure motions with large deformation, the grid becomes extremely distorted and the integration time steps decreases since they are based on the size of the smallest section of the grid.

The Eulerian reference frame is a typical framework, fixed in space, used in the analysis of fluid mechanics problems (Duarte et al., 2004). It allows the material to flow through the grid conveniently. However, the Eulerian reference frame is unable to track the path of individual particles. Therefore, for solving motion predictions through the Eulerian approach, the solution is generally implemented for the net flow through a certain area. For this reason, in the Eulerian method, conservation of mass is adjusted by measuring the flux in and out of each grid section. Therefore, the key disadvantage of the Eulerian system is that it does not track the path of any element, particularly the fluid free surfaces. ALE approach combines the use of the two reference frames. It allows for a grid that is both flexible and capable of handling flow of materials through it. In fact, it takes the advantages of both

reference frames and combines them into one (Duarte et al., 2004; Y. Wang, Zhao, Mao, & Wang, 2007). This approach proves to be helpful in problems dealing with large deformations in solid mechanics and in fluid-structure interaction. It allows the grid to track the material to some extent, however, when the grid deforms excessively and alters the aspect ratio of the grid beyond an acceptable point, it adjusts the grid and measures the flux of the material during the adjustment of the grid. The main challenge while using the ALE approach is to decide how much the grid should be allowed to deform and how much flux to allow. This can be resolved by setting a limit on the distortion of a segment of a grid and once it deforms past that limit then that part of the grid is interconnected or re-meshed.

While using the ALE, the input of several variables is required to allow the numerical model to compare closely to the real-world situation and to let the governing equations to work. There are numerous variables that must be ascribed with size, boundary considerations, free surfaces and starting velocities. Fundamental characteristics of the material are also important which include density, viscosity, strength, Young's modulus, shear modulus and bulk modulus. These variables are necessary for input in order to assure the accuracy of the governing equations.

For the modeling of FSI the use of several governing equations like the conservation of momentum is necessary. This is usually taken care of with the Navier-Stokes equations. Conservation of mass is important when re-meshing occurs. When the mesh stays constant, as in an Eulerian approach, there is no need for conservation of mass since it stays constant by default (as there is no mass flux). Conservation of energy is another important consideration. Lastly, boundary conditions need to be taken into account.

Chapter 2 COMPUTIATIONAL FSI MODELING OF BLOOD FLOW

This chapter aims to provide a description of the governing mathematical equations and the algorithm developed for the computational FSI modeling of blood flow and the model geometries used in the study. A synopsis of the mathematical equations used for the solution process and the boundary conditions has also been incorporated in this chapter. Methods used to attain the solution, as well as a discussion on the FSI coupling method are also included in this chapter.

2.1 Model Geometries

As mentioned previously, the saccular cerebral aneurysms usually forms and grows at arterial forks with connection to the circle of Willis, particularly in the anterior choroid artery junction, the anterior communicating artery and the middle cerebral arteries' main bifurcation (Steiger, 1990), where the internal elastic membrane is to some extent destroyed and where the arterial media layer are weakened (Austin, Fisher, Dickson, Anderson, & Richardson, 1993).

The current study scrutinizes the hemodynamic flow, wall deformations and WSS in straight, curvature and bifurcated vessels computationally, and examines their correlation with the influence of the mechanical properties on a saccular ICA formation, growth, and rupture.

Idealized saccular aneurysms were modeled along the parent vessels and daughter branches using the CAD drawing tools in COMSOL Multiphysics finite element software package V 3.5a (COMSOL Inc., Burlington, MA, USA) (Structural Mechanics Model: User's Guide, 2008).

The first model to be regarded as a straight elastic tube with undeformed inner diameter of D $= 3\,mm$, length of $L = 20\,mm$, and the wall thickness of $h = 0.2\,mm$, as shown in Figure 2.1 (Kroon & Holzapfel, 2008).

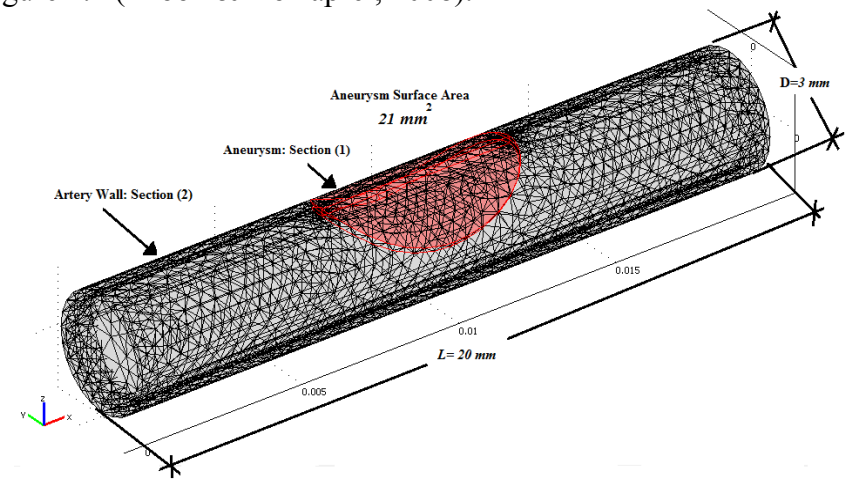

Figure 2-1: Geometry and section divisions of saccular aneurysm.

The second model was a segment of curved artery (Foutrakis, Yonas, & Sclabassi, 1999; Torii, Oshima, Kobayashi, Takagi, & Tezduyar, 2007a), which had the same inner diameter of 3 mm and length of 23 mm with a 90 degree curvature as shown in Figure 2-2.

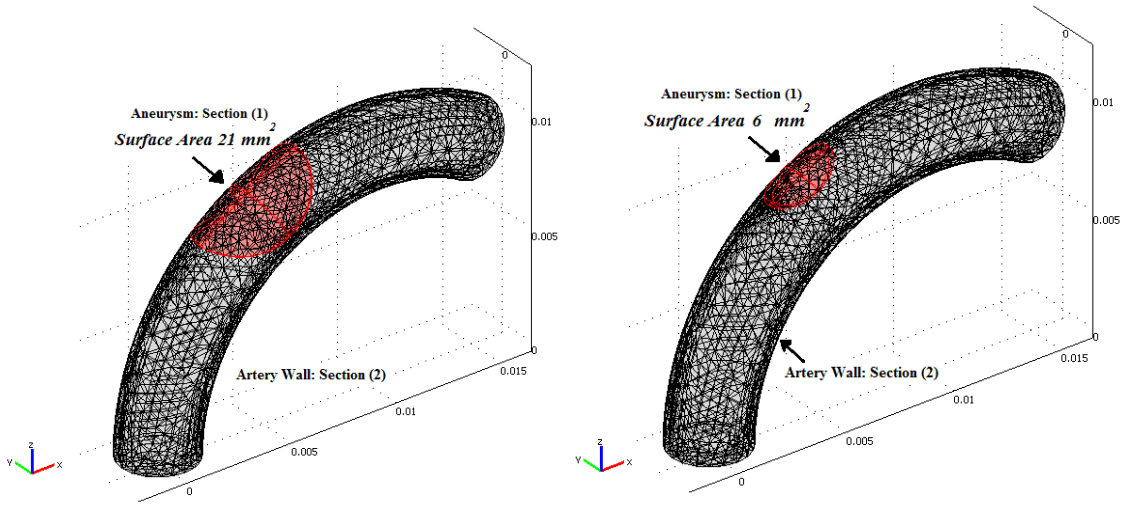

Figure 2-2: Geometry and section divisions of saccular aneurysm in a curved artery.

The last two models represent part of the middle cerebral artery (MCA) bifurcation, which is among the common locations of cerebral aneurysm as shown in Figure 2-3 (Foutrakis et al., 1999) . The inner diameter of the parent artery and two daughter arteries is assumed to be the same as earlier geometries of 3 mm and same daughter curvature in order to be compared with previous geometries and also with same two neck size, large as shown in Figure 2-3A and small neck size as shown in Figure 2-3B .

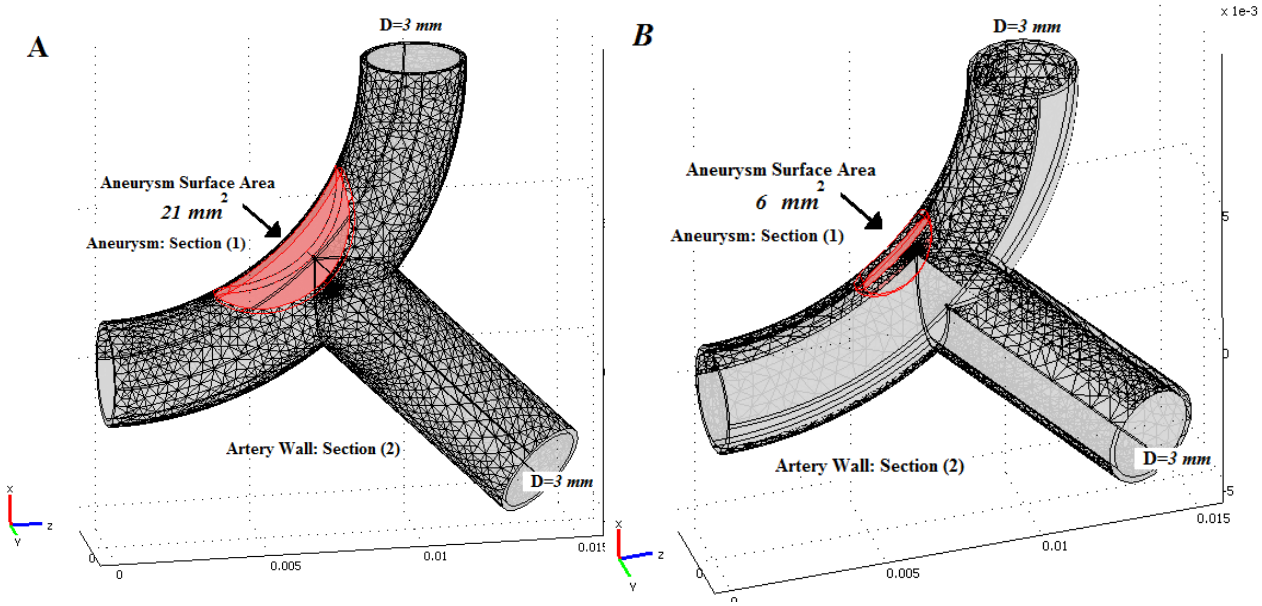

Figure 2-3: Geometry and section divisions of simplified saccular aneurysm in bifurcation geometry, with large neck size (A) and small neck size (B).

In two types of Bifurcation Aneurysm with large neck size (A) and small neck size (B). Based on wall mechanical properties, each geometry was divided into two sections. In this research, it was observed that the aneurysm considered as diseased part had different mechanical properties than the arterial wall, however both of them were assumed to have the same wall thickness of $0.2\,mm$ (Torii et al., 2010). On the other hand, the healthy arterial wall elasticity was assumed to be $6\,MPa$ for all studied models, which is a much higher elasticity than the aneurysm's wall $0.25 - 0.0625\,MPa$.

The introduction of aneurysm as a diseased part into the geometry at the median of the artery consisted of two sizes: large surface area of ($S_l = 21\ \text{mm}^2$), and small surface

area of ($S_s = 6\,\mathrm{mm}^2$). The chosen aneurysms had different mechanical properties along with a range of values that had been changed to the values from $0.25\ MPa$ to $0.0625\ MPa$ (Hashimoto et al., 2006; Kroon & Holzapfel, 2008; Valentín & Humphrey, 2009) for a more extensive coverage of biomechanical properties of diseased arteries. The severity of the aneurysm was determined by comparing the amount of the diseased surface area and the degree of loss suffered by their mechanical properties with the healthy arterial wall. For this purpose, aneurysms with different surface areas and mechanical properties were planted in a healthy blood vessel to study their effects on the formation and growth of the aneurysms. Lastly, it is imperative to mention that in all cases, the geometries were considered as cylindrical elastic tube and were generated by COMSOL.

2.2 Governing Equations

2.2.1 Flow Modeling

The Navier-Stokes equations are the principal equations to model fluid flow. Under the conditions of an incompressible material, the flow was assumed to be steady so that the time derivative is neglected, $\rho_f g$ denotes the gravitational external force which is assumed to be zero, the Navier-Stokes equations 1-12, simplify to the continuity equation (the conservation of mass) equation 2-1 and the conservation of momentum equation 2-2.

$$\frac{\partial u_i}{\partial x_i} = 0 \qquad 2-1$$

And

$$\rho . u_j \frac{\partial u_j}{\partial x_j} = -\frac{\partial P}{\partial x_i} + \mu \frac{\partial^2 u_i}{\partial x_j \partial x_j} \qquad 2-2$$

where, u_i = (u, v, w) is the local velocity, x_i = (x, y, z) is the length coordinate, p is the fluid pressure, μ is the dynamic viscosity. The last expression in equation 2-2 denotes the surface force and e_{ij} is the strain rate tensor which generated the stress in the elastic material see equation .

The blood-mimicking fluid was modeled in isothermal, incompressible and Newtonian (constant viscosity) conditions, and the stress tensor is generated in the blood defined by the constitutive equations is given by:

$$\sigma_{ij} = -p\delta_{ij} + 2\mu e_{ij} \qquad 2-3$$

where σ_{ij} is the stress tensor, and $\mu = 3.5 \times 10^{-3} m^2/sec$ is the fluid viscosity, and δ_{ij} is the knockers delta (Lee & Xu, 2002; Torii, Oshima, Kobayashi, Takagi, & Tezduyar, 2007a; Y.C. Fung, 1993).

2.2.2 Elastic Vessel Wall Modeling

The governing equations for the motion of an elastic solid are mathematically described by the following equation (Torii, Oshima, Kobayashi, Takagi, & Tezduyar, 2007a):

$$\rho_w \frac{\partial^2 \varepsilon_{ij}}{\partial t^2} = \frac{\partial \sigma_{ij}}{\partial x_j} + \rho_w F_i \quad for\ i = 1,2,3 \qquad 2-4$$

where ε_{ij} and σ_{ij} are the components of the displacements and stress tensor in a solid respectively, ρ_w is the solid density, F_i are the components of body force acting on solid, and, σ_{ij} can be obtained from constitutive equation of the material.

Solid material deformation is produced as a result of flow, and according to the law of conservation of energy, the energy will store inside the material. Strain energy density function W can be used to measure the energy stored in the material as a result of deformation that can be written as:

$$S_{ij} = \frac{\partial W}{\partial \varepsilon_{ij}} \qquad i,j = 1,2,3 \qquad 2-5$$

where S_{ij} and ε_{ij}, are the components of the second Piola-Kirchhoff stress tensor, and the Green-Lagrange strain tensor see equation , respectively. Under small deformations, the Green-Lagrange strain tensor is reduced into the infinitesimal strain tensor:

Under infinitesimal deformations both stresses are identical. Second Piola-Kirchhoff stress tensor is related to Cauchy and total stress tensors as follows:

$$\tau_{ij} = -p\bar{I} + \sigma_{ij} \qquad 2-7$$

where $\tau_{ij}, \bar{I}$, are the components of the total stress and the identity unit tensors, respectively, and p is the hydrostatic pressure.

A single-layered arterial wall was assumed throughout the entire model. The artery was modeled as a hyper-elastic material or Neo-Hookean elastic solid material which shows nonlinear dependence of stress-strain behaviour of materials undergoing large deformations (Eriksson et al., 2009).

A hyperelastic or Green elastic material is basically a type of constitutive model used for ideally elastic material for which the stress-strain relationship originates from a strain energy density function. The hyperelastic material is a special case of a Cauchy elastic material (Niroomand Oscuii et al., 2007). The strain energy density function for neo-Hookean material is considered a special case of a Cauchy elastic material that can be written as:

$$W = \frac{G}{2}(\bar{I} - 3) + \frac{k}{2}(J - 1)^2 \qquad 2 - 8$$

Where G, k are the shears and bulk modulus respectively, representing the material properties, J is the ratio of the deformed elastic volume over the undeformed volume and $\bar{I}$ is the first invariant of the left Cauchy-Green deformation tensor defined as:

$$\bar{I} = \lambda_1^2 + \lambda_2^2 + \lambda_3^3 \qquad 2 - 9$$

The artery was modeled as an incompressible material since the incompressibility is a reasonable assumption because biological tissues contain mostly water, which is incompressible at physiologic pressures. The material is incompressible in the sense that its resistance to volume changes in orders of magnitude greater than its resistance to shape changes. The incompressibility assumption has been employed by most of the investigators for arterial mechanics (Carew, Vaishnav, & Patel, 1968), confirming this assumption by measuring the change in the total volume of arterial tissue during deformation (Chuong & Fung, 1984). For a Neo-Hookean incompressible material $J=1$, then

$$W = \frac{G}{2}(\bar{I} - 3) \qquad 2-10$$

Using the relation for the Cauchy stress for an incompressible neo-Hookean material we get

$$\sigma_{ij} = \lambda e_{\alpha\alpha}\delta_{ij} + 2G\varepsilon_{ij} \qquad 2-11$$

In terms of the principal stretches, the Cauchy stress differences for an incompressible hyperelastic material, which is a type of constitutive model for ideally elastic material for which the stress-strain relationship derives from a strain energy density function. The hyperelastic material is a special case of a Cauchy elastic material are given by (Torii, Oshima, Kobayashi, Takagi, & Tezduyar, 2007a; Y.C. Fung, 1993):

$$\sigma_{11} - \sigma_{33} = \lambda_1 \frac{\partial W}{\partial \lambda_1} - \lambda_3 \frac{\partial W}{\partial \lambda_3} \qquad 2-12$$

$$\sigma_{22} - \sigma_{33} = \lambda_2 \frac{\partial W}{\partial \lambda_3} - \lambda_3 \frac{\partial W}{\partial \lambda_3} \qquad 2-13$$

The most widely used criterion is the *Von Mises Stress* distortion energy criterion for ductile materials, where the Von Mises stress or equivalent tensile stress, $\sigma_{Von\ Mises}$, a scalar stress value that can be computed from the stress tensor which is used to predict yielding of materials under any loading condition from results of simple uniaxial tensile tests. The quantities $\bar{I} = (I_1, I_2, I_3)$ are the stress invariants given same stress state in all 3D coordinated systems.

According to the Von Mises theory, even though none of the primary stresses exceeds the yield stress of the material, it is possible for yielding to stem from the combination of stresses. The Von Mises stress combines these three stresses into an equivalent stress, which is then compared to the yield stress of the material given as:

$$\sigma_{Von\ Mises} = \frac{\sqrt{2}}{2}\sqrt{(\sigma_1 - \sigma_2)^2 + (\sigma_2 - \sigma_3)^2 + (\sigma_3 - \sigma_1)^2} \qquad 2-14$$

where, $\sigma_1, \sigma_2,$ and σ_3 are the three principal stresses.

2.3 Boundary Conditions

For fluid model, steady flow velocity profile was assumed at the inflow boundaries with a uniform velocity of $50\ cm/s$. Due to the no-slip boundary condition assumption at the artery walls (with no porosity), the fluid is believed not to have penetrated through the walls as it flows along the vessel. Due to the nature of blood flow in the cerebral arteries, a uniform velocity profile was chosen with parabolic laminar profile (Wilmer W. Nichols and Michael F. O'Rourke, 1997,1990,1998). The outflow was set with various pressure values starting from $20\ mmHg$ and increased to $(200\ mmHg)$ with a $20\ mmHg$ step size for all models (Torii, Oshima, Kobayashi, Takagi, & Tezduyar, 2007a). These boundary conditions correspond to a characteristic flow setting for a typical human cardiac cycle for normal as well as hypertension high blood pressure.

In the case of the solid model which corresponds to the artery walls, a Young modulus of elasticity of $E = 6.2\ MPa$ and Poisson ratio of $\nu = 0.45$ were used in a healthy arterial wall, where the young modulus is assumed to be fixed with the value of $E = 6.2\ MPa$ for the healthy part of the arterial wall and this value was reduced down to $E = 0.25\ MPa$ to introduce the aneurysm part in the healthy artery. Additionally the aneurysm part were varies from $E = 0.25\ MPa$ and decreases down to $E = 0.0625\ MPa$ with four equal reduction steps to study the influence of the mechanical properties on aneurysm formation and growth. A full summary of the boundary conditions is shown in table 2.1.

Domain	Parameter	Value
Artery	Module	Structural Mechanical Modulus- Solid Stress-Strain
	Material Model	Hyperelastic Neo-Hookean
	Initial Shear Modulus	$G = 1.74\ MPa$
	Initial Bulk Modulus	$k = 34.7\ MPa$
	Young Modulus	$E = 6.2\ MPa$
	Density	$\rho = 1000\ Kg/m^3$
	Poisson's Ratio	0.45

Aneurysm	Module	Structural Mechanical Modulus- Solid Stress-Strain
	Model Material	Hyperelastic Neo-Hookean
	Initial Shear Modulus	$G = 0.075, 0.056, 0.037, and\ 0.018 MPa$
	Initial Bulk Modulus	$k = 1.5, 1.12, 0.74, and\ 0.37 MPa$
	Young Modulus	$E = 0.25, 0.1875, 0.125, and\ 0.0625\ MPa$
	Poisson's Ratio	0.33
	Density	$\rho = 960\ Kg/m^3$
Blood	Model Material	Incompressible Navier-Stokes
	Density	$\rho = 1060\ Kg/m^3$
	Viscosity	$\mu = 3.5\ mPa.Sec$

Table 2.1: Model Parameters.

2.4 Computational Details

COMSOL is a commercial CFD package that is utilized in this study to construct the discretised equations representing blood flow, artery and aneurysm into a structured mesh in accordance with the finite element method.

Finite element method is employed to solve the model equations in which finite element technique divides a geometry of a complex shape into smaller, simpler shaped elements, and computes these equations individually on each element. The geometries in this study consisted of three domains; the arterial wall and the aneurysm were assumed to be a composite geometry, in which COMSOL treated the system as one solid object, whereas blood as a fluid is the third domain. Thus for these three different domains, the software provided continuity for the displacement and provided a conforming mesh at the artery-aneurysm (Structural Mechanics Model: User's Guide, 2008). The three sub-domains were kept preserved in order to dispense different material properties for the artery, aneurysm, and blood domains. One of the major important factors to provide an accurate solution is the number of elements applied to establish an optimum computational result, which would trade off with the time required for each simulation. A fine mesh setting was used for the artery and aneurysm domains. The number of mesh elements varied from 150000 to 300000 with the maximum element size of 0.8 mm taking into consideration the time required for each

simulation. The COMSOL software package provides two methods for performing FSI: one-way coupling and two-way coupling. The recommended two-way coupling method was employed in this study by utilising the COMSOL Arbitrary Lagrangian-Eulerian (ALE) formulation. In this method, the fluid and solid domains are solved concurrently. This is carried out by creating fluid and solid geometries individually, applying the appropriate meshing and then applying the appropriate boundary conditions. These conditions are applied on the appropriate boundary where FSI allows the transfer of fluid-solid, solid-fluid, solid displacements and velocities changes across the geometry. This FSI process efficiently yields a two-way coupling result. Finally to solve the models, a *GMRES* solver "Generalized Minimal Residual (GMRES) algorithm method (Fortin & Fortin, 1990)" was used in all simulations allowing us for an accurate comparison between the simulations. This solver is a set of routines for solving asymmetrical hemodynamics systems (Youcef Saad, Martin H. Schultz, 1986). Finally, the simulations were runs on Intel® Core™2 Quad Processor Q8200 (4M Cache, 2.5 GHz, 1333 MHz FSB) with 8Mbyte desktop, where 6-12 hours were needed to finish one run.

2.5 Formulation of the Problem

A computational finite element analysis of three different types of idealized intracranial saccular aneurysms, including: 1) side-walled aneurysm, 2) curve-walled aneurysm and 3) bifurcation aneurysm was carried out. These types of aneurysms were modeled with the parent vessel and daughter branches and truncated into two different sizes of aneurysms surface areas along the vasculature. As part of this study, the effects different geometries on the formation and growth of ICAs were investigated. We focused in this study on two main factors: The first factor is WSS, which was reported as an important factor in the initiation and growth of aneurysms (Torii, Oshima, Kobayashi, Takagi, & Tezduyar, 2007a). The second factor is vessel wall deformation and is related to prediction of the aneurysm's rupture using Laplace law (Canham & Ferguson, 1985; Humphrey & Kyriacou, 1996).

Chapter 3 MODEL VALIDATIONS

This chapter covers the methods for the experimental verification of the developed numerical FSI model. Model validation has been done with two choosing experimental results. First validation was based on our experimental work performed on simple multichannel rigid wall blood vessels phantom that we created in our lab. In this experimental study only rigid wall simulated vessel was used. This is because it allows limited experimental effort and lowers the difficulty to construct an elastic multichannel blood vessel. The second validation was done using a published experimental data on a straight elastic dog mid-abdominal aorta. This chapter highlights and explains the details of the construction of the phantom, flow system, experimental preparation and velocity measurement. This chapter also covers the validation model and the computational model details with the boundary conditions. At the end, the FSI model simulation results for a straight dog mid-abdominal aorta have been validated against published experimental data.

The modelling technique developed in this study presents a starting point to modelling and understanding cerebral hemodynamics and there is a very large scope for validation of the model before it possibly will become accepted as a clinical tool. There is also a wide scope of extension of the model to take in other aspects of neurologic dysfunction such as brain metabolism (Aubert, Costalat, Duffau, & Benali, 2002; Vatov et al., 2006) .

In the first part of the study, a number of simulations investigating the velocity of blood flow in a rigid wall multichannel blood vessel geometry and wall deformation in a segment of dog aorta have been performed in the second part. To validate the simulations, these results were compared with our experimental work which was performed on a rigid wall blood vessels phantom, and published experimental work was done on an elastic dog aorta. The second part of the study was applied the FSI developed model on idealized clinical geometry to study the formation and growth in cerebral aneurysms.

3.1 Validation of the Numerical Model - Method One: Comparison with Experimental Data

3.1.1 Experimental Model

For a validation purpose we built several multichannel blood vessel phantoms, and a steady flow circulation system. In the following sections we will describe our phantoms and the flow system and their building stages.

3.1.1.1 Rigid-Wall Phantom

The phantom used in this part of the study shown in Figure 3-1 below, has been built from transparent plastic (Rexolite® 1422). This material was found to be one of the best ultrasound transparent solid materials in high frequency ultrasound experiments (Yeh, Ferrara, & Kruse, 2004). The phantom consists of two slabs with dimensions of 75×45×6 mm.

Figure 3-1: Rexolite® multichannel blood vessel phantom.

On one slab we carved a simple multichannel blood vessel network. The carving was carried out using manual fixed drill with drill tip diameter of 2 mm. The carved was therefore 2 mm in depth. It was then carefully polished to obtain smooth flow channels.

After carving, the next step of building the phantom was to set up a flow system by inserting an inlet and outlet short plastic tubes with 2.5 mm outer diameter, after increasing the width at the two ends of the phantom to match the tubes' outer diameter size. Then the two Rexolite® slabs were glued together to obtain the flow channels and compressed with a manual compressor, left overnight for drying. The entire outer edges of the phantom were enclosed by the same glue to create an impermeable seal. For additional sealing and structural support, the junction was properly sealed and glued.

In addition, it is important to mention that we had to redo the last stage more than once, trying to prevent any fluid leakage from anywhere in the phantom.

3.1.1.2 Steady Flow System

To determine the practicability of measurements of velocity of fluid flow, an experimental steady flow system was built. To achieve this, 2.5 millimetre diameter clear plastic tubing was fabricated into detachable tubing connectors. A schematic diagram of the experimental model is shown in Figure 3-2.

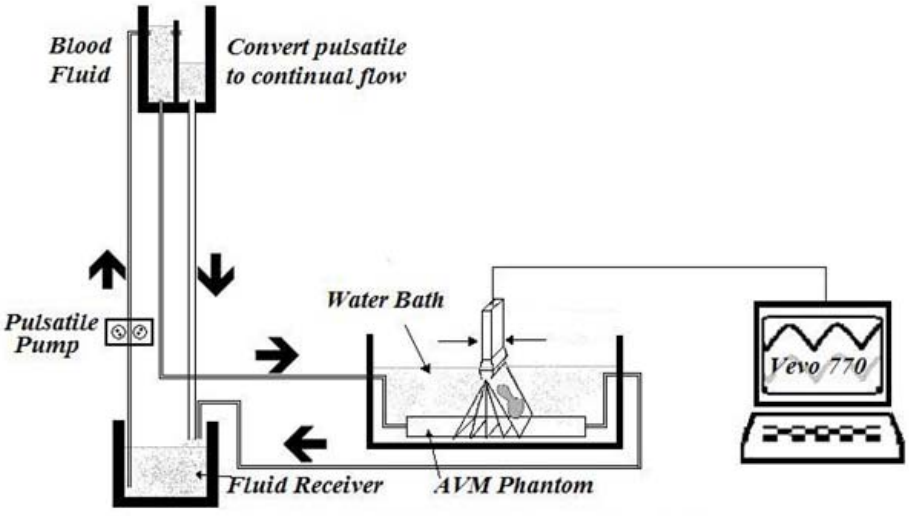

Figure 3-2: A schematic diagram of the experimental flow system.

The flow system tubing was connected into the two ends of the phantom so that the lumen, inside of the vessel, was continuous. After connecting phantom to the flow system, a rotary Masterflex® portable peristaltic pulsatile pump (Cole-Parmer Canada Inc) was used to

provide the pulsed pressure required to drive the fluid through the flow system. The pump was placed on the working surface. The lab counter level was used as a so-called “floor level” as it was about the same level as the phantom. A photograph of the experimental model is shown in Figure 3-3.

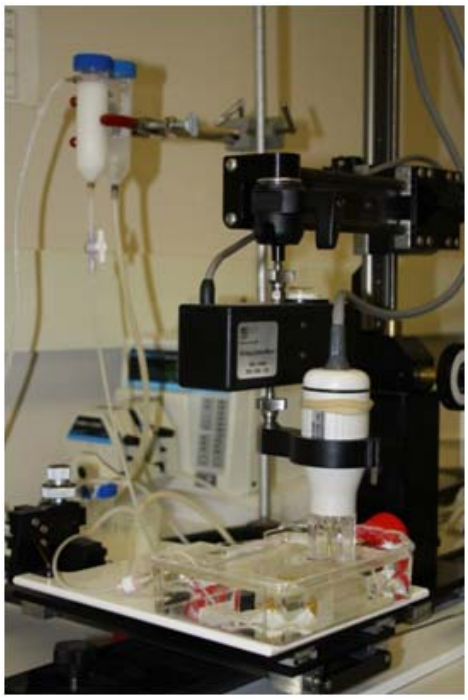

Figure 3-3: Flow System Setup. The flow system was used to measure the pulse wave velocity in multichannel blood vessel phantom.

Since in our experiment the flow velocity measurement was performed on steady flow, therefore a modification was required on the flow system to convert the fluid flow from pulsatile flow to continuous flow. That was achieved by having two fluid containers, called a head tank container and overflow container. The pulsatile pump pumped the fluid from the receiver container at the floor level to the head container having 45 ml capacity that is opened at some point to the overflow container. Figure 3-4 shows a photograph of the two head containers and overflow containers. With those, we had effectively generated a fluid column of constant height, allowing for a continuous and steady flow. The overflow container collected the overflow fluid from the head container and returned to the floor level

reservoir. A gravity-driven flow system was constructed from plastic tubing to deliver steady fluid flow.

The flow velocity was controlled by the manual valve tap placed in the outset of the outlet head container and the elevation of the head container as seen in Figure 3-4.

Figure 3-4: A photograph shows the head and over flow containers that were used to convert the pulsatile flow to steady flow, as well as the manual valve tap that was used to control the fluid flow.

As part of the experiment, the rigid-wall phantom was immersed in a water tank, in order to have coupling for the ultrasound signal between the ultrasound transducer and the phantom, and fixed at same position by adhesive water proof tape. The fluid used inside the vessel was a blood-mimicking fluid model 046 from (CSP® Medical Inc., London Ontario). Table 3-1 shows the blood-mimicking fluid specifications.

Property	**Human Blood (37°C)**	**Model 046 Blood Mimicking Fluid**
Viscosity $mPa.sec$	3.5	4 ± 0.5
DensityKg/m^3	1050	1045
Velocity m/sec	1583	1570 ±30
Attenuation $dB/cm \quad MHz$	0.15	<0.1
Fluid Properties	non Newtonian	Newtonian

Table 3-1: Blood-Mimicking Fluid Model 046 Specifications.

3.1.1.3 High Frequency Ultrasound Scanner

A high frequency ultrasound scanner *vivo770*™ (VisualSonics Inc, Toronto, Ontario, Canada) with 25 MHz single element transducer was used to perform flow velocity measurement on the constructed phantom. In this experiment, pulsed wave Doppler mode was used in all measurements. The Doppler incident angle was fixed at 60 degree, as shown in Figure 3-5, in the direction of the fluid flow. This angle was experimentally selected to achieve better image quality from feedback (reflected signals) as well as a good pulse wave Doppler velocity signal, with very small artefact (mirroring), where, it is a recommended Doppler scanning angle in the clinical practices (Fish, c1990). This angel was kept uniformed in all experimental measurements. The above-mentioned scanner has a feature of motorized scan, however, in this study we controlled the transducer manually in a different selected point on the phantom to make our measurements.

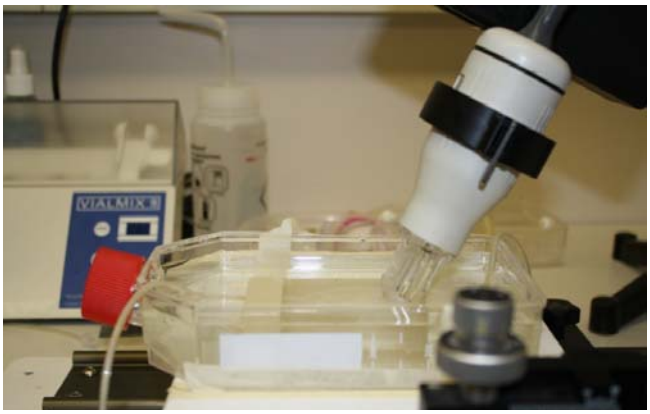

Figure 3-5: A photograph illustrate the transducer angle with the phantom for the pulse wave velocity measurements.

3.1.1.4 Experimental Preparations

Pulsed wave velocity measurement has been performed on the rigid-wall Rexolite® phantom that has been installed in the flow system filled up by a blood-mimicking fluid as mentioned earlier. The flow system had to be sealed properly to prevent any leakage. In order to check any flow leak in or out of the phantom, the flow system was tested with deionised water that was colored using regular red ink in order to be able to see the flow inside the phantom as well as observe any water leak, as the water is more prone to micro leaks than the blood-mimicking fluid due to its very low viscosity. Nevertheless, before recording any

velocity, the flow velocity was selected and monitored by adjusting the head container elevation and the tap valve to maintain a steady flow velocity. The fluid flow system was allowed to stabilize for 2-3 hours prior before any velocity measurements were taken. As for environmental temperature, it was assumed to be constant at 22 °C room temperature.

Furthermore, in order to track the measurements position and reduce the experimental measure mental errors in the velocity measurements, the water tank was fixed on a moving board with adhesive tape. In order to control and record the location for each velocity measurements, a self adhesive measuring tape was placed in both vertical and horizontal directions on the moving board. See Figure 3-6 for details of the experimental velocity measurements steps.

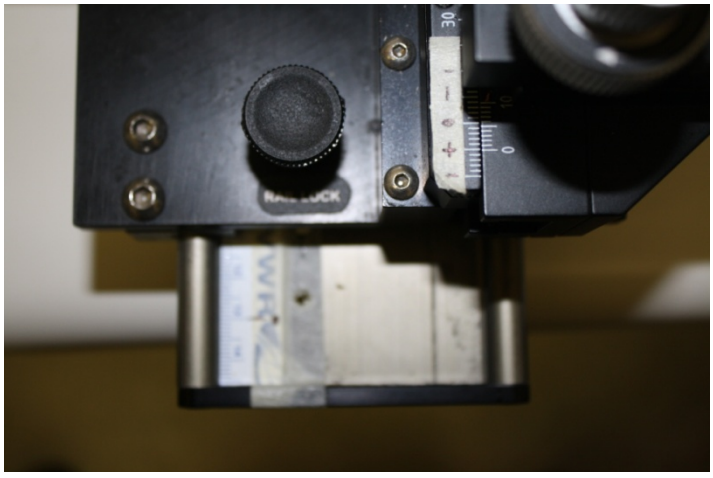

Figure 3-6: Experimental velocity measurements manual steps.

After making the data recordings at the end of the experiment, when the flow system was not in use for a short period, the working fluid remained in the flow loop. The downstream manual valve was shut and the power supply for the pulsing pump was turned off. It is important that the container is shaken to allow the particle to regain uniform position and hence help in scattering of ultrasonic waves for next experiment. If shutdown was required for longer term, the flow loop was drained, and also rinsed multiple times with clean water after every use in order to ensure that no blood-mimicking fluid is subsided into the tubes and in to the phantoms.

3.1.1.5 Experimental Velocity Measurements

Pulsed wave Doppler velocity measurements were performed on the phantom using the *Vivo770*™ high frequency ultrasound scanner system. The velocity was measured and recorded at each selected point. The phantom was divided into four paths following each vessel branch, and was also divided into 20 vertical slides with 2.5 mm of distance apart to control the locations of the selected velocity measurement positions.

The transducer of the scanner was fixed at the same position, while the phantom on the moving board was manually moved at each selected point where the velocity image was captured. To reduce the location error for each step, we followed the adhesive measuring tape mentioned earlier. An example of velocity captured from the flow system is shown in Figure 3-7. The ultrasound probe is fixed about a half centimetre above the phantom with the water path in between the probe and the phantom.

The experiments were repeated under the same conditions three times in order to obtain an average experimental flow velocity. The velocity was 42 mm/s according to the gravity elevation condition in the experimental system setup.

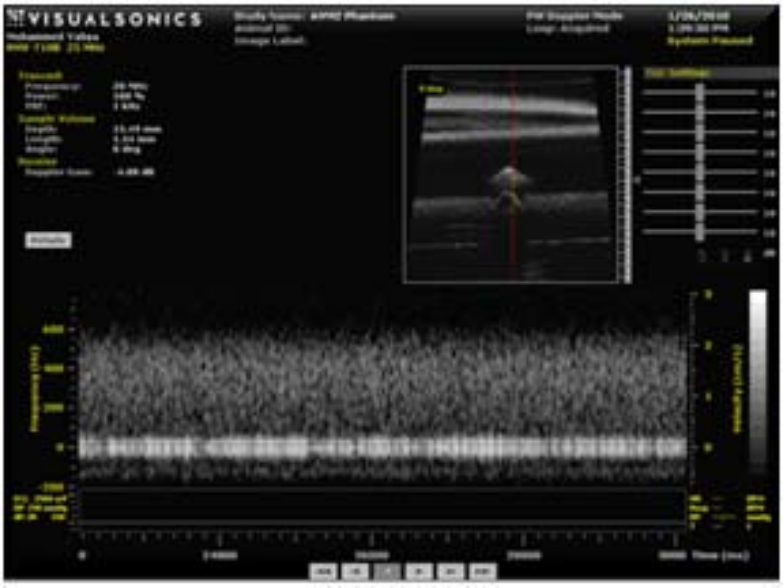

Figure 3-7: Video Display of Vevo770® scanner for the Continues Velocity on the Blood Vessel Phantom.

3.1.2 Computational Model

For model validation purpose, computational fluid dynamic based on FSI model was developed using *COMSOL Multiphysics*® finite element solver for three dimensional multichannel blood vessels. The following sections will describe briefly the details of the model development, beginning with the generation of the multichannel blood vessels geometry, followed by the governing equations and the boundary conditions, and final simulation results.

3.1.2.1 Geometry Generation

The 2D multichannel blood vessel image that was used to create the experimental phantom has been used to construct 3D multichannel blood vessel geometry. In this stage of the study, the 2D image was modified into a black and white sharp edged image using Photo Shop®, and then exported to COMSOL using a Matlab code.

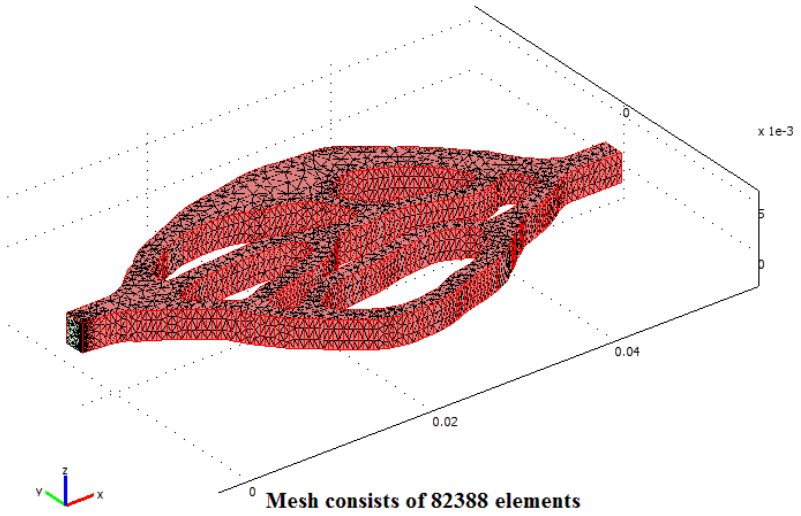

Figure 3-8: 3D Mesh of multichannel blood vessel phantom.

Then, after importing the 2D geometry into COMSL work space, the geometry was extruded for 2 mm where, COMSOL CAD tools were used to extrude the 2D geometry in COMSOL platform to 3D geometry as shown in Figure 3-8. Moreover, a fine mesh was applied to the geometry where the number of elements was 82388 elements, taking into the

consideration the calculation time of the simulation and the accuracy of the results.

3.1.2.2 Governing Equations

The principal equations for the conservation of mass and momentum for an incompressible and Newtonian fluid, in Cartesian system, which are well known as Navier-Stokes equations is written as:

$$\frac{\partial u_i}{\partial x_i} = 0 \quad for\ i,j = 1,2,3 \qquad 3-1$$

and

$$\rho . u_j \frac{\partial u_j}{\partial x_j} = \frac{\partial \sigma_{ij}}{\partial x_j} + s_i \qquad 3-2$$

where, u_i is the velocity vector, x_i = *(x, y, z)* is the Cartesian coordinate, *t* is the time, σ_{ij} is the stress tensor, where the tensors are geometric entities introduced into mathematics and physics to extend the notion of scalars, geometric vectors, and matrices to higher orders, and s_i is the momentum source component. The stress tensor is defined by the constitutive equations below:

$$\sigma_{ij} = -P\delta_{ij} + \tau_{ij} \text{ and } \tau_{ij} = 2\mu\varepsilon_{ij} \qquad 3-3$$

$$\varepsilon_{ij} = \frac{1}{2}\left(\frac{\partial u}{\partial x_j} + \frac{\partial u_j}{\partial x_i}\right) for\ i,j = 1,2,3 \qquad 3-4$$

where P is the pressure, δ_{ij} is the Kronecker delta ($\delta_{ij} = 1\ for\ i = j, otherwise = 0$), τ_{ij} are the components of the shear stress tensor, μ is the fluid viscosity, and ε_{ij} are the components of rate of deformation tensor. These flow equations together with the boundary conditions were solved using the COMSOL commercial CFD software based on the ALE method.

3.1.2.3 Boundary Conditions

The model consists of two domains, the solid domain, which represents the vessel wall, which was considered as a rigid wall where this limitation was only applied to validate the computational model. The wall was assumed as an incompressible, isotropic and linearly

elastic material, with high Young's Modulus of 80 MPa, a Poisson ratio of 0.45, and a density of 1000 Kg/m^3 with thick wall and no-slip wall condition. While, in the fluid domain, blood-mimicking fluid was modeled in isothermal conditions and as incompressible and Newtonian, in which the fluid density was $\rho = 1050\, Kg/m^3$, and viscosity was $\mu = 3.5 \times 10^{-3} m^2/s$ (Wilmer W. Nichols and Michael F. O'Rourke, 1997,1990,1998). A steady flow with laminar profile with mean velocity of 42 mm/s was selected as boundary condition at the inflow boundaries. At the outlet it was considered as free pressure boundary.

3.1.3 Model Validation Results

The velocity flow that was computed at the center-plane of the rigid walled vessel has been compared with the measured velocity values from experiment. This is shown in Figure 3-9. As mentioned earlier the blood vessel in the phantom was described as four paths as shown in Figure 3-9.

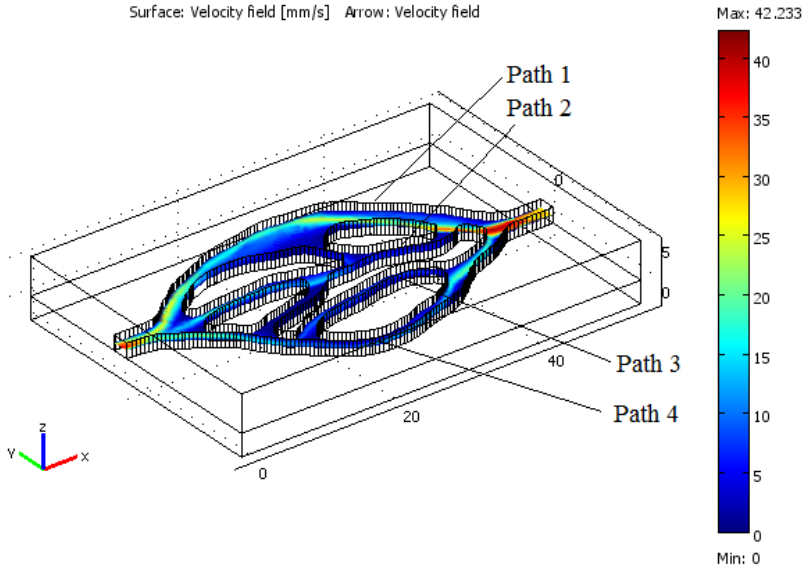

Figure 3-9: Mid-Place velocity in the rigid Rexolite® phantom.

The computed velocities from each path were plotted against the experimental one as shown in Figure 3-10. As we see, there is a close agreement between the experimental measurement results and the computed values obtained using our numerical model. The matching between the two sets of values was better at high velocities where negligible

differences were found, while difference was more significant at low velocities. This is because the Vivo770™ ultrasound scanner was found not sensitive enough at flows with average velocities less than 5 mm/s. Other possible reason for the discrepancy at low velocities could be due to the shift in the velocity measurements position experimentally on the phantom and the position on the computer simulation. Additionally, the mismatch in results could be attributed to the experimental errors which were found to be about 2.5% from the repeated experimental measurements.

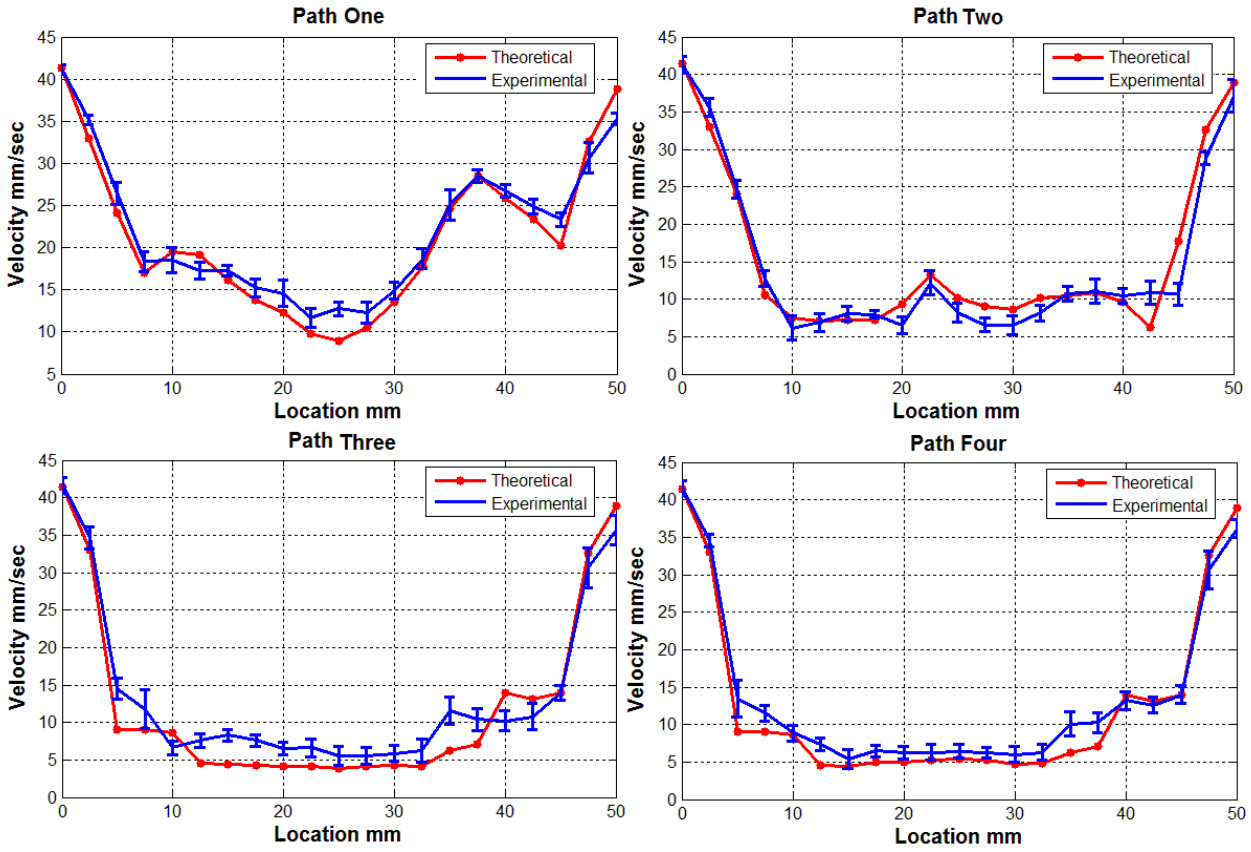

Figure 3-10: Shows the comparisons between the flow velocity from our experimental work that plotted in blue color and computed flow velocity results using FSI on the same geometry

3.2 Validation of the Numerical Model – Method Two: Comparison with Published Data

3.2.1 Experimental work

The developed numerical FSI model was also validated against the experimental data published by Mosora et al., (Mosora et al., 1993). A study on the mid-abdomen of a dog was performed *in vivo*, continuous measurement of pressure and diameter was recorded on mid-abdominal aorta whose diagram is shown in Figure 3-11. The measurements were carried out with a Gould-Statham P23 monitor (Gould Statham Inc., USA) used with a catheter tube passing through the carotid or femoral arteries till the aorta.

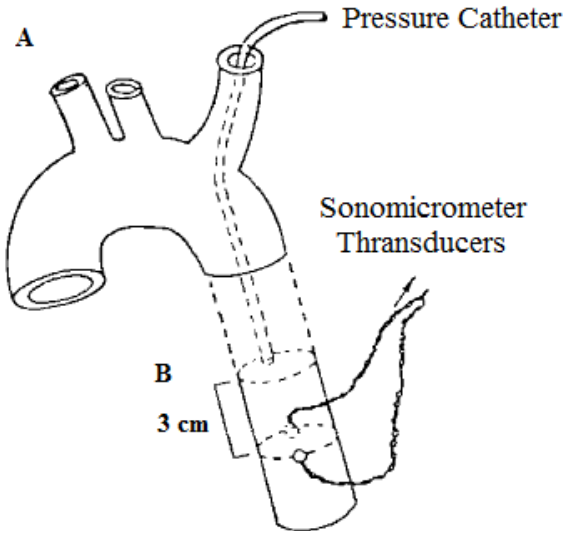

Figure 3-11: Scheme of the experimental geometry, A: on ascending thoracic aorta. B: on mid-abdominal aorta.

The diameter measurements were carried out by two techniques. First, by a pressure catheter gauge system connected with plethysmograph (Serimed PL2) that was positioned at the same level as the pressure catheter and formed by a silastic tube filled with mercury was placed around the base of thoracic ascending aorta. Second a sonomicrometer with two

transducers implanted on both sides of mid-abdominal aorta was used to measure a resonance frequency between 3 to 5 MHz. The experimental measurements were performed on a segment of aorta whose length was 3 cm. At the instant between two heart beats, when the heart is static, the mean unstressed radius and wall thickness was measured experimentally and considered as an unstressed one. While, the average radius at diastolic was 3.2 mm with wall thickness of 1 mm, the Poisson's ratio assumed to be 0.5 and Young's Modulus of 5 MPa.

3.2.1 Computational Model

The information related to geometry was provided in the experimental work (Mosora et al., 1993), and was used to manually create the same geometry in COMSOL with FSI application to model a dog's mid-abdominal aorta. In this part of the study we modeled the abdominal aorta as a hyperelastic Neo-Hookean material and used three dimensional Navier-Stokes equations to solve the fluid flow through it. The fluid was modeled to flow under the no-slip condition along the inner linings of the aorta wall. The fluid was modeled as a Newtonian fluid with viscosity $\mu = 3.5\, mPa.s$ and density $\rho = 1050\, Kg/m^3$ (Wilmer W. Nichols and Michael F. O'Rourke, 1997,1990,1998). A steady flow condition with maximum velocity of 0.30 m/s was considered at the inlet flow, while at the outflow was set to different pressure values starting from 90 mmHg, which stand for diastolic pressure and varies gradually up to 140 mmHg, which is slightly over the systolic pressure to cover whole carotid cycle.

3.2.2 Model Validation Results

The results of the wall deformation verses pressure variation due to the carotid cycle from the published data and from our numerical model was plotted as shown in Figure 3-12. The results once again show an acceptable agreement between the experimental and a computed one. However, a pronounced difference was found at high blood pressure, and that could be due to increasing experimental error at high pressures. The difference could have also been assigned to some of the assumptions that we had to make in our model that were

not mentioned in the experimental work such as considering the fluid in our model as a Newtonian one, which is an acceptable assumption in a vessel diameter larger than 1 mm (Huo et al., 2009; Wilmer W. Nichols and Michael F. O'Rourke, 1997,1990,1998). Additionally, in the experimental work there is no mention about the blood velocity in that part of aorta, and we had to adopt that value from another published data (Wilmer W. Nichols and Michael F. O'Rourke, 1997,1990,1998).

Finally, we can conclude after those two experimental validations that our numerical model gives accurate results in both rigid and an elastic wall conditions in typical clinical applications.

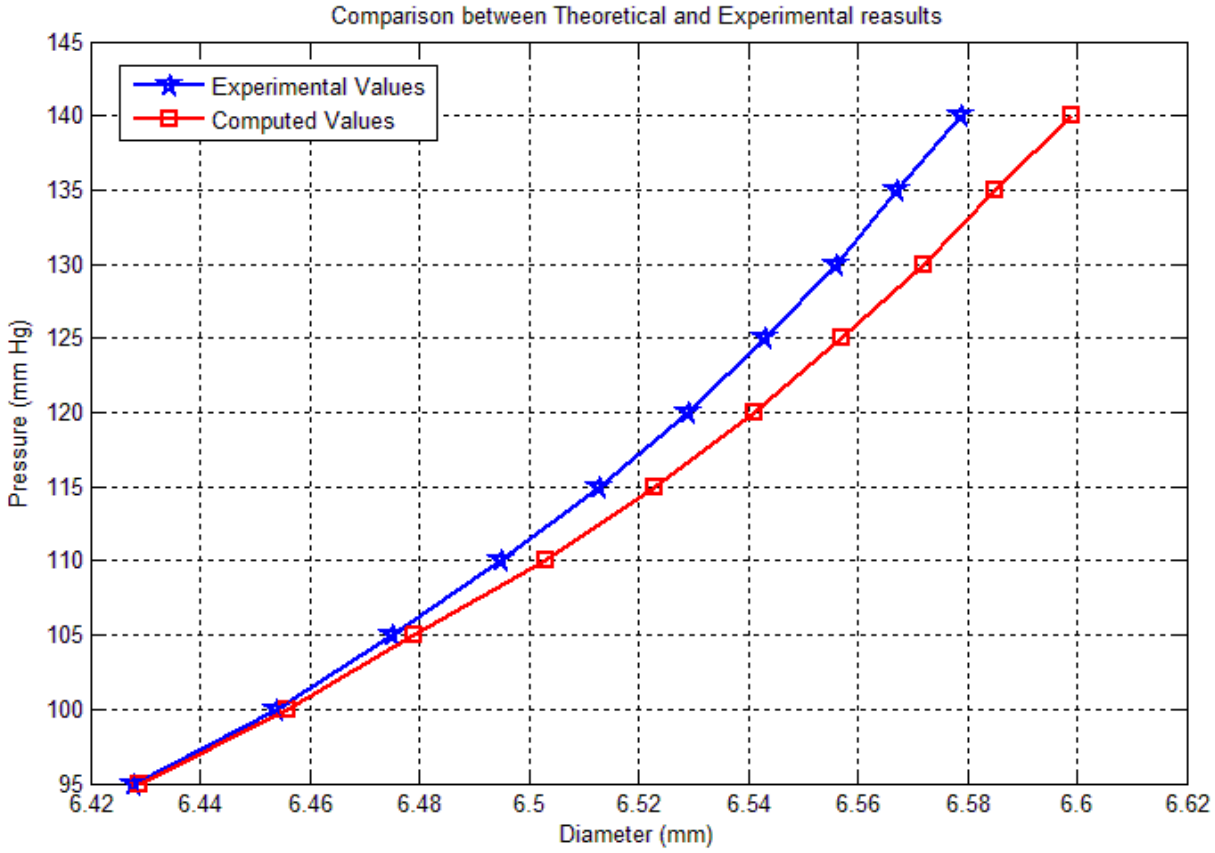

Figure 3-12: Comparison result of experimental and simulated values of pressure as a function of vessel diameter.

Chapter 4 RESULTS AND DISCUSSION

In this study, three dimensional idealized elastic wall geometries were replicated and analysed using hyperelastic neo-Hookean nonlinear isotropic materials (Kyriacou & Humphrey, 1996) as a two way-coupling of the FSI model based on the ALE algorithm, in the presence of saccular aneurysms (Takizawa et al., 2010). In this respect, aneurysm was introduced as a smooth ellipsoidal surface in a healthy artery with different wall mechanical properties.

Parabolic steady laminar flow simulations were performed with an unvarying average inlet velocity of $50\ \mathrm{mm/s}$ applied on all geometries, whereas, the outflow pressure varied from $40\ to\ 200\ mmHg$. The resultant analyses disclosed the impact of the geometry size and shape and material properties on aneurysms' initiation and growth. The model was applied on three idealized geometries for a healthy subject: first with the absence of aneurysms and then the same geometries were used with the presence of the aneurysms. This was done to examine the influence of the wall mechanical properties in addition to the effect of arterial geometry and aneurysm neck size on the hemodynamics of the aneurysm, and to associate these parameters with the growth and rupture of the aneurysm.

4.1 Influence of Wall Mechanical Properties on Aneurysms Initiation and Growth

4.1.1 Wall Deformations

We calculated the resulting wall deformation using a finite-element solver (COMSOL Multiphysics) based on the FSI model. The FSI computation formed strong implicit coupling between the solid phase stress-strain computation and the fluid phase computation. Subsequently, pressure and shear stress information was sent to the stress computation

module for the calculation of the deformations and stresses. Thus, these deformations are transported back to the fluid module, where a new grid is created and the solution is recalculated on the new deformed geometry. Iterations are performed continuously till the time convergence is obtained. According to the finite element-method, this process is applied on each element at the node.

Figures 4-1 to 4-3 below show that the evolutions of the aneurismal shape are caused only due to the dynamic alteration of the Young's elasticity modulus for the three models having large aneurysm neck surface area S_l, while Figures 4-4 to 4-6 show the same simulations but with small aneurysm neck surface area S_s (neck size). The geometrical evolution was performed in four quasi-steady steps. The Young's Modulus (E) for the surfaces S_l, S_s, changed within a range from $0.25\ to\ 0.0625\ Mpa$. The above arterial wall remodelling steps were captured under one constant pressure of $60\ mmHg$ as shown in Figures 4-1 to 4-6. These figures reflect the four consecutive steps of wall weakening process, demonstrated an interesting behaviour of arterial remodelling. The aneurysm growth process shows in these figures reflects the function of endothelial cell layer function as a sensor of arterial remodelling on developing aneurysms (Kinlay et al., 2001; Resnick et al., 2003). This also comes in conformity with the computationally simulated results.

On the other hand, it is evident that the resulting arterial geometry at lower Young's Modulus of $\mathrm{E} = 0.0625\ MPa$ is considerably more prone to deformation than the same geometry with higher Young's Modulus $of\ \mathrm{E} = 0.1875\ MPa$. In other words, the arterial geometry achieved by lower E has more deformation on the aneurysm part in all models. Under the consideration of $\mathrm{E} = 0.125\ MPa$, the maximum displacement in walls was $149.8, 934.5, \text{and } 953.4\ \mu m$ and $109.9, 635.6, \text{and } 344.38\ \mu m$ for the large and the small neck size of the models 1 to 3, respectively, where the maximum wall deformation occurring in the fundus of the aneurysms. Hence the middle of aneurysmal wall is the region that shows much of the deformation, and fairly large displacements can be seen on the fundus of the aneurysm, which is of the order of one tenth of the arterial diameter which is approximately $3\ mm$.

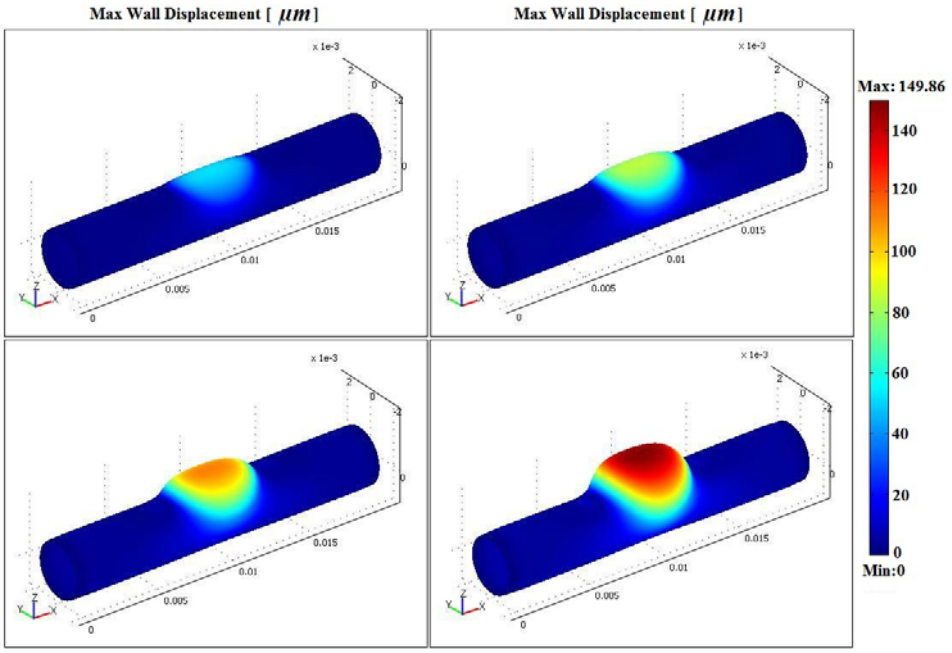

Figure 4-1: Wall Deformation in μm for aneurysm geometrical evolution due to the Young`s Modulus of elasticity dynamic alteration large aneurysm neck surface area in 3D view.

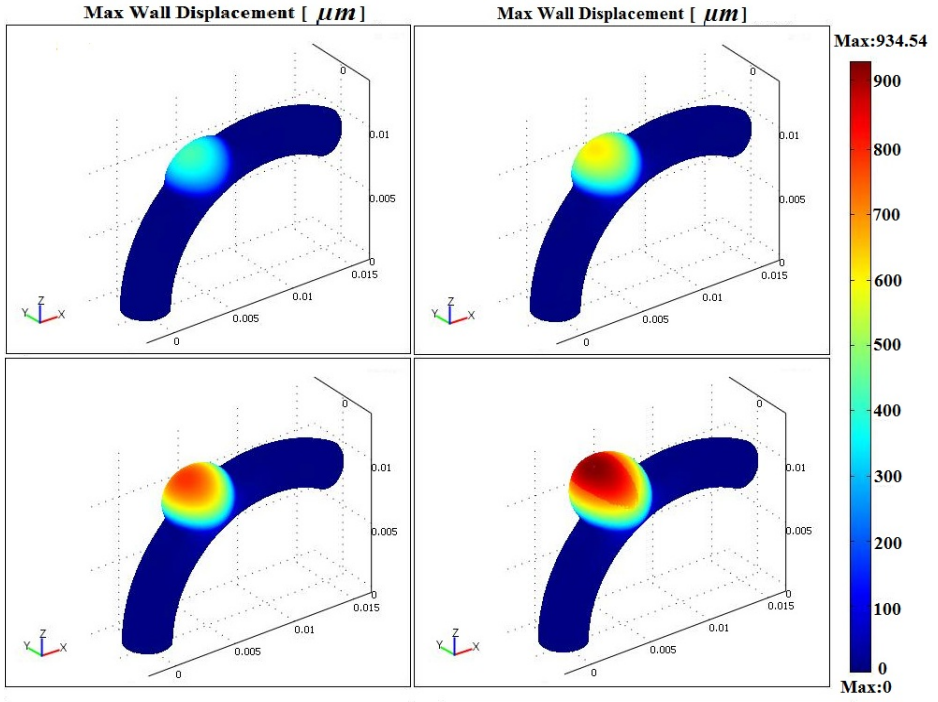

Figure 4-2: Wall Deformation in μm for aneurysm geometrical evolution due to the Young`s Modulus of elasticity dynamic alteration large aneurysm neck surface area in 3D view.

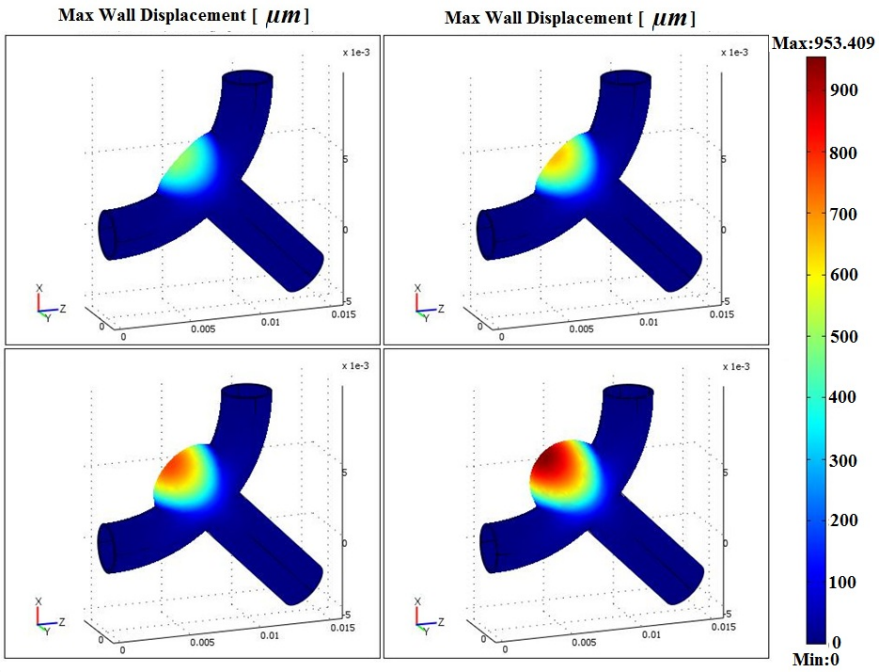

Figure 4-3: Wall Deformation in µm for aneurysm geometrical evolution due to the Young`s Modulus of elasticity dynamic alteration large aneurysm neck surface area in 3D view.

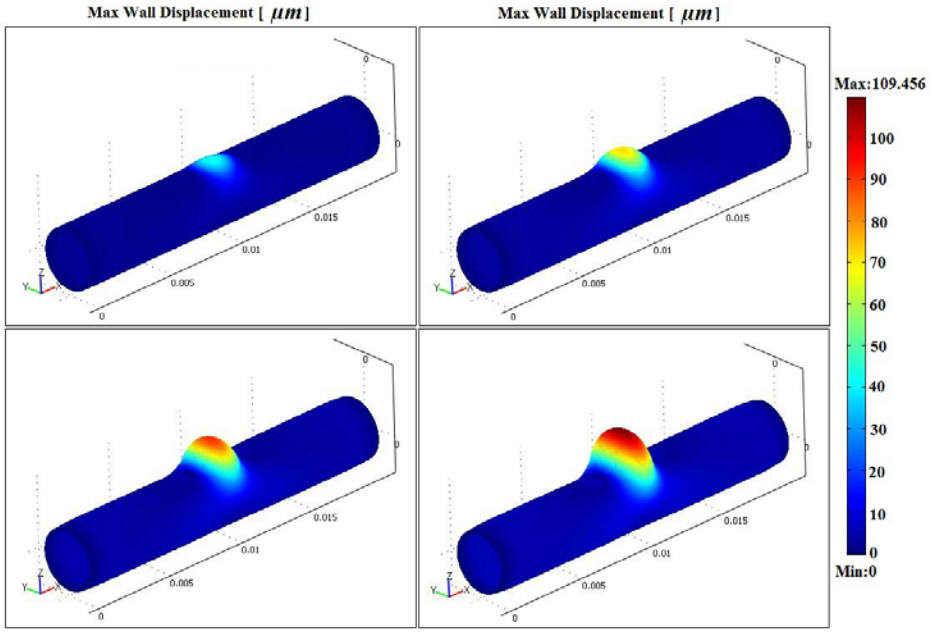

Figure 4-4: Wall Deformation in µm for aneurysm geometrical evolution due to the Young`s Modulus of elasticity dynamic alteration small aneurysm neck surface area in 3D view.

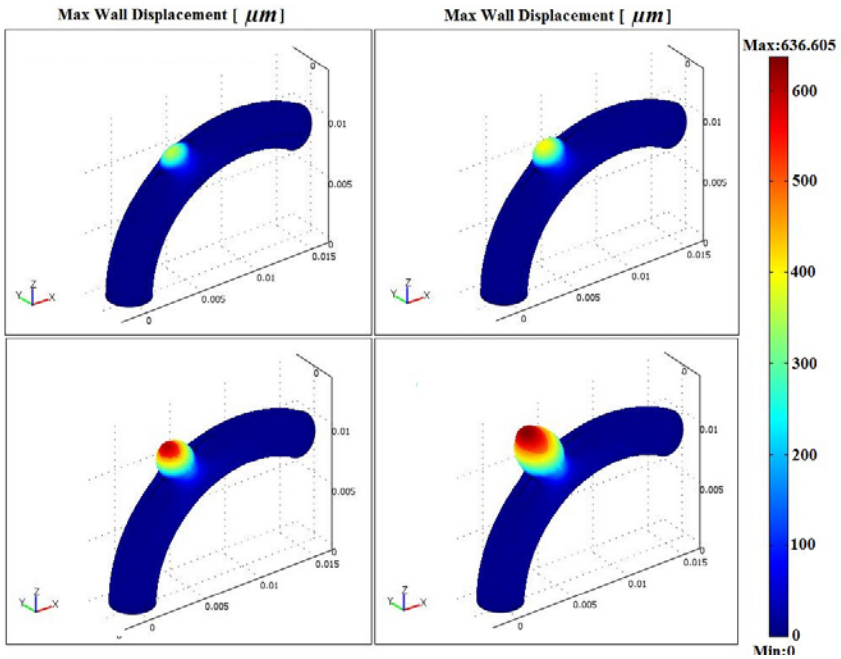

Figure 4-5: Wall Deformation in µm for aneurysm geometrical evolution due to the Young`s Modulus of elasticity dynamic alteration small aneurysm neck surface area in 3D view.

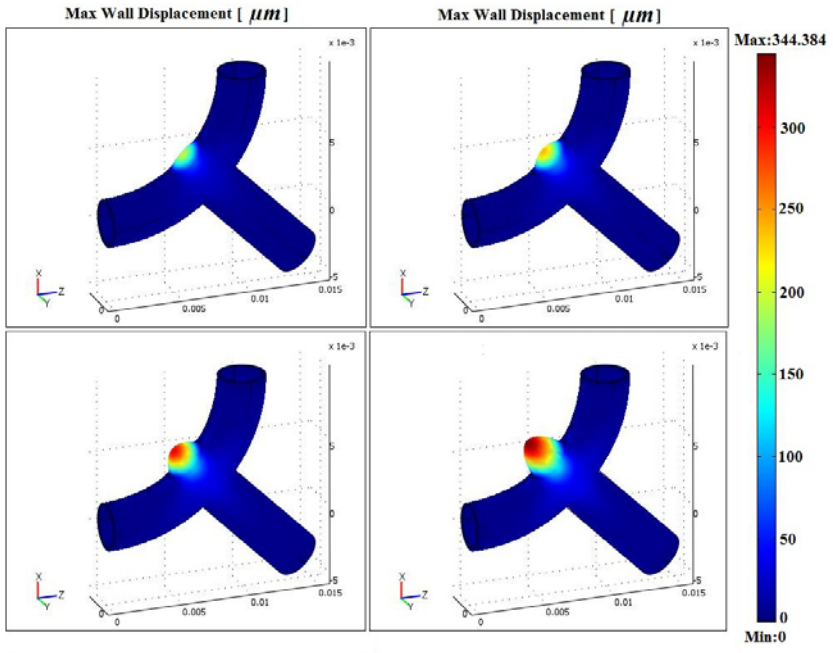

Figure 4-6: Wall Deformation in µm for aneurysm geometrical evolution due to the Young`s Modulus of elasticity dynamic alteration small aneurysm neck surface area in 3D view.

The influence of variations in the Young's Modulus for model 2 and model 3 has been plotted in Figures 4-7 and 4-8 for both large surface area S_l and small surface area S_S respectively.

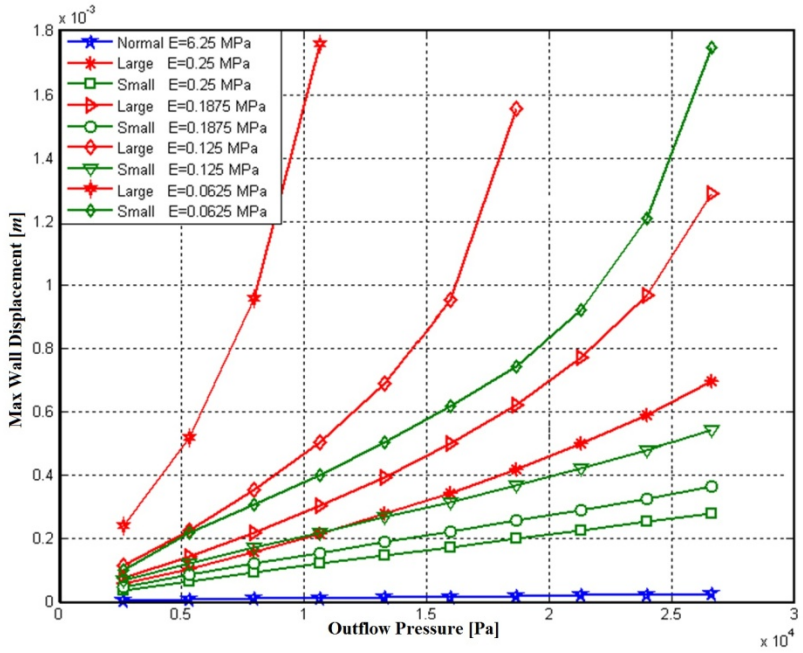

Figure 4-7: Maximum wall displacements for models 2 as a function of outflow pressure.

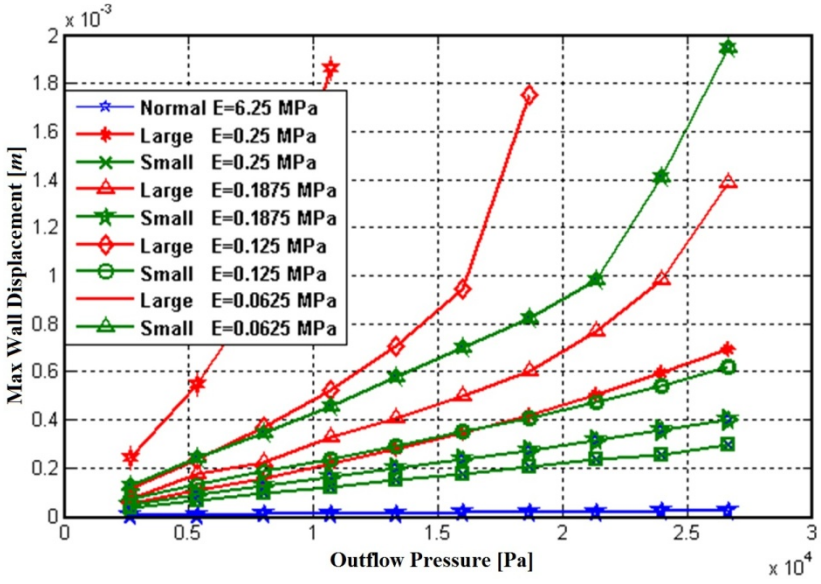

Figure 4-8: Maximum wall displacements for models 3 as a function of outflow pressure.

The plotting shows that reduction in the Young's Modulus has significant effect on aneurysm formation and growth as observed in a comparison of healthy models versus wide range of blood pressures. The wall displacement of arteries at high pressure for the curved and bifurcation model have not been shown in Figures 4-7 and 4-8, since the material failed, which the artery lose is strength under the action of high pressure and low E.

The predicted aneurysmal wall rupture can be seen from Figure 4-9. The results for the curved model 2 were calculated based on the Laplace law. There occurs an intersection of the Laplace law result and the computed radii result based on our model. Based on the simulations, we stipulate that if the aneurism's critical radius falls above the Laplace curve, it has high probability of rupture. High risk of aneurism rupture translates to an urgent need for a suitable treatment.

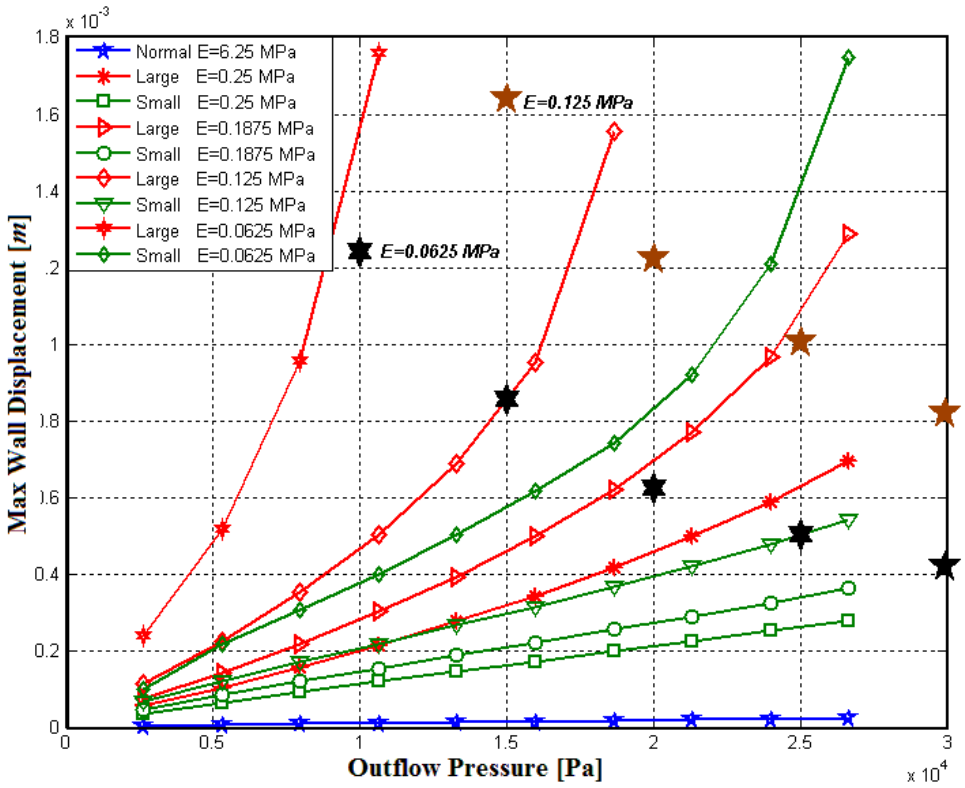

Figure 4-9: Predicted aneurysmal wall rupture for the curved model 2 was calculated based on the Laplace law.

4.1.2 Wall Shear Stress and Flow Field

For the aneurysm progression, one of the most relevant hemodynamic parameters is the WSS. WSS is the tangential force of the blood flow on the endothelial surface of the blood vessel. In this study it has been assumed that the blood flows at constant velocity of 50 mm/s with a fixed inflow pressure of $20\,mm/Hg$ and variable pressures of $40-200\,mm/Hg$ at the outlet boundary.

The arterial wall stress tensor consists of nine components, rendering it very difficult to present any illustrative results based on it. In order to meet this challenge alternatively, the energetic equivalent formulation as presented by von Mises is used to illustrate the stress behaviour of the arterial wall during its deformation period. The equivalent von Mises stress depicts the distortional energy (δ^2/E) contained by an element and in terms of all the positive defined scalar stress values, gives a final stress value.

Figures 4-10 and 4-15 show the patterns of WSS variations at different instants during the aneurysmal growth for the models 1 to 3 for four different blood pressures 40, 80, 120, and 160 mmHg respectively at fixed arterial wall elasticity of $E = 0.125\,MPa$. The simulated results not only bring agreement with literature (Hashimoto,T. 2006; Kroon,M. 2007), but also justify the observation that the shear stress gives higher values at the neck distal side of aneurysm which is away from the fundus. It also becomes evident by the results that the major part of the deformation is caused by this remodelling procedure and essentially a high WSS caused at aneurysm part is responsible for the shaping of the aneurysm. Figures 4-10 and 4-15 help us in drawing the conclusion that the resultant spatial stresses from this deformation are similar to that during the inflation of a balloon.

It has been observed that large deformation takes place near the apex of this ‘‘balloon’’. Due to this, the largest stress values are found at the distal aneurysmal wall region with the higher E value. The results of S_l, S_s for the models 1 to 3 are presented in Figures 4-10 to 4-15, respectively.

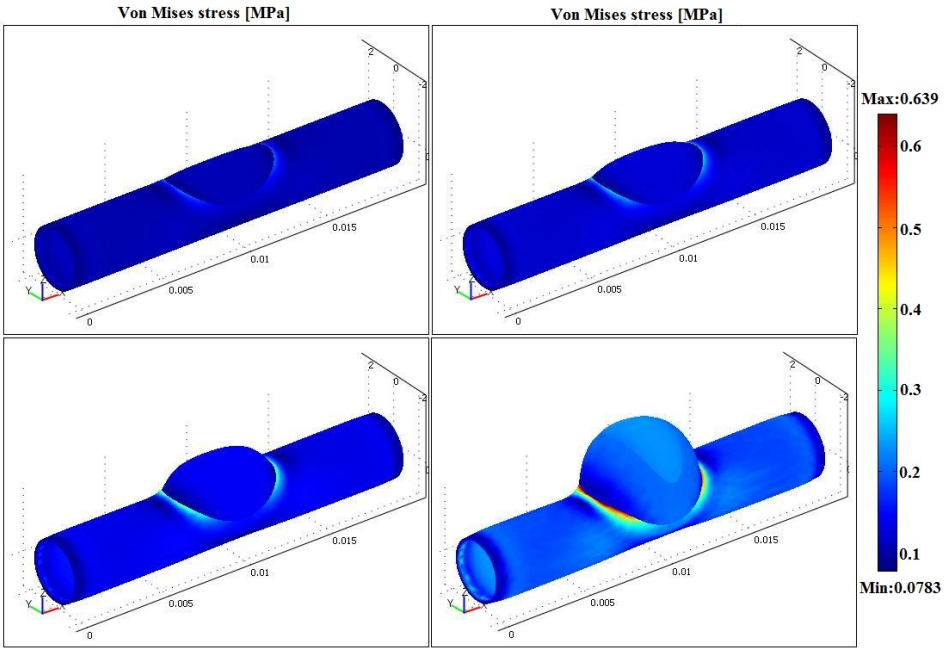

Figure 4-10: Von Mises wall shear stress in Pa for aneurysm geometrical at four different blood pressures 40, 80, 120, and 160 *mmHg at E=0.125 MPa* on large aneurysm neck surface area.

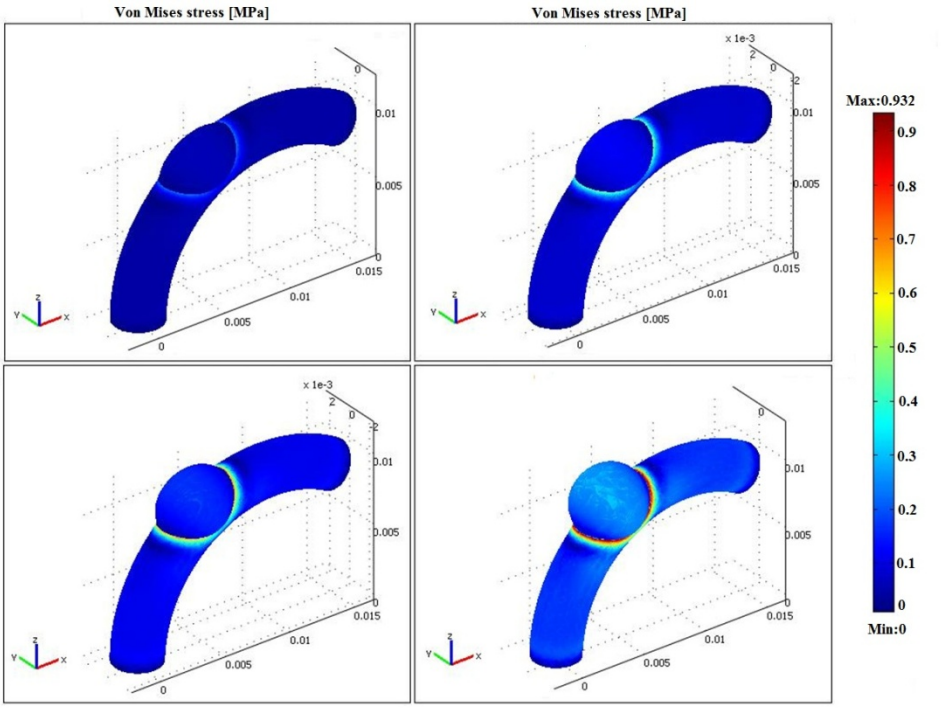

Figure 4-11: Von Mises wall shear stress in Pa for aneurysm geometrical at four different blood pressures 40, 80, 120, and 160 *mmHg at E=0.125 MPa* on large aneurysm neck surface area.

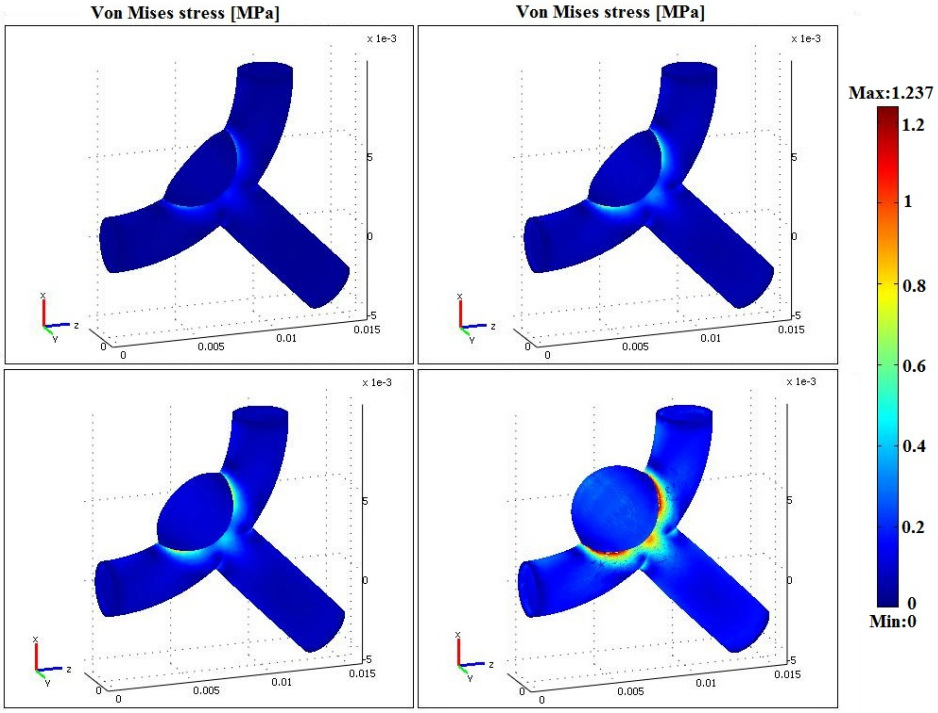

Figure 4-12: Von Mises wall shear stress in Pa for aneurysm geometrical at four different blood pressures 40, 80, 120, and 160 *mmHg at E=0.125 MPa* on large aneurysm neck surface area.

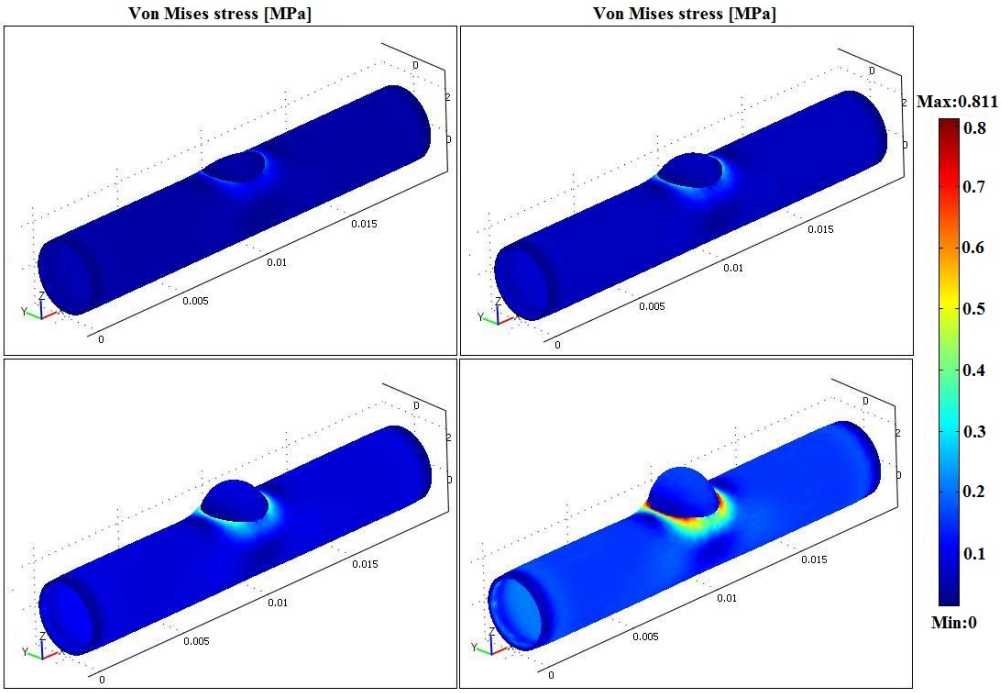

Figure 4-13: Von Mises wall shear stress in Pa for aneurysm geometrical at four different blood pressures 40, 80, 120, and 160 *mmHg at E=0.125 MPa* on small aneurysm neck surface area.

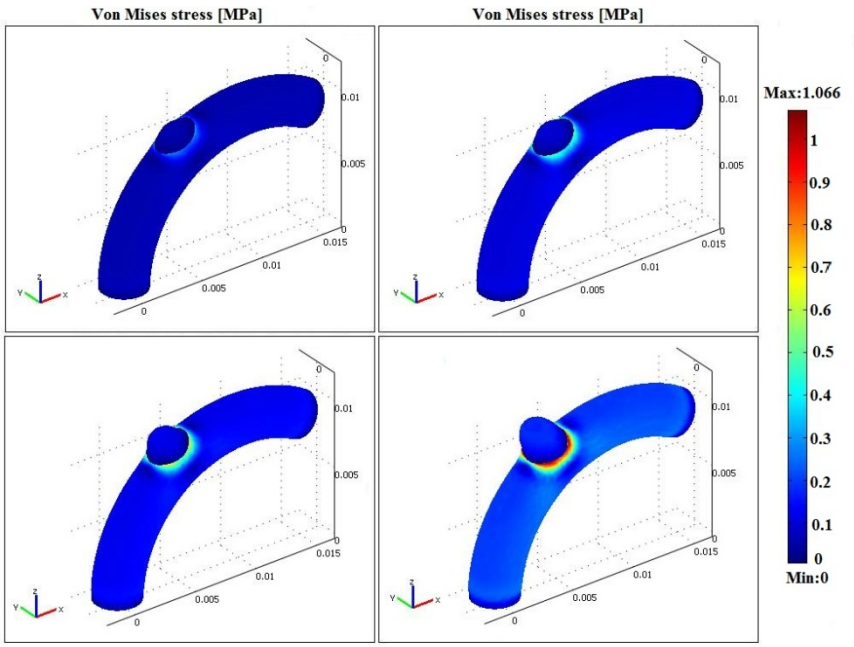

Figure 4-14: Von Mises wall shear stress in Pa for aneurysm geometrical at four different blood pressures 40, 80, 120, and 160 *mmHg at E=0.125 MPa* on small aneurysm neck surface area

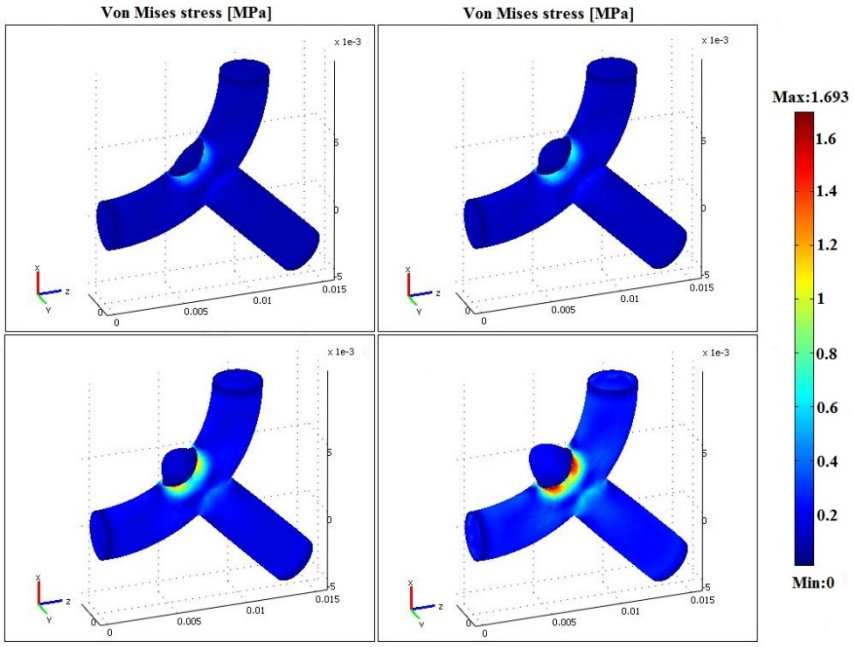

Figure 4-15: Von Mises wall shear stress in Pa for aneurysm geometrical at four different blood pressures 40, 80, 120, and 160 *mmHg at E=0.125 MPa* on large aneurysm neck surface area.

4.2 Effects of Blood Vessel Geometry on Cerebral Aneurysm Initiation and Growth

The second important process carried out in this study, that affects the aneurysm growth, was to quantify the relationship between hemodynamic forces and arterial curvature in order to determine further correlations of the effect of arterial geometry on the aneurysm growth.

In this context, the aneurysm growth on three idealized models was analysed with varying arterial curvatures, along with two aneurysm neck sizes to quantify the role of local hemodynamic forces within the aneurysm. Idealized arterial geometries with varying curvatures (and keeping other parameters unchanged at the same time) were adopted to segregate the arterial geometry and aneurysm neck size from several other geometric and physiological factors present in human aneurysms.

4.2.1 Flow Dynamic and Velocity Field

Figures 4-16 to 4-20 shows how the computed results of the flow dynamics, represented by the velocity field and streamlines, were captured at the center-plane in all three geometries. During this procedure, we selected outflow blood pressure of $120\ mmHg$ from various outflow pressures under use and the E of $0.125\ MPa$ in all the figures presented in this study. After the development of the aneurysm, it was observed that some of the flow streamlines never entered the aneurysm, whereas all the paths entering the aneurysm did so near the distal side of the neck in all three models. Some streamlines entering the aneurysm left at the proximal side of the neck with a lower velocity, whereas others joined the inflow of the parent artery, entered the cavity again, spinning erratically within the aneurysm. In the case of the straight artery, the vortices at the distal side of the neck weakly allowed the flow into the aneurysm, as compared to the arteries with more pronounced curvature.

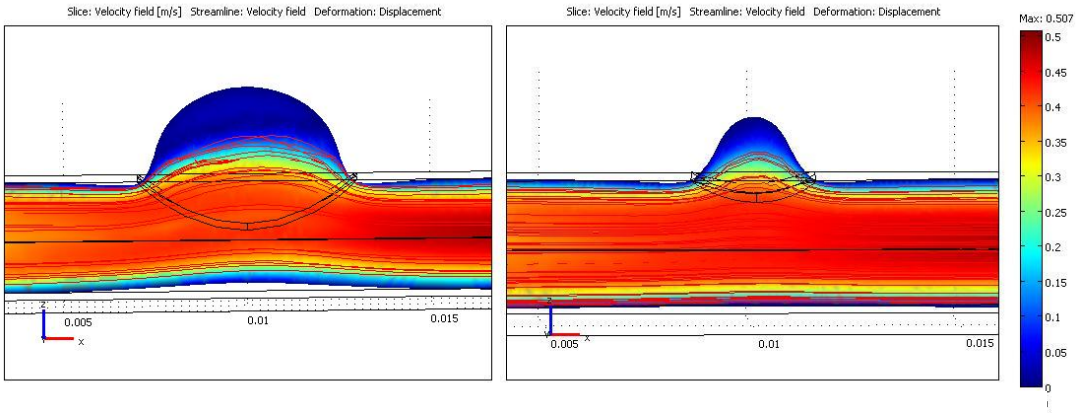

Figure 4-16: Velocity field and stream lines at the aneurysm plane in the straight artery model 1with two neck surface area.

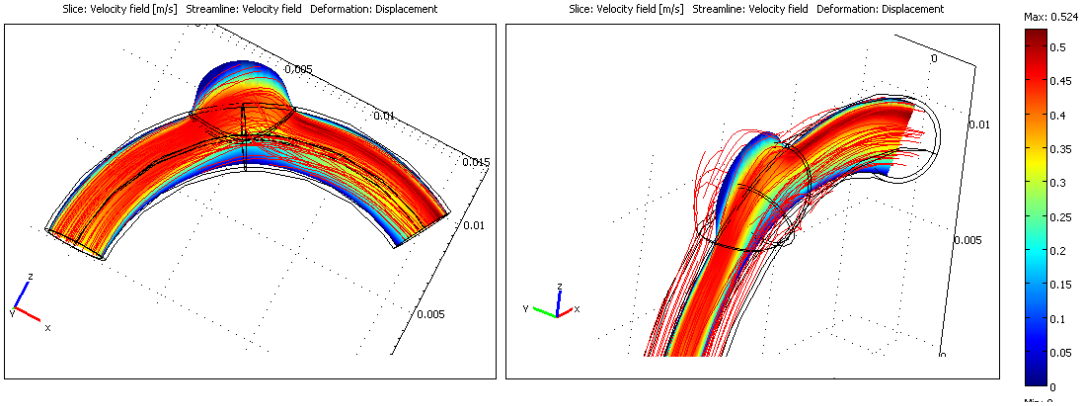

Figure 4-17: Velocity field and stream lines at the aneurysm plane in curvature artery model 2 for the large neck surface area.

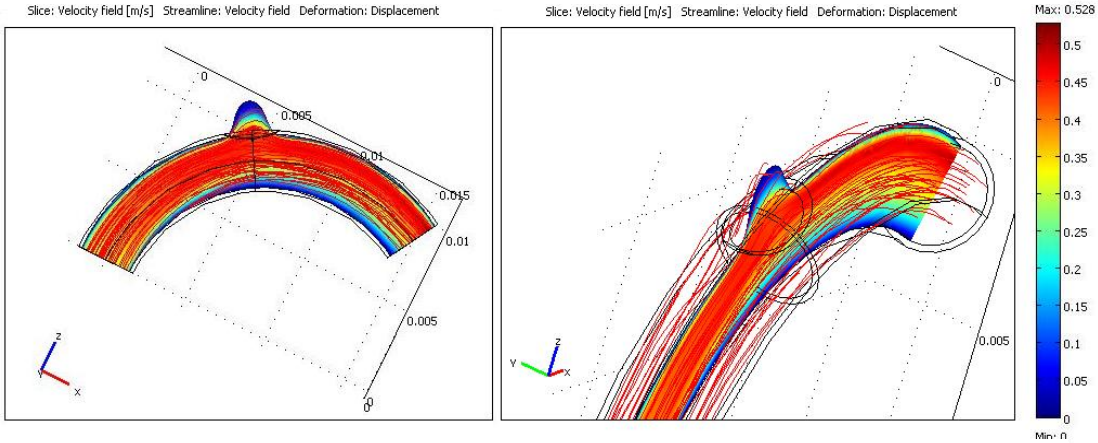

Figure 4-18: Velocity field and stream lines at the aneurysm plane in curvature artery model 2 for the small neck surface area.

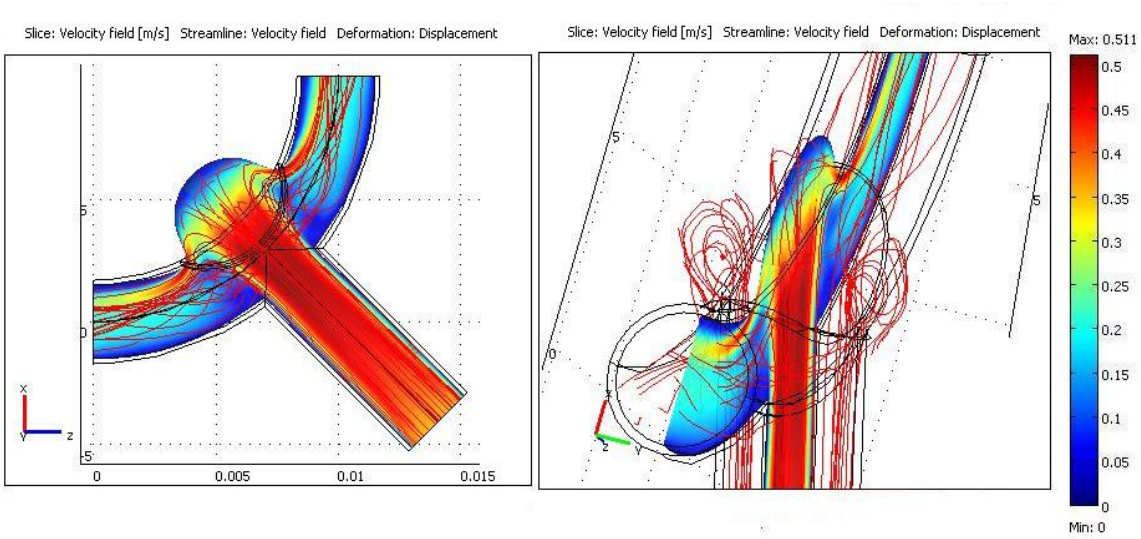

Figure 4-19: Velocity field and stream lines at the aneurysm plane in arterial bifurcation model 3 for the large neck surface area.

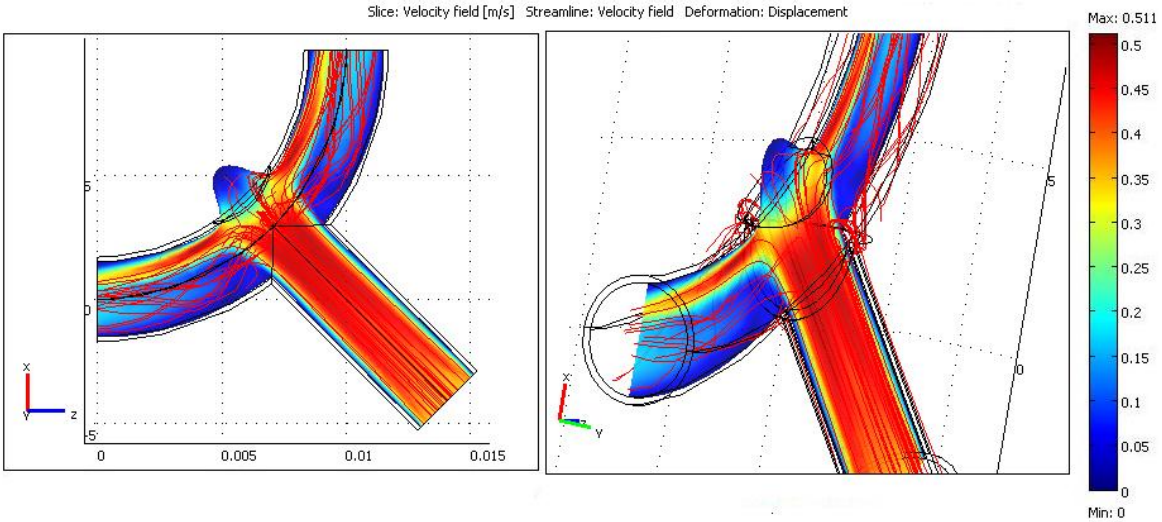

Figure 4-20: Velocity field and stream lines at the aneurysm plane in arterial bifurcation model 3 for the small neck surface area.

It is interesting to know that blood impinges on the distal aneurysm neck while travelling through the main lumen of the artery. Subsequently, the impinged flow is diverted into the aneurysm sac present at the side of the distal neck. The blood re-circulates within the aneurysm and travels in a retrograde fashion to the main flow in the arterial lumen. Despite

the fact that the magnitude of the intra-aneurysmal flow velocities is smaller, the blood continues to re-circulate inside the aneurysm until it joins the mainstream flow and is carried downstream.

As far as velocity field is concerned, high velocity flow is observed at the distal side of aneurysm neck with increasing curvature. Figures 4-16 to 4-20 illustrate the flow velocity at the centerline of the model, which was documented at the selected outflow pressure of $120\ mmHg$ and E of $0.125\ MPa$ in the three models. Model 1 depicted a straight artery, where the curvature in model was insignificant, thus the flow was weakly entrained into the aneurysm by the streamlines at the distal side of the aneurysmal neck. In the case of the curved models 2 and 3, the arteries having more curvatures, allow the velocity profiles to tilt towards the outer wall of the lesion, demonstrating the effect of centrifugal force in all models as illustrated in previous figures. From these results, it is observed that a large volume of higher momentum flow impinges more strongly on the distal of the aneurysm neck as the degree of arterial curvature or the major axis of the aneurysm neck increases. The high momentum flow resulted in the formation of a strong vortex in the aneurysm cavity. Therefore it was concluded that the affected area enlarges with the increase in arterial curvature and in the size of the aneurysm neck.

4.2.2 Wall Shear Stress

As a result of the increase in the degree of arterial curvature and decreasing the size of the aneurysm neck, a rise in the wall deformation at the fundus of the aneurysmal wall along with a rise in the WSS at the distal side of the neck were observed in all models, as can be seen in previous Figures. These increases can be considered as a function of arterial curvature or aneurysm neck size or both. To quantify this relationship, we plot the wall deformation and the WSS for three different geometries with two sizes of the aneurysm neck as a function of pressure as shown in Figures 4-21 and 4-22 respectively.

A comparison with the parent artery shows low WSS within the dome of the aneurysm through visualizing the distribution of WSS magnitude. In all simulations, high WSS is always found at the distal side of aneurysmal wall. Furthermore, the intra-aneurysmal

flows, as established by the streamlines in Figures 4-21 and 4-22 were smoother with a more simplified vortical pattern. In cases of high degrees of upstream curvature, these changes are more prominent (i.e. models 2 and 3).

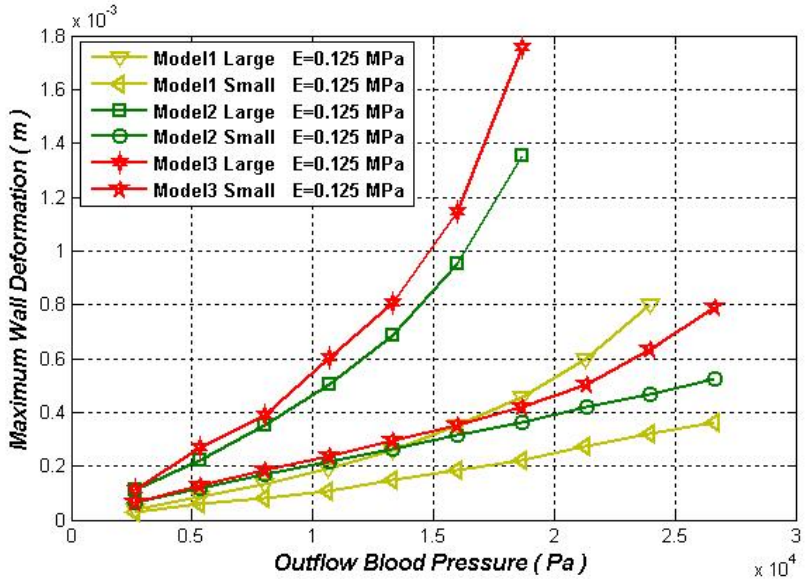

Figure 4-21: Comparative plot of the maximum wall deformation at the aneurysm for the three models as a function of outflow pressure.

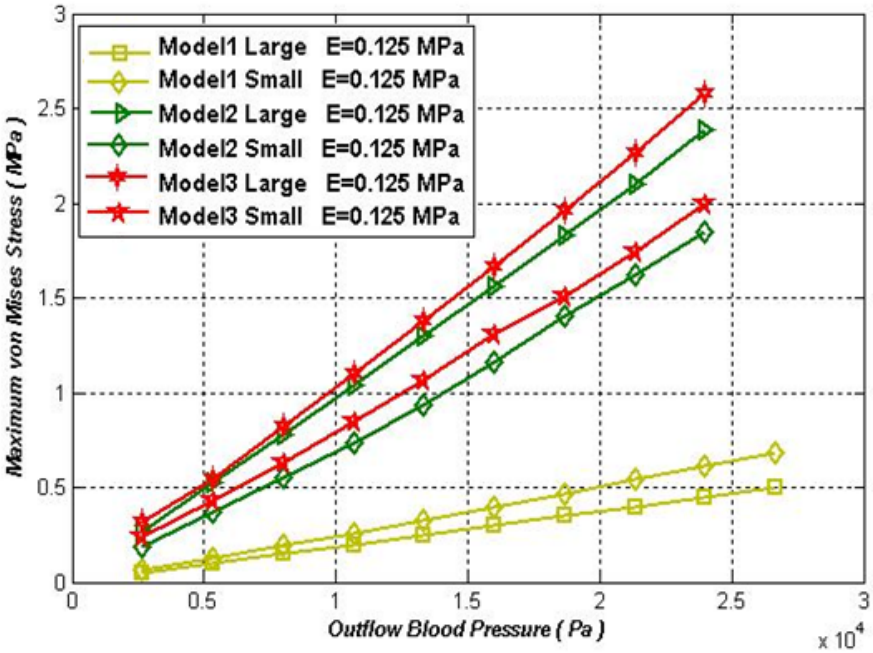

Figure 4-22: Comparative plot of the wall shear stress at the distal side of aneurysmal wall for the three models as a function of outflow pressure.

4.3 Discussion

The first major part of this study investigated the influence of the reduction in the E factor of an aneurysmal wall on the initiation and growth of aneurysm in three idealized models. This factor is of special interest since it is the only main factor that will be changed in case of any sudden arterial wall injury or disease, therefore aneurysms most commonly occur at these locations.

Simulations were repeated for four values of E assigned to the aneurysm part of the arterial wall with a wider-range of blood pressures, covering the normal and abnormal (hypertension) blood pressures in human cardiac cycle. In such cases, as the aneurysm dome growth proceeds, the wall-aneurysmal diameter begins to increase and the arterial remodelling itself to compensator mechanism tensor to reduce the risk of aneurysmal wall stress and rupture. In the beginning, steady flow in healthy arteries without an aneurysm was simulated. The results indicated that besides an insignificant wall displacement at the aneurysmal wall, no shear stress is likely to occur. A wide-range of normal and high blood pressures were used in this respect.

In all the three models studied, the wall E was modified at selected areas on the arterial wall in order to account for the presence of an aneurysm. The simulation result indicates that the aneurysm develops at that part of the wall which has less mechanical properties, and the developed aneurysm size rapidly increases with an increase of blood pressure and a decrease in their E. The simulation also specifies that increasing the aneurysmal surface area from small S_s to large S_l (neck size) leads to large amount of wall deformation and eventually to high probability of rupture. In addition, we also observed that the maximum wall displacement occurred at the fundus of the aneurysmal wall, increases the possibility of rupture at the fundus of an aneurysm. On the other hand, smaller size of aneurysm neck S_s showed higher shear rates than the larger size of aneurysm neck S_l, possibly due to the reason that at a given blood flow the amount of shear stress is concentrated on smaller area of aneurysm neck, while it is distributed liberally on larger area of aneurysm neck, and the high shear stress occurs at the distal side of the aneurysmal wall.

It has been inferred from the computational simulation results for the wall deformation and WSS that large wall deformation does not occur at the point of high wall stress. Actually, the maximum WSS occurs at the distal side of the artery which is away from the aneurysm fundus, while the maximum wall deformation occurs at the fundus of the aneurysmal wall. This inference is also in agreement with the published studies (Torii et al., 2006; Torii, Oshima, Kobayashi, Takagi, & Tezduyar, 2007b; Torii, Oshima, Kobayashi, Takagi, & Tezduyar, 2009). We also found that the WSS is not distributed uniformly on the aneurysmal wall and is mostly found with high values at the distal wall in the direction of blood flow.

The maximum value of WSS on the aneurysm is generally found around the region where the flow first comes in contact with the aneurysm wall, e.g., the distal side of aneurysms neck. This was found to be about 2-10 times the values in the parent artery, whereas the value of the spatially averaged WSS over the entire aneurysm is usually less than the parent artery values. It is to be noted that WSS over the aneurysm mostly relies on the aneurysm neck size and increases linearly with a decrease in the Young's module. This linear increase is only observed at low blood pressure, while at high blood pressure it is more nonlinear as shown in Figures 4-21 and 4-22. An increased WSS within distal side of aneurysm neck as compared to the parent artery is believed to be a contributing factor for aneurysm growth or rupture.

The observations made in this study are significant from the modeling point of view, as well as for the contribution it has made for understanding the processes of aneurysm growth and rupture. Currently, there are two opposing schools of thought about these processes. On one hand it is believed, according to the claim made by low-flow theories, that the dome of aneurysms under low WSS states triggers mechanobiologic processes that weaken the arterial wall, which in turn results in the growth or rupture of the aneurysm (Griffith, 1994; Liepsch, 1986). These theories are formulated on the basis of the observations of low WSS in the aneurysm dome conducted on idealized experimental and computational models and clinical observations.

On the other hand, high-flow theories argue that unusually large WSS at the aneurysm wall, especially at the flow impaction area cause a different set of mechanobiologic processes that weaken the vessel structure and result in growth or rupture (Fukuda et al., 2000; Fukuda et al., 2000; Guzman, Abe, & Zarins, 1997; Kyriacou & Humphrey, 1996).

The current study signifies that the hemodynamic patterns demonstrate regions of increased WSS at the aneurysm distal through modeling of idealized aneurysm geometries. Although the extent of these differences is not identified, drawing general conclusions from idealized models may be deceptive. Aneurysm rupture mechanism theories should take possible errors into deliberation. There is also a need for re-scrutinizing in the low flow theories depending on previous "low WSS states". Furthermore, it is imperative to distinguish between the mechanisms that are actually driving the processes of growth and rupture using hemodynamic studies employing "realistic" (i.e., including the correct geometry of the proximal segment of the parent vessel) patient specific vascular models.

Despite the fact that we have found changes in intra-aneurysmal flow patterns and WSS in our study, yet there are limitations to our study that may influence our results. The CFD analysis relies on a number of assumption including Newtonian flow as shows significant effect at small diameter < 1mm, input flow, outflow conditions where pulsatile flow is more realistic flow, and fixed aneurysmal wall thickness as is reported to be thinner than the rest of the artery.

The concentration of high hemodynamic stresses at the aneurysm neck suggests an inclination for the increase of the size of the aneurysm neck. The maximal pressure in the surrounding area of the narrow-neck S_s aneurysm configuration is up to 5 times greater than that of the luminal pressure in the parent artery. On the other hand, the computational results for a wide-neck S_l saccular aneurysm reflect the existence of high pressure at the aneurysm neck. As compared to the narrow-neck aneurysm model, the amount of intra-aneurysmal flow is dramatically increased in the wide-neck S_l saccular aneurysm, therefore supporting the proposition that wide-neck aneurysms are less vulnerable to thrombus formation.

Towards the second part of the study, the focus was aimed at the effect of arterial geometry on aneurysm growth. We came to know that in the case of the curved arterial segment model,

high streamline flow arises at the apex of the bend along the outer (lateral) arterial wall, whereas in case of bifurcation, high streamline flow exists at the apex of the bifurcation.

An investigation conducted on the progressive formation of saccular aneurysms in curved non-bifurcating arteries exposed several assumed but unproved hypotheses concerning mechanisms that play a significant role in the origin of aneurysms. It also revealed that local pressure increase is present along the lateral (outer) wall in the region of the bend. This localized high pressure zone yields high hemodynamic stress as a result that materializes the occurrence of saccular aneurysms on the lateral wall of the curved arteries. We found that once the yield stress, which is defined as the stress at which a predetermined amount of permanent deformation occurs, of the arterial wall is exceeded, the wall undertakes plastic deformation and therefore an aneurysm bleb develops. It was observed that when a small aneurysm grows, the blood impinges on the wall throughout the entire pressure values (outflow boundary), thus making the distal neck a crucial target of hemodynamic stress. As a result of high pressures and shear rates at the distal neck within the aneurysm bleb, dilatation occurs at this site, further resulting in a fully developed saccular aneurysm that inclines towards the downstream direction. Thus, the foremost changes in hemodynamics as well as aneurysm growth occur at the dome of aneurysms, as originally suspected. These results show that as the distal neck site is pushed downstream, the aneurysm mouth is prone to get enlarged.

The risk of the rupture of ICA is generally assumed to be associated with maximum diameter. Where, size is the primary parameter currently used to determine whether an aneurysm is likely to rupture or not, numerous studies categorised aneurysms into smaller and larger sizes (Morita, Fujiwara, Hashi, Ohtsu, & Kirino, 2005; Rinkel, Djibuti, Algra, & Van Gijn, 1998; So, Dowling, Mitchell, Laidlaw, & Yan, 2010). It has been concluded through extensive research (based on the hypothesis that the aneurysm size alone is the determinant) that for large aneurysms (>10mm), the risk of rupture is quite high and treatment is required, whereas for smaller aneurysms (<4mm) the lesions are safe and unlikely to rupture. As a matter of fact, this assumption is fallacious as some of these small lesions do rupture while larger aneurysms remain stable, which depicts that a new predictor

is needed. Little research has been made in the geometry of saccular aneurysms as the predictor for the rupture of a lesion with only the most basic parameters such as aspect ratio "head-to-neck ratio" (Parlea, Fahrig, Holdsworth, & Lownie, 1999). Since size is the easiest among all the properties of an aneurysm that can be measured, this is considered as the best indicator of likelihood of aneurysm rupture. The law of Laplace relates the in-plane Cauchy stress σ to the distension pressure P, aneurysm radius R, and aneurysmal wall thickness h for an inflated, thin-walled, spherical structure through a simple equation $\sigma = PR/2h$. For a given constant value of elastic modulus E, the expression for the critical radius of the aneurysm was used $as\ R_c = 2Eh/P$.

A gross mechanical failure of the arterial aneurysmal wall is responsible for the aneurysm rupture and occurs when the acting mechanical wall stress surpasses the potency of the tissue. In this study we predicted the aneurysm rupture in the light of the Laplace law, whereas the risk of ICA rupture was determined on the basis of the critical radii. The computed radii results obtained from computational model simulations were plotted against the theoretical results obtained from the Laplace law as shown in Figure 4-9. From this figure we believe that any arterial radii that fall above the presented Laplace curve are to be considered under risk of rupture and it is necessary to take medical action.

Chapter 5 CONCLUSIONS AND FUTURE WORK

5.1 Conclusions

What makes unique the approach to study ICAs formation and growth in this thesis is that it proposes to develop fluid-structure interactions through a 2-way coupling using a finite-element model based on the ALE algorithm. One of the striking factors of this study is that the finite-element method simulated fluid-structure interactions for blood flow through intracranial arteries. In previous studies (Niroomand Oscuii et al., 2007) it was indicated that the stress distribution and blood flow fields get affected from the elasticity of the arterial wall significantly as compared to a solid arterial wall.

The approach of computational fluid-structure interactions was applied to three idealized intracranial arteries with different curvatures, comprising of two different mechanical properties in one solid domain. It is for the first time that this model is developed in COMSOL Multiphysics in a 2-way coupling of fluid flow and solid structure finite-element solvers for a 3D geometry. The uniqueness of this model lies in the method in which a full coupling of the fluid domain and the solid domain compressed elasticity of different materials and simultaneously solved the fluid-solid domain equations using finite elements method. Basically, this method offers a vitally new perspective to study aneurysm's growth based on the response to controlled changes in the local mechanical properties of the arterial wall. This model approach may help to study the effects of local parameters on arterial remodelling outputs by independently controlling the parameters. Furthermore, this approach can also be utilized for solving patient-specific realistic geometries.

The need to develop a finite-element model was roused in order to solve the flow governing equations (Navier-Stokes equations) with the assumption of the Newtonian and incompressible steady flow and with the arterial wall assumed to be an elastic homogenous

hyperelastic neo-Hookean material. In this study, a fixed aneurysm wall thickness similar to the rest of the arterial wall was assumed, which we believe is an acceptable simplification for the intracranial arteries for the reason that intracranial arteries and their associated aneurysms possess very small wall thickness of $20\ to\ 200\ \mu m\ \ as$ compared to the normal extra cranial arteries (Kroon & Holzapfel, 2008). The possible location of aneurysm development on the arterial wall was predicted based on literature data (Kroon & Holzapfel, 2008)[Ref] that focused on the velocity fields and the streamlines of blood flow in the normal intracranial arterial segment models. Also, a selected part of the arterial wall was modified to detect the presence of an aneurysm in its initial stage of development.

In this study, a comprehensive analysis of fluid flow has been presented in three idealized intracranial models (straight and curved arteries, and arterial bifurcations) related to aneurysmal disease. The relationship between the hemodynamics of blood flow and aneurysm formation and growth has also been established. It was indicated through the analysis of our 3D CFD studies, which were altered with respect to local anatomical geometric parameters and by constituting a local hemodynamic environment, that the chances of the existence of an aneurysm growth on a high degree of arterial curvature is high if the inflow momentum is not impeded. However, it was observed that a large impact area on the aneurysm wall appears to be the most probable site for aneurysm initiation, growth or regrowth of a treated aneurysm. Our analysis has revealed that hemodynamic stresses are pressure-dependent and vary greatly over the pressure range values, as well as location-dependent, varying considerably all through the aneurysm. In addition, we have also provided evidence that the weakening of the arterial wall mechanical properties is significant for the commencement of the disease and for a sizeable aneurysm growth to occur.

This study contributes to the advancement of our knowledge towards aneurysm hemodynamic variable, such as blood velocity, pressure and shear stress. It aims to provide information for the healthy and diseased cardiovascular function and assists in predicting the risk of aneurysm rupture. It provides clinicians a modeling tool to gain a better understanding of the aneurysm hemodynamics and analyses to be used for optimal medical management.

5.2 Future Work

The results from this study suggest a wide range of future research projects with different set of assumptions. Among others, new models can be developed for non-Newtonian blood flow with other available hyperelastic material models and solid models such as Yeoh model or Mooney-Rivlin model (Lally, Dolan, & Prendergast, 2005). Below are a few suggestions for future works based on the current study:

- A new anisotropic model can be developed to compare with the current isotropic models in a finite element analysis of ICAs. Both the new model and current isotropic models can be added in simulations that integrate fluid-structure interactions between pulsatile blood flow and the ICA wall. The results from these studies can then be used to augment the effectiveness of current treatment decisions.
- Further computational results would be used to investigate the effects of a heterogeneous vessel wall with residual stress. Currently, all models of ICA tissue assumed a homogeneous wall with a fixed wall thickness, although the arterial wall is clearly known to have three heterogeneous layers (cf. Ch. 1).
- Additional computational work may also involve dividing the aneurysmal wall geometry into different regions and using a separate constitutive equations for each region. Such approach will be particularly useful in defining realistic geometries.
- New more elaborated patient-specific models could lead to a complete hemodynamic analysis that hopefully will incite new research that would result in enhanced treatment of multiple pathological conditions, such as ICAs.

References

A Huerta, M Casteleiro and H. Alder. (1993). Progress in arbitrary lagrangian-eulerian analysis of fluid and solid problems.B01/1

Agarwal, R., Katiyar, V. K., & Pradhan, P. (2008). A mathematical modeling of pulsatile flow in carotid artery bifurcation. International Journal of Engineering Science, 46(11), 1147-1156.

Alberto Figueroa, C., Baek, S., Taylor, C. A., & Humphrey, J. D. (2009). A computational framework for fluid-solid-growth modeling in cardiovascular simulations. Computer Methods in Applied Mechanics and Engineering, 198(45-46), 3583-3602.

Aubert, A., Costalat, R., Duffau, H., & Benali, H. (2002). Modeling of pathophysiological coupling between brain electrical activation, energy metabolism and hemodynamics: Insights for the interpretation of intracerebral tumor imaging. Acta Biotheoretica, 50(4), 281-295.

Austin, G. M., Fisher, S., Dickson, D., Anderson, D., & Richardson, S. (1993). The significance of the extracellular matrix in intracranial aneurysms. Annals of Clinical and Laboratory Science, 23(2), 97-105.

Bazilevs, Y., Gohean, J. R., Hughes, T. J. R., Moser, R. D., & Zhang, Y. (2009). Patient-specific isogeometric fluid-structure interaction analysis of thoracic aortic blood flow due to implantation of the jarvik 2000 left ventricular assist device. Computer Methods in Applied Mechanics and Engineering, 198(45-46), 3534-3550.

Bazilevs, Y., Hsu, M., Zhang, Y., Wang, W., Liang, X., Kvamsdal, T., Brekken, R., & Isaksen, J. G. (2010). A fully-coupled fluid-structure interaction simulation of cerebral aneurysms. Computational Mechanics, 46(1), 3-16.

Burton, A. C. (1954). Relation of structure to function of the tissues f the walls of blood vessels, Physiol. Rev. 34, 619-642.

Canham, P. B., & Ferguson, G. G. (1985). A mathematical model for the mechanics of saccular aneurysms. Neurosurgery, 17(2), 291-295.

Carew, T. E., Vaishnav, R. N., & Patel, D. J. (1968). Compressibility of the arterial wall. Circulation Research, 23(1), 61-68.

Castro, M. A., Putman, C. M., & Cebral, J. R. (2006). Computational fluid dynamics modeling of intracranial aneurysms: Effects of parent artery segmentation on intra-aneurysmal hemodynamics. American Journal of Neuroradiology, 27(8), 1703-1709.

Chen, H. Y. H., & Sheu, T. W. H. (2003). Finite-element simulation of incompressible fluid flow in an elastic vessel. International Journal for Numerical Methods in Fluids, 42(2), 131-146.

Christof Sohn, Hans-Joachim Voigt, Klaus Vetter. (c2004). Doppler ultrasound in gynecology and obstetrics, Stuttgart, New York, Thieme.

Chuong, C. J., & Fung, Y. C. (1984). Compressibility and constitutive equation of arterial wall in radial compression experiments. Journal of Biomechanics, 17(1), 35-40.

David H. Evans and W.N. McDicken. (c2000). Doppler ultrasound physics, instrumentation and signal processing, 2nd ed., Chichester, New York, Wiley.

De Hart, J., Peters, G. W. M., Schreurs, P. J. G., & Baaijens, F. P. T. (2003). A three-dimensional computational analysis of fluid-structure interaction in the aortic valve. Journal of Biomechanics, 36(1), 103-112.

Di Martino, E. S., Guadagni, G., Fumero, A., Ballerini, G., Spirito, R., Biglioli, P., & Redaelli, A. (2001). Fluid-structure interaction within realistic three-dimensional models

of the aneurysmatic aorta as a guidance to assess the risk of rupture of the aneurysm. Medical Engineering and Physics, 23(9), 647-655.

Duarte, F., Gormaz, R., & Natesan, S. (2004). Arbitrary lagrangian-eulerian method for navier-stokes equations with moving boundaries. Computer Methods in Applied Mechanics and Engineering, 193(45-47), 4819-4836.

Eriksson, T., Kroon, M., & Holzapfel, G. A. (2009). Influence of medial collagen organization and axial in situ stretch on saccular cerebral aneurysm growth. Journal of Biomechanical Engineering, 131(10), 101010.

Fish, P. (c1990). Physics and instrumentation of diagnostic medical ultrasound, Chichester, New York, Wiley.

Flori, F., Giudicelli, B., & Di Martino, B. (2009). A numerical method for a blood-artery interaction problem. Mathematical and Computer Modelling, 49(11-12), 2145-2151.

Fortin, A., & Fortin, M. (1990). A preconditioned generalized minimal residual algorithm for the numerical solution of viscoelastic fluid flows. Journal of Non-Newtonian Fluid Mechanics, 36(C), 277-288.

Foutrakis, G. N., Yonas, H., & Sclabassi, R. J. (1999). Saccular aneurysm formation in curved and bifurcating arteries. American Journal of Neuroradiology, 20(7), 1309-1317.

Francis A. Duck, Andrew C. Baker, Hazel C. Starritt. (c1998). Ultrasound in medicine, Bristol, Philadelphia, Pa., Institute of Physics Pub.

Fukuda, S., Hashimoto, N., Naritomi, H., Nagata, I., Nozaki, K., Kondo, S., Kurino, M., & Kikuchi, H. (2000). Prevention of rat cerebral aneurysm formation by inhibition of nitric oxide synthase. Circulation, 101(21), 2532-2538.

George J. Hademenos, Tarik F. Massoud. (c1998). The physics of cerebrovascular diseases, New York, Springer.

Gordon, J. E. (1975). Mechanical instabilities in biological membranes. Comparative Physiology, Functional Aspects of Structural Materials, , 49-57.

Griffith, T. M. (1994). Modulation of blood flow and tissue perfusion by endothelium-derived relaxing factor. Experimental Physiology, 79(6), 873-913.

Guivier-Curien, C., Deplano, V., & Bertrand, E. (2009). Validation of a numerical 3-D fluid-structure interaction model for a prosthetic valve based on experimental PIV measurements. Medical Engineering and Physics, 31(8), 986-993.

Guzman, R. J., Abe, K., & Zarins, C. K. (1997). Flow-induced arterial enlargement is inhibited by suppression of nitric oxide synthase activity in vivo. Surgery, 122(2), 273-280.

Hademenos, G. J., Massoud, T., Valentino, D. J., Duckwiler, G., & Vinuela, F. (1994a). A nonlinear mathematical model for the development and rupture of intracranial fusiform aneurysms. Neurological Research, 16(6), 433-438.

Hademenos, G. J., Massoud, T., Valentino, D. J., Duckwiler, G., & Vinuela, F. (1994b). A nonlinear mathematical model for the development and rupture of intracranial saccular aneurysms. Neurological Research, 16(5), 376-384.

Hashimoto, T., Meng, H., & Young, W. L. (2006). Intracranial aneurysms: Links among inflammation, hemodynamics and vascular remodeling. Neurological Research, 28(4), 372-380.

Hoi, Y., Meng, H., Woodward, S. H., Bendok, B. R., Hanel, R. A., Guterman, L. R., & Hopkins, L. N. (2004). Effects of arterial geometry on aneurysm growth: Three-

dimensional computational fluid dynamics study. Journal of Neurosurgery, 101(4), 676-681.

Humphrey, J. D., & Canham, P. B. (2000). Structure, mechanical properties, and mechanics of intracranial saccular aneurysms. Journal of Elasticity, 61(1-3), 49-81.

Humphrey, J. D., & Kyriacou, S. K. (1996). The use of laplace's equation in aneurysm mechanics. Neurological Research, 18(3), 204-208.

Huo, Y., Choy, J. S., Svendsen, M., Sinha, A. K., & Kassab, G. S. (2009). Effects of vessel compliance on flow pattern in porcine epicardial right coronary arterial tree. Journal of Biomechanics, 42(5), 594-602.

John Edward. (1946). Guyton and hall textbook of medical physiology, eBook link, http://www.eshare-org.co.cc/2010/02/textbook-of-medical-physiology-guyton.html

Jorgen Arendt Jensen. (1996). Estimation of blood velocities using ultrasound, Cambridge, New York, USA, Cambridge University Press.

Kinlay, S., Creager, M. A., Fukumoto, M., Hikita, H., Fang, J. C., Selwyn, A. P., & Ganz, P. (2001). Endothelium-derived nitric oxide regulates arterial elasticity in human arteries in vivo. Hypertension, 38(5), 1049-1053.

Koh, W., Kang, S., Cho, M., & Yoo, J. Y. (2009). Three-dimensional steady flow in non-linear elastic collapsible tubes. 2009 ASME Fluids Engineering Division Summer Conference, FEDSM2009, Vail, CO. , 1(PART C) 1785-1790.

Krex, D., Schackert, H. K., & Schackert, G. (2001). Genesis of cerebral aneurysms - an update. Acta Neurochirurgica, 143(5), 429-449.

Krittian, S., Janoske, U., Oertel, H., & Böhlke, T. (2010). Partitioned fluid-solid coupling for cardiovascular blood flow : LLLeft-ventricular fluid mechanics. Annals of Biomedical Engineering, 38(4), 1426-1441.

Kroon, M., & Holzapfel, G. A. (2008). Modeling of saccular aneurysm growth in a human middle cerebral artery. Journal of Biomechanical Engineering, 130(5).

Kyriacou, S. K., & Humphrey, J. D. (1996). Influence of size, shape and properties on the mechanics of axisymmetric saccular aneurysms. Journal of Biomechanics, 29(8), 1015-1022.

Lally, C., Dolan, F., & Prendergast, P. J. (2005). Cardiovascular stent design and vessel stresses: A finite element analysis. Journal of Biomechanics, 38(8), 1574-1581.

Lee waite. (c2006). Biofluid mechanics in cardiovascular system, New York, McGraw-Hill.

Lee, K. W., & Xu, X. Y. (2002). Modelling of flow and wall behaviour in a mildly stenosed tube. Medical Engineering and Physics, 24(9), 575-586.

Liepsch, D. W. (1986). Flow in tubes and arteries - A comparison. Biorheology, 23(4), 395-433.

Malek, A. M., Alper, S. L., & Izumo, S. (1999). Hemodynamic shear stress and its role in atherosclerosis. Journal of the American Medical Association, 282(21), 2035-2042.

Milne-Thomson, L. M. (1958). Theoretical aerodynamics, London, Macmillan, c1966 .

Moosavi, M., Fatouraee, N., & Katoozian, H. (2009). Finite element analysis of blood flow characteristics in a ventricular assist device (VAD). Simulation Modelling Practice and Theory, 17(4), 654-663.

Morita, A., Fujiwara, S., Hashi, K., Ohtsu, H., & Kirino, T. (2005). Risk of rupture associated with intact cerebral aneurysms in the japanese population: A systematic review of the literature from japan. Journal of Neurosurgery, 102(4), 601-606.

Mosora, F., Harmant, A., Bernard, C., Fossion, A., Pochet, T., Juchmes, J., & Cescotto, S. (1993). Modelling the arterial wall by finite elements. Archives Internationales De Physiologie, De Biochimie Et De Biophysique, 101(3), 185-191.

Nichols, D. A., Meyer, F. B., Piepgras, D. G., & Smith, P. L. (1994). Endovascular treatment of intracranial aneurysms. Mayo Clinic Proceedings, 69(3), 272-285.

Nikolov, S., Stoytchev, S., Torres, A., & Nieto, J. J. (2003). Biomathematical modeling and analysis of blood flow in an intracranial aneurysm. Neurological Research, 25(5), 497-504.

Niroomand Oscuii, H., Tafazzoli Shadpour, M., & Ghalichi, F. (2007). Flow characteristics in elastic arteries using a fluid-structure interaction model. American Journal of Applied Sciences, 4(8), 516-524.

Oshima, M., Torii, R., Kobayashi, T., Taniguchi, N., & Takagi, K. (2001). Finite element simulation of blood flow in the cerebral artery. Computer Methods in Applied Mechanics and Engineering, 191(6-7), 661-671.

P. J. Camarata, R. E. Latchaw. (1993). State of the art in medicine: Intracranial aneurysms.28(4)

P. Niyogi, S.K. Chakrabartty, M.K. Laha. (2005). Introduction to computational fluid dynamics, Cambridge, New York, Cambridge University Press.

Parlea, L., Fahrig, R., Holdsworth, D. W., & Lownie, S. P. (1999). An analysis of the geometry of saccular intracranial aneurysms. American Journal of Neuroradiology, 20(6), 1079-1089.

Peattie, R. A., Riehle, T. J., & Bluth, E. I. (2004). Pulsatile flow in fusiform models of abdominal aortic aneurysms: Flow fields, velocity patterns and flow-induced wall stresses. Journal of Biomechanical Engineering, 126(4), 438-446.

Pericevic, I., Lally, C., Toner, D., & Kelly, D. J. (2009). The influence of plaque composition on underlying arterial wall stress during stent expansion: The case for lesion-specific stents. Medical Engineering and Physics, 31(4), 428-433.

Peter W. Callen. (c2000). Ultrasonography in obstetrics and gynecology, 5th ed., Philadelphia, Saunders Elsevier.

Resnick, N., Yahav, H., Shay-Salit, A., Shushy, M., Schubert, S., Zilberman, L. C. M., & Wofovitz, E. (2003). Fluid shear stress and the vascular endothelium: For better and for worse. Progress in Biophysics and Molecular Biology, 81(3), 177-199.

Rinkel, G. J. E., Djibuti, M., Algra, A., & Van Gijn, J. (1998). Prevalence and risk of rupture of intracranial aneurysms: A systematic review. Stroke, 29(1), 251-256.

Robert Shadwick. (1999). Mechanical design in arteries, New York, Informa Healthcare.

S. Satomura. (1957). Ultrasonic doppler method for the inspection of cardiac functions.29, 1181-1185.

Schmid-Schönbein, H., Wells, R., & Goldstone, J. (1969). Influence of deformability of human red cells upon blood viscosity. Circulation Research, 25(2), 131-143.

Scott, S., Ferguson, G. G., & Roach, M. R. (1972). Comparison of the elastic properties of human intracranial arteries and aneurysms. Canadian Journal of Physiology and Pharmacology, 50(4), 328-332.

Sekhar, L. N., & Heros, R. C. (1981). Origin, growth, and rupture of saccular aneurysms: A review. Neurosurgery, 8(2), 248-260.

So, T. Y., Dowling, R., Mitchell, P. J., Laidlaw, J., & Yan, B. (2010). Risk of growth in unruptured intracranial aneurysms: A retrospective analysis. Journal of Clinical Neuroscience, 17(1), 29-33.

Steiger, H. J. (1990). Pathophysiology of development and rupture of cerebral aneurysms. Acta Neurochirurgica, Supplement, 48, 1-57.

Structural Mechanics Model: User's Guide. (2008). COMSOL multiphysiscs V.3.5a.

Takizawa, K., Christopher, J., Tezduyar, T. E., & Sathe, S. (2010). Space-time finite element computation of arterial fluid-structure interactions with patient-specific data. International Journal for Numerical Methods in Biomedical Engineering, 26(1), 101-116.

Taylor, C. A., Hughes, T. J. R., & Zarins, C. K. (1998). Finite element modeling of blood flow in arteries. Computer Methods in Applied Mechanics and Engineering, 158(1-2), 155-196.

Torii, R., Oshima, M., Kobayashi, T., Takagi, K., & Tezduyar, T. E. (2006). Fluid-structure interaction modeling of aneurysmal conditions with high and normal blood pressures. Computational Mechanics, 38(4-5), 482-490.

Torii, R., Oshima, M., Kobayashi, T., Takagi, K., & Tezduyar, T. E. (2007a). Influence of wall elasticity in patient-specific hemodynamic simulations. Computers and Fluids, 36(1), 160-168.

Torii, R., Oshima, M., Kobayashi, T., Takagi, K., & Tezduyar, T. E. (2007b). Numerical investigation of the effect of hypertensive blood pressure on cerebral aneurysm - dependence of the effect on the aneurysm shape. International Journal for Numerical Methods in Fluids, 54(6-8), 995-1009.

Torii, R., Oshima, M., Kobayashi, T., Takagi, K., & Tezduyar, T. E. (2009). Fluid-structure interaction modeling of blood flow and cerebral aneurysm: Significance of artery and

aneurysm shapes. Computer Methods in Applied Mechanics and Engineering, 198(45-46), 3613-3621.

Torii, R., Oshima, M., Kobayashi, T., Takagi, K., & Tezduyar, T. E. (2010). Influence of wall thickness on fluid-structure interaction computations of cerebral aneurysms. International Journal for Numerical Methods in Biomedical Engineering, 26(3-4), 336-347.

Valentín, A., & Humphrey, J. D. (2009). Evaluation of fundamental hypotheses underlying constrained mixture models of arterial growth and remodelling. Philosophical Transactions of the Royal Society A: Mathematical, Physical and Engineering Sciences, 367(1902), 3585-3606.

Vatov, L., Kizner, Z., Ruppin, E., Meilin, S., Manor, T., & Mayevsky, A. (2006). Modeling brain energy metabolism and function: A multiparametric monitoring approach. Bulletin of Mathematical Biology, 68(2), 275-291.

Wang, Q., Wang, W., Fei, Z., Liu, Y., & Cao, Z. (2009). Simulation of blood flow in intracranial ICA-PComA aneurysm via computational fluid dymamics modeling. Journal of Hydrodynamics, 21(5), 583-590.

Wang, Y., Zhao, N., Mao, J., & Wang, D. (2007). Arbitrary lagrangian-eulerian method with adaptive moving mesh. Jisuan Wuli/Chinese Journal of Computational Physics, 24(3), 261-267.

Watanabe, H., Hisada, T., Sugiura, S., Okada, J., & Fukunari, H. (2002). Computer simulation of blood flow, left ventricular wall motion and their interrelationship by fluid-structure interaction finite element method. JSME International Journal, Series C: Mechanical Systems, Machine Elements and Manufacturing, 45(4), 1003-1012.

Wilmer W. Nichols and Michael F. O'Rourke. (1990). Mc donald's blood flow in arteries, 3rd ed., Philadelphia : Lea & Febiger.

Wilmer W. Nichols and Michael F. O'Rourke. (1997,1990,1998). Mc donald's blood flow in arteries, 4th ed., London : Arnold ; New York : Oxford University Press.

Y.C. Fung. (1990). Biomechanics/ motion, flow, stress and growth, New York , Springer.

Y.C. Fung. (1993). Biomechanics / mechanical properties of living tissues, Second Edition, , New York , Springer.

Yeh, C., Ferrara, K. W., & Kruse, D. E. (2004). High-resolution functional vascular assessment with ultrasound. IEEE Transactions on Medical Imaging, 23(10), 1263-1275.